Copyright

by

Alexandra Yakovlevna Woldman

2017

The Dissertation Committee for Alexandra Yakovlevna Woldman Certifies that this is the approved version of the following dissertation:

Phase-field modeling of the thermo-electro-mechanically coupled behavior of ferroelectric materials

Committee:

Chad M. Landis, Supervisor

Mark E. Mear

Rui Huang

Krishnaswa Ravi-Chandar

John Timothy Foster

Phase-field modeling of the thermo-electro-mechanically coupled behavior of ferroelectric materials

by

Alexandra Yakovlevna Woldman

Dissertation

Presented to the Faculty of the Graduate School of

The University of Texas at Austin

in Partial Fulfillment

of the Requirements

for the Degree of

Doctor of Philosophy

The University of Texas at Austin

December 2017

Acknowledgements

I would not have been able to complete this work without the contribution of many people in my life. They say it takes a village to raise a child, but it also takes a village to complete a PhD program.

First and foremost, I would like to thank my advisor, Dr. Chad M. Landis for his advice and mentorship over the past years. Throughout our difficulties with projects, highs and lows, Dr. Landis was always supportive and helpful in our work. I appreciate his logical and clearheaded advice and I have learned a lot from him. I would also like to thank the members of my Graduate Committee: Dr. Rui Huang, Dr. Mark Mear, Dr. K. Ravi-Chandar and Dr. John Foster for their time, guidance and intellectual curiosity. It is truly appreciated. To the many other professors of the Engineering Mechanics Department who have taught me over the years, thank you. I would also like to acknowledge the department staff, who have helped and supported me over the years. I must also thank my current and past friends and colleagues of the ASEM Department: thank you for always being there for me, both academically and socially, as we toiled through the years to get our degrees.

Over my years at UT Austin, I have had many sources of funding. Some of the work was funded through ARO grant number W911NF-13-1-0220 and NSF grant CMMI-1068024. I would specifically like to acknowledge the National Science Foundation Graduate Research Fellowship, which helped me tremendously, both

financially and academically, by allowing me the freedom to make my academic choices without the constraints of funding. I would also like to acknowledge the UT Diversity Recruitment Fellowship and the UT Thrust Fellowship that helped fund me during parts of my time at UT Austin.

Finally, I would like to thank my family, who have shaped me into the person that I am today. To my parents, Mila and Yakov, thank you so much for supporting me in my education and in every other part of my life. To my sister Tatiana, thank you for being there for me all these years. The family dinners, the time with the kids and just being in the same city with you for years has been a true pleasure. And to my husband Will, I cannot thank you enough for your support and kindness you have shown me in this process. We have gone through this phase of our lives together, and I could not have asked for a better partner. I cannot wait to continue my adventure with you.

Phase-field modeling of the thermo-electro-mechanically coupled behavior of ferroelectric materials

Alexandra Yakovlevna Woldman, PhD

The University of Texas at Austin, 2017

Supervisor: Chad M. Landis

Ferroelectric materials are widely used in engineering and science applications due to their large nonlinear thermo-electro-mechanical coupling. Of interest recently, has been the study of the giant electrocaloric effect, a large adiabatic temperature change with the application of an electric field, due to its possible application for solid-state cooling. The electrocaloric effect is maximized near phase transitions, where entropy jumps contribute to a large nonlinear effect. This dissertation develops a continuum phase-field model for the thermo-electro-mechanically coupled behavior for ferroelectric materials. The model is derived from thermodynamic considerations and based on a phenomenological free energy function. The finite element method is applied to solve the governing equations for a selected set of boundary value problems. Mechanical displacement, electric potential, polarization and temperature are used as degrees of freedom in the formulation of the finite element implementation of the model.

The a geometry for an isothermal stable two-dimensional ferroelectric to paraelectric phase boundary is developed, along with appropriate boundary conditions, and simulated using the nonlinear finite element method for a variety of ferroelectric domain widths. The dependence of the phase coexistence temperature,

boundary energy, entropy jump across the boundary and closure domain shape on the ferroelectric laminate domain width is quantified. A simulation of the motion of the phase boundary through the material under entropy/heat input control is demonstrated.

Next, a realistic electrocaloric cooling device based on a multilayer ferroelectric capacitor is simulated through a full thermodynamic refrigeration cycle. The model geometry and boundary conditions are chosen to match realistic device configurations. The device is driven through a cycle with two adiabatic and two constant electric field legs, and compared with the analytically computed ideal plane strain electrocaloric cooling cycle. Several inefficiencies arise in the device, including incomplete transformation, entropy loss due to phase boundary motion, and high energy zones with large stresses and closure domains at the electrode tip.

Lastly, motivated by potential uses as actuators, the domain structure in three-dimensional ferroelectric nanodots is modeled by cooling from a paraelectric phase. The expected vortex domain structure forms in sufficiently small dots, but distorts upon further cooling to room temperature. The room temperature transfer of dots to a rigid substrate and actuation via an out-of-plane electric field leads to incomplete domain switching, thereby reducing actuator displacements.

Table of contents

List of figures

Chapter 1: Introduction

Ferroelectricity is a material property wherein a material has an intrinsic spontaneous polarization that can be reversed with the application of an electric field. Ferroelectric materials display a range of novel field-coupled behaviors like pyroelectricity, piezoelectricity, and electrocaloric behavior that make them useful in a wide range of engineering applications. Ferroelectricity was originally discovered in 1920, but only came to be widely studied in science and engineering upon the discovery of the robust ceramic, barium titanate, in the 1940s. Bulk ceramic barium titanate came into wide usage in device applications like actuators and transducers. The field expanded dramatically upon the development of thin film ferroelectric materials that could be integrated into semiconductor chips. Modern electronics use thin film ferroelectric materials for a wide array of applications, including sensors, ferroelectric random access memory and fuel injectors [1]. Of particular interest to this work, ferroelectric materials exhibit the electrocaloric effect (ECE): an adiabatic temperature change upon the application of an electric field. This electric field driven temperature change could potentially be harnessed for solid-state cooling or for energy harvesting.

A wide variety of techniques have been used to model ferroelectric behavior in materials. Good overviews of the techniques can be found in Duan and Liu [2] and Potnis *et al.* [3] and are briefly reviewed here. Generally, ferroelectric

microstructure can be studied by applying either a first principles approach or with the use of a phenomenological model. The first principle calculations compute the material properties and behavior directly from quantum mechanics, without the use of any input parameters from experiments [2]. Phenomenological models for ferroelectric materials, on the other hand, assume that the free energy is a function of the polarization and strain and can be written as a power series. Phenomenological models aim to accurately capture the behavior of a material under a given set of conditions, but are not directly derived from fundamental principles. In phenomenological models for ferroelectric materials, the elastic, piezoelectric and electrostrictive coefficients are chosen to match the known material response. There is computational trade-off between accuracy and speed of the two general methods [3]. While first principle calculations tend to be highly accurate and better motivated by fundamental physics, they cannot model large regions due to the tremendous computational costs of such computations. Phenomenological model are computationally faster and can therefore model larger regions with more microstructural complexity, but do not capture the exact physics of the material.

Ferroelectric materials form domain structures which influence the bulk material response, making the study of domain evolution critical to understanding ferroelectrics. Domain evolution models for ferroelectric materials can also be classified, broadly, into two types: sharp interface models and diffuse interface

models [3]. Sharp interface models treat domain walls in ferroelectric materials as defect and find driving forces for the motion of the defect. Diffuse interface models treat domain walls as part of a continuum. This dissertation relies on the use of a phenomenological model and diffuse interfaces based on phase-field modeling. Phase-field modeling is a powerful tool for modeling microstructure evolution in materials by using order parameters that take on distinct values in each phase and/or domain [4]. Background information on ferroelectric materials, the electrocaloric effect and phase-field modeling are presented in the remainder of this chapter.

1.1 FERROELECTRIC AND PARAELECTRIC BEHAVIOR IN BARIUM TITANATE

Ferroelectricity was first discovered by Valasek in 1921 while he was performing experiments on Rochelle salt, a material that was already known to have strong piezoelectric and pyroelectric properties [5]. Valasek's work includes the first publication of the now well-known polarization-electric field hysteresis curve that is indicative of ferroelectricity. Ferroelectric materials are characterized by a spontaneous polarization at zero electric field. The spontaneous polarization can then be switched by the application of a sufficiently large electric field, E_0. An illustration of the classic ferroelectric hysteresis curve is shown in Figure 1.1(a). The dashed line indicates that an inhomogeneous ferroelectric material that begins at a neutral average polarization and zero electric field can be poled with the application of a biasing electric field. When the electric field is returned to zero, the polarization

does not return to zero. The material polarization can then be switched to the opposite polarization direction with the application of an electric field of magnitude E_0 or greater in the direction opposite to the original polarization vector.

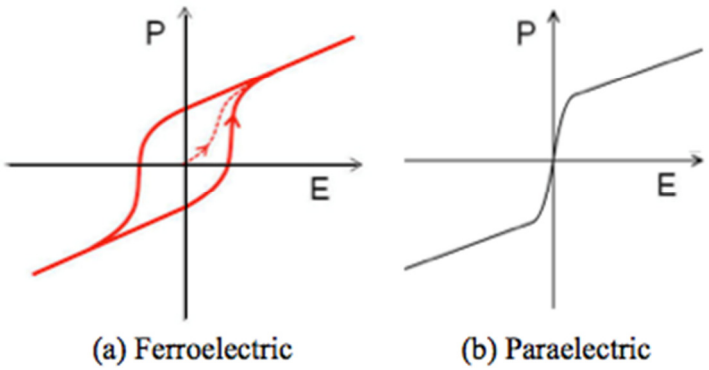

Figure 1.1: (a) Ferroelectric and (b) paraelectric behavior in materials. Ferroelectric materials exhibit a nonzero spontaneous polarization (P) at zero electric field (E), which can be switched by the application of an opposing electric field. Paraelectric materials do not have a spontaneous polarization and do not exhibit hysteresis.

Ferroelectricity is generally a temperature-dependent phenomenon. Ferroelectric behavior is exhibited at temperatures below a critical phase transition temperature, known as the Curie temperature and indicated throughout this dissertation as θ_C. At temperatures sufficiently above the Curie temperature, the spontaneous polarization ceases to exist and the polarization at zero electric field is zero. Paraelectric material behavior is still nonlinear, but no longer hysteretic, as shown in Fig. 1.1(b). While these are two distinct material responses, it should be noted that for certain materials, the behavior at the Curie temperature is a combination of the ferroelectric and paraelectric curves.

All of the simulations and calculations in this work are done with material properties and characteristics of the ferroelectric perovskite barium titanate ($BaTiO_3$). $BaTiO_3$ has been studied extensively and its material properties are well-characterized in the literature. $BaTiO_3$ exhibits a first-order phase transition at its Curie temperature of 125°C. First-order phase transitions are characterized by a latent heat associated with the phase transition, and allow for the coexistence of the phases at a temperature of exactly θ_C (for the ideal single crystal case). A simple example of this is the melting of ice. At 0°C, ice will transition to water with the addition of latent heat. The additional heat does not change the temperature of the ice/water mixture until all the ice has melted into water. Therefore, at the transition temperature, the two phases can coexist under heat/entropy control. Second-order phase transitions do not allow for phase coexistence under isothermal conditions and will not be discussed further in this work.

Solid state phase transitions are often associated with a change in symmetry of the crystal structure. Above the Curie temperature, $BaTiO_3$ has a cubic structure. The centrosymmetric crystal structure, shown in Fig. 1.2(a), exhibits paraelectric behavior. Below the Curie temperature, the titanium (Ti) atom is no longer thermodynamically stable in the center of the cubic structure, and moves in one of six equally likely tetragonal directions (a loss of the cubic symmetry). A representative tetragonal crystal structure is shown in Fig. 1.2(b). The unit cell elongates in the tetragonal direction and shortens in the two perpendicular

directions, leading to a spontaneous strain (relative to the cubic structure). The off-center location of the titanium atom causes a spatial imbalance in the charges, which generates a spontaneous polarization P_0 along the tetragonal axis in the crystal. Figure 1.2(c) shows all six possible spontaneous polarization directions that are stable below the Curie temperature.

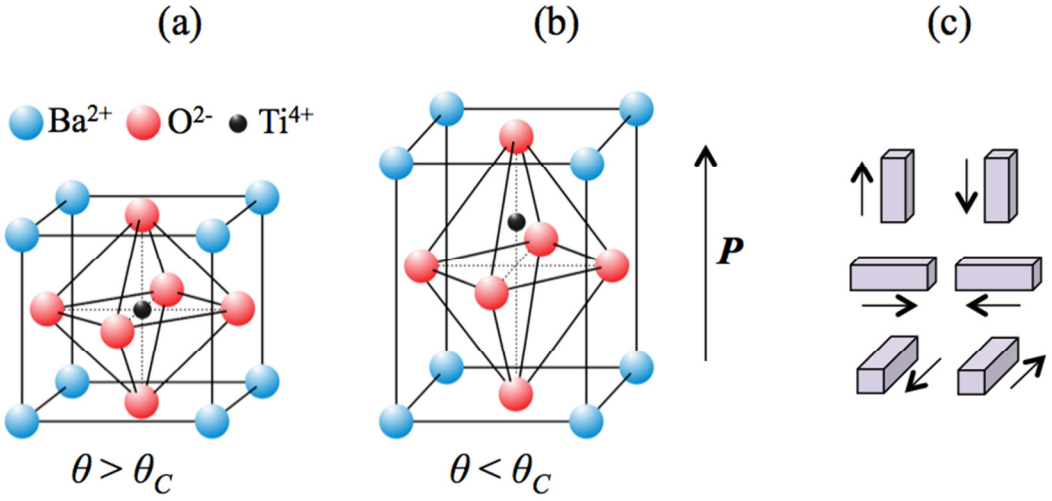

Figure 1.2: The crystal structure of barium titanate above and below the Curie temperature (θ_C). (a) Above θ_C, the crystal structure is cubic and the charges are balanced due to the centrosymmetry of the crystal structure. (b) Below θ_C, the crystal structure is tetragonal, with a spontaneous polarization in one of six tetragonal directions, which are illustrated in (c).

Due to its lack of centrosymmetry and intrinsic dipole moment, tetragonal $BaTiO_3$ exhibits two common coupled material behaviors: piezoelectricity and pyroelectricity. The piezoelectric effect is when an applied electric field leads to a strain in the material, or inversely, an applied stress causes a change in electric displacement/polarization. In $BaTiO_3$, linear piezoelectric behavior occurs at stresses and electric fields that are below the magnitudes necessary to induce

domain switching. The pyroelectric effect is a change in electric displacement/polarization caused by an increase or decrease in temperature. All pyroelectric crystal structures are also piezoelectric. In $BaTiO_3$, linear pyroelectric behavior occurs at temperatures well below the Curie temperature (around the Curie temperature, the behavior is highly nonlinear). The inverse of the pyroelectric effect, the electrocaloric effect, is discussed in greater detail in Section 1.2.

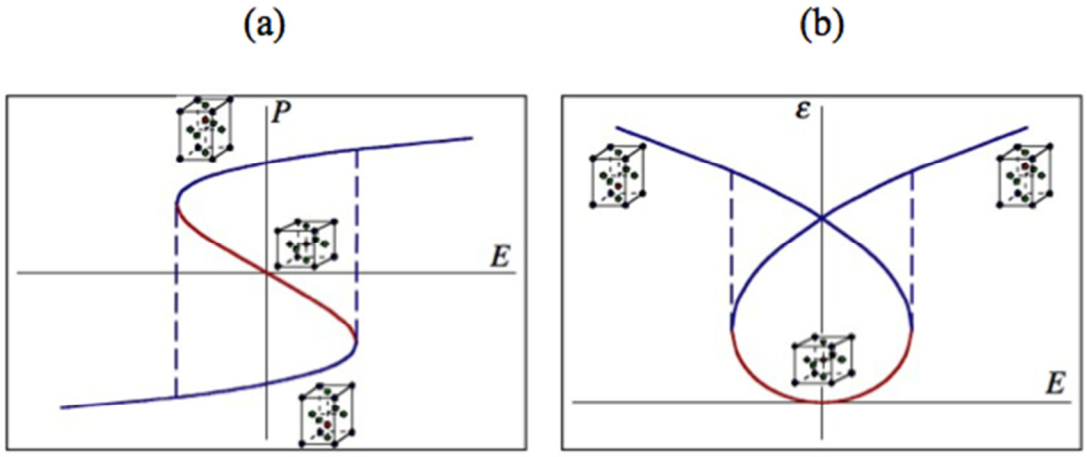

Figure 1.3: The nonlinear ferroelectric behavior of single crystal $BaTiO_3$ under an electric field applied along the tetragonal axis at temperatures below θ_C. (a) The polarization will switch by 180° when a sufficiently large electric field is applied, as indicated by the dotted line. The red sections are unstable portions of the curve. (b) The strain will spontaneously jump (along the dotted lines) when a large electric field switches the polarization.

Nonlinear coupled behavior in ferroelectric crystals is directly related to the crystal structure. When a sufficiently large antiparallel electric field is applied to the tetragonal $BaTiO_3$ crystal, the titanium atom, no longer stable, moves to align with the electric field, switching the polarization direction by 180°. This switching regime gives rise to the ferroelectric behavior of $BaTiO_3$ and the polarization-electric field

relationship is shown in Fig 1.3(a). The red section of the plot indicates unstable material behavior and the material exhibits spontaneous polarization switching as indicated by the dashed lines. The strain behavior for the same condition is shown in Fig. 1.3(b): a small electric field in the opposite direction of the polarization will cause the crystal to shrink along the tetragonal direction, but once the field is sufficiently large, polarization switching causes the strain to increases spontaneously, as indicated by the dashed lines. An electric field perpendicular to the polarization direction will lead to 90° switching in the polarization direction, with the titanium atom aligning with the electric field direction. Because of the spontaneous strains that exist in ferroelectric $BaTiO_3$, mechanical loading can also be used to induce switching in the polarization. For instance, a large compressive force in the direction parallel to the tetragonal axis will lead to 90° switching in the polarization direction, a property referred to as ferroelesticity. Thus, the shape and polarization of the material can be altered by changing the temperature, applying an electric field or applying stress, leading to the recognition that $BaTiO_3$ is a fully thermo-electro-mechanically coupled nonlinear material. A summary of the linear and nonlinear material responses discussed here are shown in Fig. 1.4.

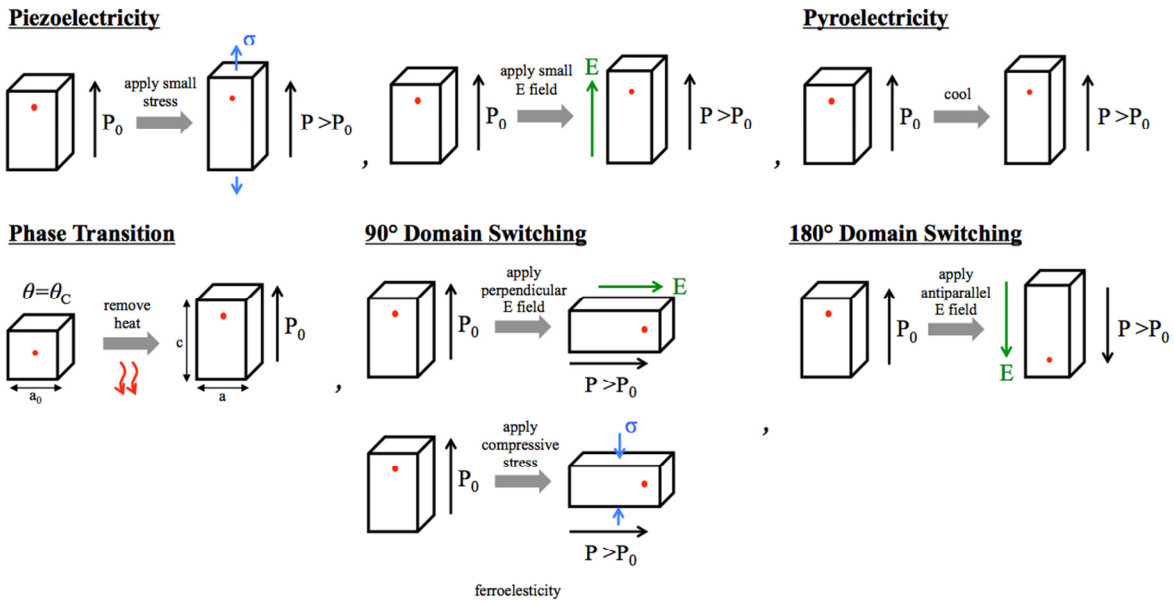

Figure 1.4: The coupled field behavior in $BaTiO_3$ single crystal. The red dot represents the location of the titanium atom in the crystal structure. Linear piezoelectric and pyroelectric effects occur at small loads and at temperatures far below θ_C, respectively. Phase transitions and domain switching are highly nonlinear coupled behaviors in $BaTiO_3$. The cubic to tetragonal phase transition occurs at θ_C with the removal/addition of latent heat. Sufficiently large electric fields and stresses can cause domain switching in the crystal.

1.1.1 Domain walls in tetragonal ferroelectric materials

The crystal structure of ferroelectric materials allows us to understand the fundamental behaviors of the material under thermal and elecromechanical loading. However, ferroelectric materials rarely exist in a pure single crystal with a single polarization direction. For tetragonal $BaTiO_3$, there are six energetically equivalent variants, and twinning between these variants is instrumental in forming charge-neutral crystals. Upon cooling below the Curie temperature, polycrystalline

ferroelectric materials form complex domain structures that minimize the energy within the constraints of the surface conditions and loading, often forming irregular geometric structures.

There are two low energy domain structures for tetragonal ferroelectric materials: 180° domain walls and 90° domain walls with a head-to-tail domain configuration [6]. The two structures are illustrated in Fig. 1.5, showing a schematic of ideal crystal boundary, the deformed shape of the one-dimensional stress-free boundary for a diffuse domain wall model, and a plot of the polarization in the crystal as a function of distance for a diffuse domain wall model. A third type of domain wall, a 90° head-to-head or tail-to-tail orientation with a charged boundary was shown to be unstable in experiments. In order to reduce the electrostatic energy in such a boundary, it naturally evolves from a straight planar boundary into a fine zigzag pattern [7]. The two low energy domain wall structures are electrically and mechanically compatible, and have been observed through microscopy imagining. In 180° domains, the polarization of the two variants have equal magnitude but opposite direction. The domain wall, which is the boundary that forms between the two variants (or domains), is parallel to both polarization vectors. For a diffuse boundary model, the average magnitude of the polarization in the domain wall is zero (see Fig. 1.5(a)), meaning the structure of the material in the domain wall is, ideally, cubic/paraelectric. However, for a mechanically free bidomain, the domain wall is in tension due to its confinement between the two

tetragonal domains. The domain wall is therefore at a high energy as compared to the interior of the domains. For the 90° domains, the polarizations in the two domains are of equal magnitude, perpendicular to one another and arranged in a head-to-tail configuration. The domain wall makes a 45° angle with each of the polarization vectors. This creates a charge neutral boundary because the component of the polarization perpendicular to the boundary does not change across the domain wall. For a diffuse boundary model, the polarization in the domain wall is nonzero and is (on average) perpendicular to the domain wall, but its magnitude is smaller than in the domains. In a free bidomain, the 90° domains distorts, shearing at the domain wall (see Fig. 1.5(b)), to become lower symmetry [6]. The domain wall is once again stressed in this configuration, but the stresses are smaller than in the 180° wall. Given the assumption that the domain walls have finite width, the width of the 180° domain wall is about 2/3 the width of the 90° domain wall at room temperature [8].

Both domain wall structures can be moved with the application of an electric field parallel to the wall. The green arrows in Fig. 1.5 indicate the direction of wall motion with the application of a positive *y*-direction electric field. Any nonzero electric field applied to either domain wall structure will annihilate the unfavorable domain in an ideal crystal (no hysteresis due to lattice friction or pinning), creating a monodomain. However, the domain walls are stable under charge control with the appropriate boundary conditions. Equal fractions of each domain exist under charge

neutral conditions, but any nonzero charge condition will result in a readjustment of the volume fraction of each domain. The two low-energy domain structures can be repeated to form rank-1 laminates. The laminates can also be combined and repeated to form more diverse and complex microstructures. For in-depth discussion of higher rank laminate structures, see Tsou and Huber [9].

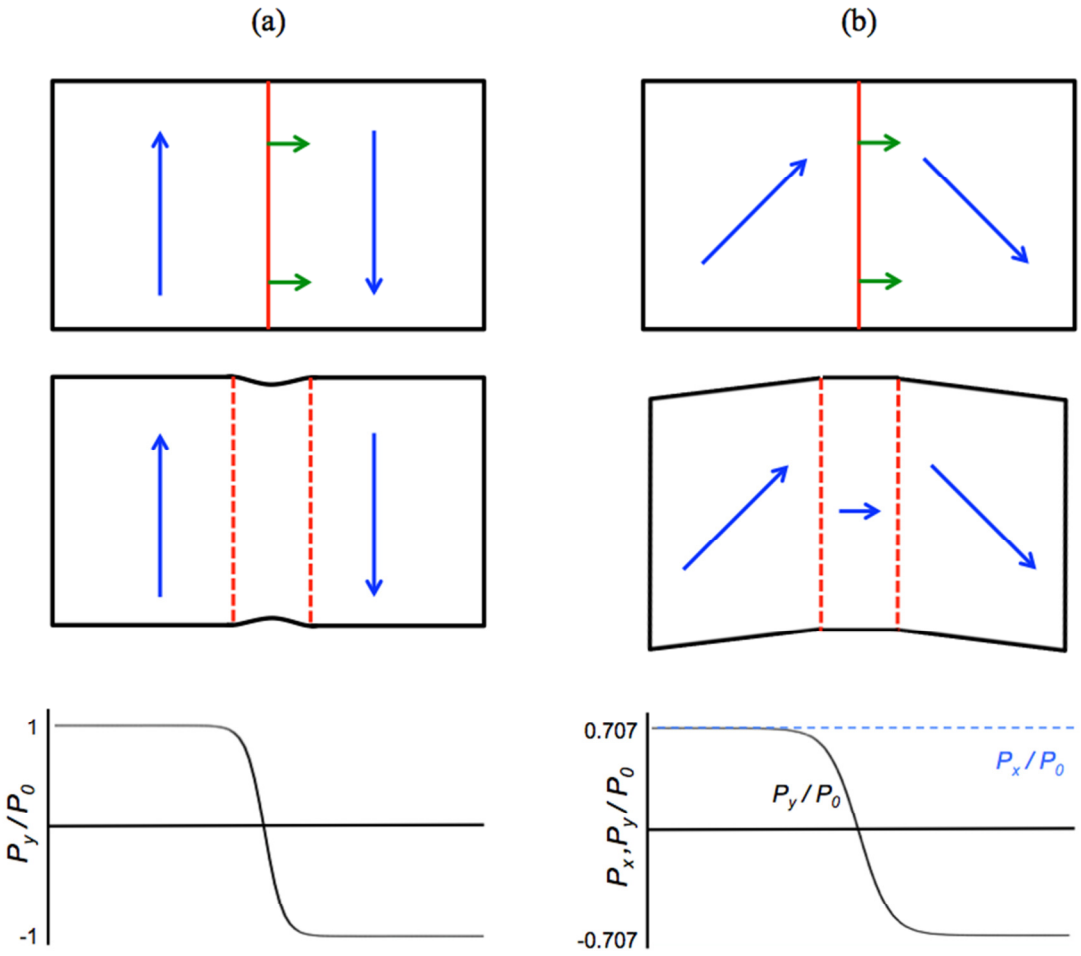

Figure 1.5: Schematic of tetragonal ferroelectric domain structures (domain walls indicted in red and polarization indicated in blue) for (a) a 180° domain and (b) a 90°domain wall with head-to-tail configuration. The green arrows show the direction of motion of the domain wall with the application of a positive electric field parallel to the domain wall. The second image for each domain indicates the deformed shape for a diffuse boundary model with no stress. The third image gives a plot of the polarization components as a function of location for the two domains.

1.2 ELECTROCALORIC EFFECT AND COOLING CYCLES

The electrocaloric effect (ECE) is the adiabatic temperature change from the application of an electric field. It is the inverse of the pyroelectric effect. While the

ECE was known and quantified decades ago for materials like Rochelle salts and potassium dihydrogen phosphate [10], [11], the temperature change produced was small and the voltage requirements too large for commercial applications. In 2006, a seminal paper by Mischenko *et al.* [12] demonstrated the giant ECE in thin film $PbZr_{0.95}Ti_{0.05}O_3$ (PZT), with a maximum 12K temperature change at an applied voltage of 25 V. The use of thin films allows small voltages to generate large electric field without the threat of electrical breakdown/arcing in the surroundings. The giant ECE is maximized near the Curie temperature of a material, where phase transitions occur [13], [14], especially in transitions with large entropy changes. Since Mischenko's discovery, there have been numerous studies investigating the electrocaloric effect in ferroelectric materials [14]. Akcay *et al.* applied Landau-Devonshire theory to study the effect of electric field [13] and strain [15] on the electrocaloric effect in single domain materials, and Li *et al.* [16] used Landau-Ginzburg-Devonshire (LGD) theory to study the effects of electric field and strain on the electrocaloric effect in multi-domain thin films. Ferroelectric nanostructures are also of considerable interest [17], and Liu and Wang [18] have recently investigated the room temperature electrocaloric effect in ferroelectric nanotubes using LGD theory. For a thorough review of the literature on electrocaloric materials, see Scott [14] .

The application of the ECE to engineering applications mainly focuses on the use of thermodynamic cooling cycles for efficient solid-state refrigeration, or the

reverse cycle for energy generation. Conventional refrigeration techniques use the vapor compression cycle and are bulky, poorly scalable and offer only moderate efficiency (40-50%). Electrocaloric coolers, in contrast, are high efficiency (60-70%), lighter, scalable, and offer possibilities for device integration, including for microelectronics [19].

A thermodynamic cycle for electrocaloric cooling is built by combining adiabatic (and ideally isentropic) steps with isothermal or constant electric field steps. Many other cycles are also possible, but will not be discussed in details here. The schematic for a possible electrocaloric cooling cycle is shown in Fig. 1.6. Starting at the top left corner of the cycle, the material begins in a high entropy and low temperature state. For operating temperatures at or above the Curie temperature, this would be a paraelectric state. The material is then adiabatically heated by applying an electric field. The field will then induce a phase transition from paraelectric to ferroelectric, and therefore a polarization is induced, in the material. On the second leg, the material ejects heat to a heat sink, reducing the entropy. This can be done either isothermally or at a constant electric field. These two cases are shown with the solid line and dashed grey lines in Fig. 1.5, respectively. The isothermal cycle is referred to in the literature as a Carnot-like electrocaloric cycle [14], [20], [21], and allows for the largest temperature changes with minimal work input. To maintain the isothermal conditions while ejecting or absorbing heat, the Carnot-like cycle requires adjusting the electric field to keep the material at a

constant temperature. Note that isothermal processes are notoriously slow [17]. The constant electric field cycle has constant boundary conditions for the second and fourth legs of the cycle, and is therefore much more straightforward to implement in both simulations and practice [21]. On the third step of the cycle, the material is adiabatically cooled by the removal of the applied electric field. For operating temperatures at or above the Curie temperature, the removal of the field will make the material, in the ideal case, paraelectric. Finally, the material absorbs heat from a source (thereby cooling the source) to return to its original entropy and temperature. As the cycle repeats, the continuous removal of heat cools the source. The operating temperature of the source dictates the starting temperature of the electrocaloric cooling cycle. It is useful to note here that while the present work is done with $BaTiO_3$ and the specific Curie temperature of 125°C, ferroelectric ceramic Curie temperatures can be tuned by chemical substitution or prestrain [22]. Thus, it is conceivable that a material's properties can be tuned such that its Curie temperature is near the operating temperature of a device, maximizing the device efficiency.

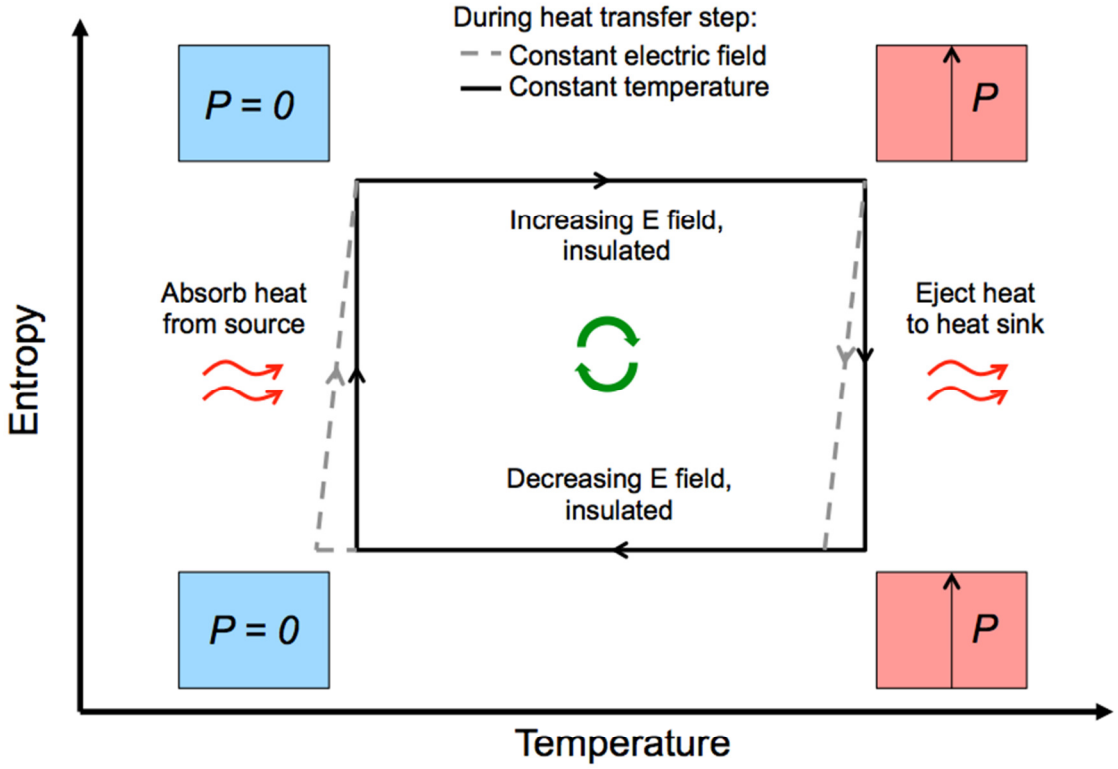

Figure 1.6: A schematic of the electrocaloric cooling cycle, operating at or above the Curie temperature of a ferroelectric material. The cycle has two adiabatic legs, indicated by the horizontal lines, and two isothermal or constant electric field legs, indicated by the vertical black or dashed gray lines, respectively. The polarization is zero on the cool side of the cycle and nonzero on the hot side.

1.3 PHASE-FIELD MODELING

Phase-field modeling has been used extensively to model the structure of ferroelectric materials [4] and is the exclusive method used in this dissertation. It is a powerful computational approach to modeling microstructure evolution using a set of field variables that are continuous across the entire model. The advantage offered by phase-field modeling is its ability to predict complex material

microstructural evolution without explicitly tracking the domain and phase interfaces. For a review of the use of phase-field models for microstructure evolution in a variety of applications, see Chen [4].

Phase-field modeling describes the domain structure in ferroelectric materials by using the material polarization as an order parameter. This order parameter takes on a distinct value in each domain. For example, for the 180° bidomain shown in Fig. 1.5(a), the polarization transitions from the "up" poled domain, with positive polarization, to the "down" poled states with negative polarization. The transition between the two domains is smooth and has a finite width (width is discussed further in Chapter 3). Outside of the domain wall, the value of the order parameter, the polarization, is uniform. Many authors have tackled ferroelectric materials modeling with phase-field techniques. Hu and Chen [23] modeled three-dimensional domain formation and evolution in ferroelectric materials using a phase-field technique. Previous work by Landis and co-workers used a temperature-independent phase-field model to develop the continuum theory for domain evolution in ferroelectric materials and investigate the steady-state motion of domain walls and domain wall pinning [8]. Domain wall interaction with dislocations, domain switching near crack tips and domain structures in thin films were also investigated using this model [24]–[27]. Other work has focused on the temperature-dependent structure of ferroelectric materials. Li *et al.* studied the three-dimensional domain structure evolution of a constrained thin film

ferroelectric material through the paraelectric to ferroelectric transition [28] and developed a temperature-strain phase diagram for barium titanate thin films [29] using a semi-implicit Fourier spectral method. Cao and Cross [6] found homogenous analytical solutions for stress-free ferroelectric perovskites and provided the temperature ranges where only a single ferroelectric or paraelectric state is stable and ranges where both a metastable and a stable phase solution are possible. For an further review of the use of phase-field methods for domain evolution modeling in ferroelectric crystals, see Potnis [3].

1.4. OUTLINE

The remainder of this dissertation is outlined as follows. Chapter 2 develops the theoretical framework for the continuum phase-field model of the fully thermo-electro-mechanically coupled ferroelectric material based on a thermodynamic energy approach. The governing equations for electromechanics and microforce balance are combined with the first and second law of thermodynamics to yield constitutive relationships and governing equations for ferroelectric material behavior based on the free energy function. The theory expands on the work of Su and Landis [8], but now includes temperature dependence. The Helmholtz free energy function for the model is introduced and examined. Finally the finite element implementation of the phase-field model is discussed.

Chapter 3 presents the results of phase-field modeling of ferroelectric to paraelectric phase boundary structures in single-crystal barium titanate. The study

begins with an examination of the conditions necessary to create a stable ferroelectric to paraelectric phase boundary, including the selection of a ferroelectric laminate structure, the calculation of an electromechanically stable angled boundary and the application of entropy control via displacement boundary conditions. Simulations of the stable phase boundary are performed for a variety of laminate domain widths to determine the dependence of phase coexistence temperature, boundary energy, and entropy jump across the boundary on the laminate width. While only the 180° ferroelectric laminate is studied in detail, other options, both two- and three-dimensional, are discussed. Finally, we demonstrate the motion of the ferroelectric-paraelectric boundary under entropy/heat input control.

Chapter 4 presents the phase-field model of a proposed electrocaloric cooling device. First, we examine the literature on the use of multilayer capacitor style electrocaloric cooling devices to inform the geometry and boundary conditions of the proposed electrocaloric cooling device. The finite element simulation of the device follows the electrocaloric cooling cycle with two adiabatic and two constant electric field legs. The results of the cooling cycle simulation for the multilayer capacitor electrocaloric device is compared to the ideal cycle for a homogeneous plain strain electrocaloric material and the inefficiencies that arise in the device, including the formation of domains, high stress areas and incomplete material transformation, are discussed.

Chapter 5 explores the formation of vortex domains in ferroelectric nanodots upon cooling from a paraelectric state. The dots have a square base and are wider than they are tall. First, we document the effect on the domain structure of the dot of reducing the dot size while keeping the width constant. Then, the change in domain structure with further cooling to room temperature is shown. Finally, the use of nanodots in actuation is explored by applying an out-of-plane electric field to induce polarization and thereby shape change along the field direction.

Chapter 2: Thermodynamic derivation of phase-field model of thermo-electro-mechanically coupled ferroelectric material[1]

Phase-field modeling is a powerful computational technique used to predict the complex microstructure and the evolution of microstructure in materials. Phase-field modeling is well-suited to the study of ferroelectric materials, since ferroelectric ceramics are well known to have complex domain/phase structures that evolve with the application of electric fields, mechanical stress and/or temperature change. The phase-field model for the thermo-electro-mechanically coupled behavior of ferroelectric materials with a cubic to tetragonal phase transitions presented in this chapter is based on an expansion of the work by Su and Landis [8], which developed a thermodynamic framework for evolution of ferroelectric domain structures. We expanded the theory to include material temperature and temperature gradients as variables in the formulation. This allows for the modeling of the electrocaloric effect in ferroelectric ceramics. The thermodynamic framework is used in conjunction with a free energy function, which describes the material properties and behavior. A principle of virtual work is formulated for the theory and the nonlinear finite element equations are derived from it.

[1] Minor portions of this chapter were published in 2016 by A.Y. Wolman in collaboration with C.M. Landis [30]. C. M. Landis originally developed the theory presented in this chapter. All the written text, calculations and analysis was completed by A. Y. Woldman in consultation with C. M. Landis.

2.1 GOVERNING EQUATIONS FOR THE PHASE-FIELD MODEL

The development of the phase-field model begins with the consideration of the governing equations relevant to the problem. For a body of volume V, bounded by the surface S the conservation of linear and angular momentum for a quasi-static process dictates that

$$\begin{aligned} \sigma_{ji} n_j &= t_i \quad on\ S \\ \sigma_{ij} &= \sigma_{ji} \ \ in\ V \\ \sigma_{ji,j} + b_i &= 0 \ \ \ in\ V \end{aligned} \tag{2.1}$$

where σ_{ij} are the components of the Cauchy stress tensor, b_i are the components of the body force, n_i are the components of the unit normal to the surface and t_i are the components of the traction vector. Note that the above assumes that the acceleration of the body is zero, and therefore the problem is quasi-static. With the assumption of small deformations and small rotations, linear kinematics holds and therefore the strain-displacement relationship

$$\varepsilon_{ij} = \frac{1}{2}\left(u_{i,j} + u_{j,i}\right) \tag{2.2}$$

is used. Here, ε_{ij} are the components of the strain tensor and u_i are the components of the displacement vector.

Since the velocities considered in ferroelectric device applications are well below the speed of light, the quasistatic Maxwell's equations yields

$$D_{i,i} - q = 0 \quad in\, V$$
$$D_i n_i = -\omega \;\; on\, S \tag{2.3}$$
$$E_i = -\phi_{,i} \;\; in\, V$$

where D_i are the components of the electric displacement, q is the volume charge density, ω is the surface charge density and E_i and ϕ are the components of the electric field and electric potential, respectively. The electric displacement can be related to the electric field with the following equation,

$$D_i = P_i + \kappa_o E_i \;\; in\, V \tag{2.4}$$

where P_i are the components of the material polarization vector and κ_o is the permittivity of free space.

Phase-field modeling uses a set of field variables that describe the microstructure of the material. For ferroelectric materials, the natural field variables, or order parameters, as they are frequently referred to, are the components of the polarization. Within the phase-field approach, the polarization components are continuous but can vary sharply across a finite length scale, thus creating diffuse domain boundaries in the material. Diffuse boundaries are computationally tractable, since they allow microstructure evolution without the need to explicitly track interfaces. In phase-field modeling, the total free energy of the system is given by the combination of the energy of the bulk material and the interfacial energy, which is only nonzero near phase/domain transitions.

As first suggested by Gurtin [31], the laws of thermodynamics should account for work associated with each kinematic process. Thus the polarization components must have associated microforces that are work conjugate to the polarizations. Hence, the micro-'stress' tensor ξ_{ji} and the internal and external micro-'force' vectors f_i and π_i, respectively, are introduced. Consequently, $\xi_{ji}n_j\dot{P}_i$ is the power density expended across the surface of a material volume, $f_i\dot{P}_i$ is the power density expended by the surrounding regions on the material volume and $\pi_i\dot{P}_i$ is the power density expended by external forces on the material, where the notation $\dot{x}$ indicates a time derivative of the variable x. We also define the variable λ_i as an external applied surface micro-'force', with $\lambda_i = \xi_{ji}n_j$. An overall balance of this set of micro-forces is postulated as

$$\int_S \lambda_i dS + \int_V (f_i + \pi_i) dV = 0 \ . \tag{2.5}$$

Applying the divergence theorem and then assuming that the integral must be zero for any volume, the integrand gives the differential microforce balance

$$\xi_{ji,j} + f_i + \ \pi_i = 0 \quad in\, V \ . \tag{2.6}$$

Along with the above balance laws for electromechanics and microforces, the laws of thermodynamics are used to determine the final governing equations for the model. Expressing the first law as an integral equation with all the work and heat quantities relevant to our calculations, we arrive at the following expression

$$\frac{d}{dt}\int_V \tilde{u}dV = \int_S \left(t_i\dot{u}_i + \phi\dot{\omega} + \xi_{ji}n_j\dot{P}_i - \tilde{q}_i n_i\right)dS + \int_V \left(b_i\dot{u}_i + \phi\dot{q} + f_i\dot{P}_i + r\right)dV \ , \tag{2.7}$$

where $\tilde{u}$ is the internal energy density, $\tilde{q}_i$ are the components of the heat flux per unit area and r is the external supply of heat per unit volume. The left hand side of Eq. 2.7 gives the rate of change in internal energy while the right hand side gives the power expended by external sources on the body plus the heat entering and leaving the system. Expanding this equation using the relationships presented earlier in this chapter (Eqs. 2.2-2.6) and then once again applying the divergence theorem, the rate of change in internal energy density can be expressed in differential form as

$$\frac{d\tilde{u}}{dt} = \sigma_{ji}\dot{\varepsilon}_{ij} + E_i\dot{D}_i + \xi_{ji}\dot{P}_{i,j} - \pi_i\dot{P}_i + r - \tilde{q}_{i,i} \ . \tag{2.8}$$

The Second Law of Thermodynamics states that the entropy change of a closed system is greater than or equal to the heat input divided by temperature. Using the relevant quantities in this model, we rewrite the second law in integral form as

$$\frac{d}{dt}\int_V sdV \geq \int_V \frac{r}{\theta}dV - \int_S \frac{\tilde{q}_i n_i}{\theta}dS \tag{2.9}$$

where θ is the temperature and s is the entropy. Again, with the application of the divergence theorem, the second law can be simplified to the differential form

$$\theta \dot{s} \geq r - \tilde{q}_{i,i} + \frac{1}{\theta} \tilde{q}_i \theta_{,i} \, . \tag{2.10}$$

The derivation continues with the introduction of the electrical enthalpy, h, which can be derived from the Helmholtz free energy, ψ, by the equation

$$h = \psi - E_i D_i \ . \tag{2.11}$$

Looking ahead to the numerical implementation of the model, the electrical enthalpy is used so that the independent variables in the enthalpy expression can be directly derived from the nodal quantities (u_i, ϕ, P_i and θ) of the finite element implementation. To be as general as possible, the electrical enthalpy is allowed to depend on the ε_{ij}, E_i, P_i, $P_{i,j}$, $\dot{P}_i$, θ, $\theta_{,i}$ and $\dot{\theta}$. The calculations will show that h cannot depend on several of these quantities. Using the definition of Helmholtz free energy

$$\psi = \tilde{u} - \theta s \tag{2.12}$$

the expression for h can be rewritten as

$$h\left(\varepsilon_{ij}, E_i, P_i, P_{i,j}, \dot{P}_i, \theta, \theta_{,i}, \dot{\theta}\right) = \tilde{u} - \theta s - E_i D_i \, . \tag{2.13}$$

Taking the time derivative of Eq. 2.13 and combining it with the differential form of the first and second law of thermodynamics (Eqs. 2.8 and 2.10), the following inequality emerges

$$\left(\frac{\partial h}{\partial \varepsilon_{ij}} - \sigma_{ji}\right)\dot{\varepsilon}_{ij} + \left(\frac{\partial h}{\partial E_i} + D_i\right)\dot{E}_i + \left(\frac{\partial h}{\partial P_i} + \pi_i\right)\dot{P}_i$$

$$+\left(\frac{\partial h}{\partial P_{i,j}} - \xi_{ji}\right)\dot{P}_{i,j} + \left(\frac{\partial h}{\partial \dot{P}_i}\right)\ddot{P}_i + \left(\frac{\partial h}{\partial \theta} + s\right)\dot{\theta} + \left(\frac{\partial h}{\partial \theta_{,i}}\right)\dot{\theta}_{,i} \tag{2.14}$$

$$+\left(\frac{\partial h}{\partial \dot{\theta}}\right)\ddot{\theta} \leq -\frac{1}{\theta}\tilde{q}_i\theta_{,i} \ .$$

Since h is independent of $\dot{\varepsilon}_{ij}$, $\dot{E}_i$, $\dot{P}_{i,j}$, $\ddot{P}_i$, $\dot{\theta}_{,i}$ and $\ddot{\theta}$, the inequality is linear in these terms. Given that the expression must hold for all admissible processes, we extract the constitutive relationships

$$\sigma_{ji} = \frac{\partial h}{\partial \varepsilon_{ij}} \ , D_i = -\frac{\partial h}{\partial E_i} \ , \xi_{ji} = \frac{\partial h}{\partial P_{i,j}} \ , s = -\frac{\partial h}{\partial \theta} \tag{2.15}$$

and show that the electrical enthalpy is independent of the time derivative of the polarization, the time derivative of temperature, and the gradient of the temperature:

$$0 = \frac{\partial h}{\partial \dot{P}_i} \ , 0 = \frac{\partial h}{\partial \theta_{,i}} \ , 0 = \frac{\partial h}{\partial \dot{\theta}} \ . \tag{2.16}$$

Defining the quantity η_i as

$$\eta_i \equiv \frac{\partial h}{\partial P_i} \ , \tag{2.17}$$

the inequality is reduced to

$$(\eta_i + \pi_i)\dot{P}_i + \frac{1}{\theta}\tilde{q}_i\theta_{,i} \leq 0 \ . \tag{2.18}$$

The inequality in Eq. 2.18 is satisfied if the terms π_i and $\tilde{q}_i$ are given as

$$\pi_i = -\eta_i - \beta_{ij}\dot{P}_j - \frac{a_{ij}\theta_{,j}}{\theta} \tag{2.19}$$

and

$$\tilde{q}_i = -k_{ij}\theta_{,j} - \tilde{a}_{ij}\dot{P}_j \ , \tag{2.20}$$

where the matrix $\begin{bmatrix} \beta_{ij} & \frac{1}{\theta}a_{ij} \\ \frac{1}{\theta}\tilde{a}_{ij} & \frac{1}{\theta}k_{ij} \end{bmatrix}$ must be positive definite. Note that β_{ij}, k_{ij}, a_{ij}, and $\tilde{a}_{ij}$ can all depend on ε_{kl}, E_k, P_k, $P_{k,l}$, $\dot{P}_k$, θ, $\theta_{,k}$ and $\dot{\theta}$. Combining the expressions in Eqs. 2.19-2.20 with the inequality in Eq. 2.18 expands the inequality to

$$-\beta_{ij}\dot{P}_i\dot{P}_j - \frac{1}{\theta}a_{ij}\dot{P}_i\theta_{,j} - \frac{1}{\theta}\tilde{a}_{ij}\dot{P}_j\theta_{,i} - \frac{1}{\theta}k_{ij}\theta_{,i}\theta_{,j} \leq 0 \tag{2.21}$$

which can then be rewritten in matrix form as

$$-\begin{bmatrix} \dot{P}_i & \theta_i \end{bmatrix}\begin{bmatrix} \beta_{ij} & \frac{1}{\theta}a_{ij} \\ \frac{1}{\theta}\tilde{a}_{ij} & \frac{1}{\theta}k_{ij} \end{bmatrix}\begin{bmatrix} \dot{P}_j \\ \theta_{,j} \end{bmatrix} \leq 0 \ . \tag{2.22}$$

Obviously Eq. 2.22 is satisfied since the matrix of dissipative coefficients is positive definite. Equation 2.22 gives the most general form for the inequality, but is usually simplified by assuming that the off-diagonal submatrices are zero. Using the positive definite submatrices β_{ij} and k_{ij}, defined as the "polarization viscosity" and thermal conductivity, we write the reduce relationships for Eqs. 2.19 and 2.20 as

$$\begin{aligned} \eta_i + \pi_i &= -\beta_{ij}\dot{P}_j \\ \tilde{q}_i &= -k_{ij}\theta_{,j}\,. \end{aligned} \tag{2.23}$$

Equation 2.23(a) above describes the mobility of the polarization and is mainly used as a computational device to evolve the domains in towards equilibrium states in time. Equation 2.23(b) is equal to Fourier's Law of heat conduction, which states that the local heat flux in a material is proportional to the negative local gradient of the temperature.

We substitute the constitutive relationships in Eqs. 2.15-2.17 and the polarization mobility (Eq. 2.23(a)) into the momentum balance (Eq. 2.1), quasistatic Maxwell's equations (Eq. 2.3) and the microforce balance (Eq. 2.6) to get

$$\left(\frac{\partial h}{\partial \varepsilon_{ij}}\right)_{,j} + b_i = 0 \quad in\ V \tag{2.24}$$

$$\left(\frac{\partial h}{\partial E_i}\right)_{,i} = -q \quad in\ V \tag{2.25}$$

$$\left(\frac{\partial h}{\partial P_{i,j}}\right)_{,j} - \frac{\partial h}{\partial P_i} + f_i = \beta_{ij}\dot{P}_j \quad in\, V\,, \tag{2.26}$$

respectively. Equation 2.26 is the familiar Landau-Ginzburg equation, an evolution equations frequently used to model a variety of physical systems [31] . The energy balance of the first law of thermodynamics (Eq. 2.8) can also be rewritten using the constitutive relationships (Eqs. 2.15-2.17), polarization mobility and heat conduction equations (Eq. 2.23(b)) to yield

$$\begin{aligned}&\left(k_{ij}\theta_{,j}\right)_{,i} + \beta_{ij}\dot{P}_i\dot{P}_j + r \\ &\quad + \theta\left(\frac{\partial^2 h}{\partial\theta\partial\varepsilon_{ij}}\dot{\varepsilon}_{ij} + \frac{\partial^2 h}{\partial\theta\partial E_i}\dot{E}_i + \frac{\partial^2 h}{\partial\theta\partial P_i}\dot{P}_i + \frac{\partial^2 h}{\partial\theta\partial P_{i,j}}\dot{P}_{i,j} + \frac{\partial^2 h}{\partial^2\theta}\dot{\theta}\right) = 0\,,\end{aligned} \tag{2.27}$$

which is a thermo-electro-mechanical heat equation. The first term on the left-hand side of Eq. 2.27 is the familiar Fourier heat conduction term and the second and third terms represent the heat generated from polarization changes and any external heat sources. The final term represents a range of reversible heat source and sink effects from the thermally coupled behavior of the material. It is useful to compare Eq. 2.27 with the typical uncoupled form of the heat equation found as

$$C_p\dot{\theta} = \left(k_{ij}\theta_{,j}\right)_{,i} + r \tag{2.28}$$

where C_p is the volumetric heat capacity. When simplified using the calculations for the second derivatives of the electrical enthalpy (see Appendix A), Eq. 2.27 contains

all three terms from Eq. 2.28. However, there are three other non-zero terms, one stemming from the thermal expansion, another from coupling between the polarization and temperature (pyroelectricity), and finally the heat dissipation domain evolution $\beta_{ij}\dot{P}_i\dot{P}_j$.

Together, equations 2.24-2.27 give the full balance laws for mechanics, electrostatics, microforce, and heat conduction necessary for the solution of the fully-coupled thermo-electro-mechanical ferroelectric material problem. Since the constitutive laws are energy based, it is crucial that the chosen free energy function captures the properties of the ferroelectric material at a range of temperatures, including the Curie temperature.

2.2 HELMHOLTZ FREE ENERGY FUNCTION

Proceeding to the Helmholtz free energy function, we require that the function accurately model the piezoelectric, dielectric, elastic, and thermal properties of the material in both the tetragonal ferroelectric and cubic paraelectric state. Equation 2.29 below gives the general form of the free energy

$$\psi = \frac{1}{2}a_{ijkl}P_{i,j}P_{k,l} + \frac{1}{2}\bar{\alpha}_{ij}(\theta-\theta_0)P_iP_j + \frac{1}{4}\bar{\bar{\alpha}}_{ijkl}P_iP_jP_kP_l$$
$$+\frac{1}{6}\bar{\bar{\bar{\alpha}}}_{ijklmn}P_iP_jP_kP_lP_mP_n + \frac{1}{8}\bar{\bar{\bar{\bar{\alpha}}}}_{ijklmnrs}P_iP_jP_kP_lP_mP_nP_rP_s$$
$$+b_{ijkl}\varepsilon_{ij}P_kP_l + \frac{1}{2}c_{ijkl}\varepsilon_{ij}\varepsilon_{kl} + f_{ijklmn}\varepsilon_{ij}\varepsilon_{kl}P_mP_n \qquad (2.29)$$
$$+g_{ijklmn}\varepsilon_{ij}P_kP_lP_mP_n + \frac{1}{2\kappa_0}(D_i-P_i)(D_i-P_i)$$
$$+\tilde{\beta}_{ij}(\theta-\theta_1)\varepsilon_{ij} + C_P\left[(\theta-\theta_2) - \theta\ln\left(\frac{\theta}{\theta_2}\right)\right].$$

The first term in the free energy function penalizes large gradients in polarization and thereby gives rise to smooth phase/domain transitions that are the foundation of phase-field modeling. The ideal transition between phases is of finite width, minimizing the area over which the first term is non-zero, and smooth, minimizing the magnitude of the term with smaller gradients. Outside of the phase/domain boundaries, contributions from the first term are negligible.

The next four terms give the phenomenological Landau-Devonshire (LD) potential for a ferroelectric crystal. An eighth-order LD potential is used in this work. While the potential contains up to eighth-order tensors, it should be noted that every material tensor must have at least the symmetry of the highest symmetry phase: the paraelectric cubic phase. Therefore, $\bar{\alpha}$, $\bar{\bar{\alpha}}$, $\bar{\bar{\bar{\alpha}}}$, and $\bar{\bar{\bar{\bar{\alpha}}}}$ tensors reduce to one, two, three and four independent terms, respectively. The sixth-order LD potential was long popular for modeling ferroelectric behavior in $BaTiO_3$ and other

perovskite crystals [32]. However, calculations with both the paraelectric and ferroelectric phases showed that in fitting the nonlinear dielectric properties of the material near the phase transition, the coefficients of the LD potential are highly phase-dependent [33]. This suggests that the sixth-order is insufficient for modeling phase behavior near the Curie temperature, and thus an eighth-order LD potential is necessary to capture the full temperature-dependent behavior accurately [33], [34].

Since the energy landscape is dependent on the temperature, the coefficients in the LD potential can all depend on the temperature. Calculations from first principles suggested that for the sixth-order LD potential, all the coefficients in the expansion should be temperature dependent [32]. However, for this work, only the first term of the LD potential is taken to be linearly dependent on the absolute temperature, as shown explicitly in the free energy function above. Note that θ_0, which is simply a parameter of the model, is not equivalent to the Curie temperature θ_c. While other models with further temperature dependence in the $\bar{\bar{\alpha}}$ and $\bar{\bar{\bar{\alpha}}}$ coefficients have been proposed for sixth-order [35] and eighth-order [33] potentials, we choose to use the model presented by Li, *et al*, where only the $\bar{\alpha}$ coefficient is temperature-dependent [34]. This choice is made for computational stability and is justifiable since the temperature dependence of the phenomenological LD potential is based on curve-fitting the phase diagram and material properties to a phenomenological model and no "true" values for these coefficients exists.

The four terms following the LD potential in Eq. 2.29 are used to fit spontaneous strains and dielectric, elastic and piezoelectric properties of the material. The next term is the energy stored in the free space occupied by the ferroelectric material. The final two terms are used to fit the thermal expansion and the specific heat of the material. The numerical values of all the coefficients are determined from the literature and are given in the Appendix A.

The temperature-dependent term in Eq. 2.29 is responsible for altering the free energy from a single well at high temperatures to a multi-well structure at lower temperatures. A one-dimensional illustration of the free energy for a stress-free $BaTiO_3$ crystal as a function of the polarization is given in Fig. 2.1. The red arrows on each crystal in the nonzero energy wells indicate the orientation of the polarization for the minima. Alongside the free energy, an illustration of the polarization as a function of the electric field is also given for each temperature. Note that while the polarization vs. electric field curve presented is achieved using charge control on a $BaTiO_3$ monodomain, the application of electric fields directly to the crystal will induce spontaneous polarization jumps anytime the slope of the curve switches from positive to negative (see the ferroelectric hysteresis curve shown in Fig. 1.3(a)). At temperatures significantly above the Curie temperature, the free energy is minimized by the cubic paraelectric ($P = 0$) configuration. No other energy minima exist. The polarization is an approximately linear function of the electric field, with no hysteretic behavior of domain switching possible. As the

material cools, the two metastable ferroelectric energy minima form, but the paraelectric phase remains the global minimum. At this state, the ferroelectric phases can be induced with a sufficient application of a driving force, for instance with an applied electric field, and will remain stable at the higher energy state even after the electric field is removed if undisturbed by other outside forces. At exactly the Curie temperature, shown in Fig. 2.1(c), the pure ferroelectric and paraelectric phase are equally energetically favorable, suggesting that the two phases can stably coexist at zero stress and electric field. Coexistence at a single uniform temperature is a property of first-order phase transitions in perfect crystals. The polarization at this temperature is used to calculate the spontaneous polarization P_0, which is used for normalization throughout this dissertation. With continued cooling, the paraelectric phase becomes metastable and the ferroelectric polarization magnitude increases as the minima move away from one another on the P-axis. At temperatures significantly below the Curie temperature, the paraelectric phase becomes unstable and the energy is minimized by the tetragonal ferroelectric phases (two variants in the one-dimensional case, and six variants in the full three-dimensional case) with polarization $P = \pm P_S$, where P_S is a function of the temperature, increasing in magnitude as the temperature decreases. At this state, the behavior of the crystal is entirely ferroelectric, and the paraelectric cubic state is unstable under any electric field, as shown by the negative slope in the polarization vs. electric field plot at zero polarization.

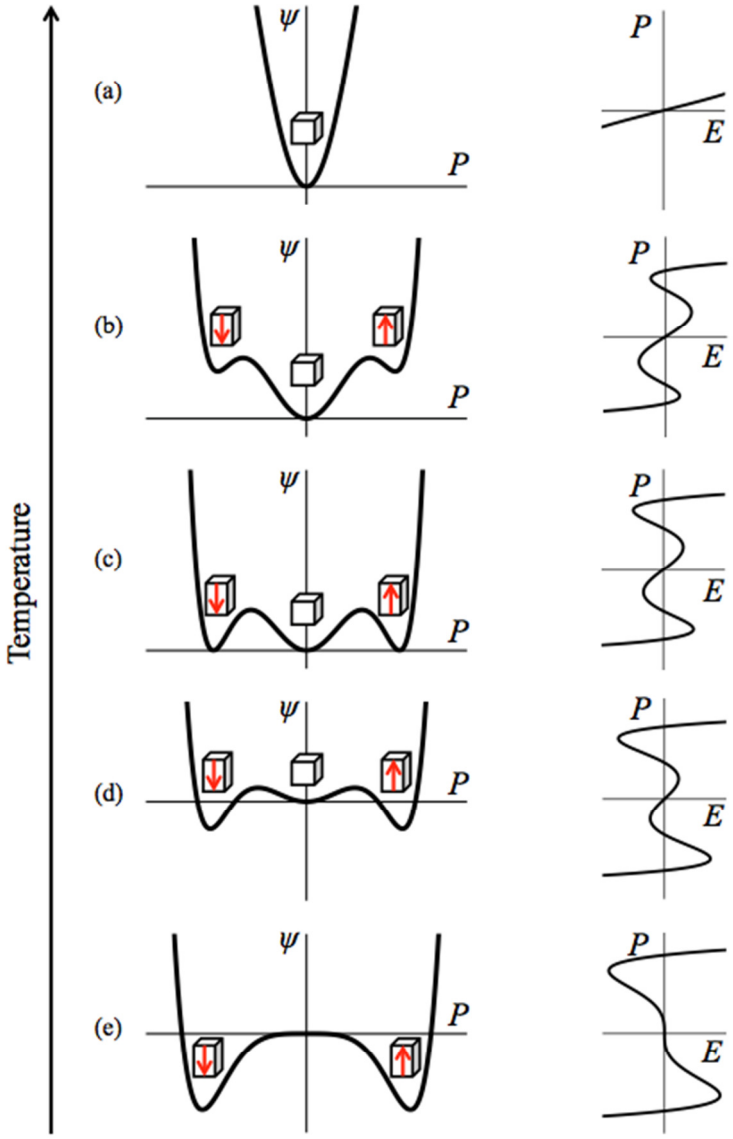

Figure 2.1: The energy minima of the Helmholtz free energy of $BaTiO_3$ as a function of temperature and the single crystal behavior of the polarization as a function of electric field at these temperatures. (a) Above the Curie temperature, the energy landscape has a single minimum at zero polarization, with the material in the paraelectric, cubic phase. (b) Upon cooling, metastable ferroelectric phases can form. (c) At the Curie temperature, the ferroelectric tetragonal and paraelectric cubic phases have equal energies. (d) Further cooling leads the paraelectric phase to become metastable. (e) Below the Curie temperature, the ferroelectric tetragonal state is energetically favorable and the paraelectric phase is unstable.

2.3 FINITE ELEMENT IMPLEMENTATION

Due to the highly nonlinear and coupled nature of the material behavior, an iterative finite element method is used to solve the model problems presented in this dissertation. The governing equations developed in Section 2.1, along with appropriate boundary conditions, provide the strong form of the finite element formulation. The nodal quantities for the finite element model are mechanical displacements, electric potential, polarizations and temperature (eight degrees of freedom for a full three-dimensional model). As discussed in Section 2.1, the electrical enthalpy h, is used, instead of the Helmholtz free energy, in order to allow the independent variables of h to be directly derived from the finite element interpolations of the nodal quantities.

To develop the weak form, we integrate the four governing differential equations (2.24-2.27) over the volume. Applying the divergence theorem and appropriate traction relationships for each equation gives rise to the four coupled weak forms for the finite element implementation of the thermo-electro-mechanical ferroelectric material model shown below:

$$\int_S t_i \delta u_i dS + \int_V b_i \delta u_i dV = \int_V \sigma_{ji} \delta \varepsilon_{ij} dV \tag{2.30}$$

$$\int_S -\omega \delta \phi dS + \int_V -q \delta \phi dV = \int_V -D_i \delta E_i dV \tag{2.31}$$

$$\int_S \lambda_i \delta P_i dS + \int_V f_i \delta P_i dV = \int_V \left\{ \xi_{ji} \delta P_{i,j} + \left(\eta_i + \beta_{ij} \dot{P}_j \right) \delta P_i \right\} dV \tag{2.32}$$

$$\int_S \frac{1}{\theta}\tilde{q}_i n_i \delta\theta dS + \int_V -\frac{1}{\theta}\left(r + \beta_{ij}\dot{P}_i\dot{P}_j\right)\delta\theta dV = \int_V \left(-\dot{s}\delta\theta + \frac{1}{\theta}\tilde{q}_i\delta\theta_{,i}\right) dV \ . \quad (2.33)$$

The familiar weak forms for mechanics and electrostatics (Eqs. 2.30-2.31) do not exhibit any time dependency. The microforce weak form (Eq. 2.31) exhibits time-dependence in the β_{ij} term. This implies that the time-dependence stems primarily from the motion of the domain/phase boundary motion, since the time derivative of polarization would remain relatively modest in the bulk of the domain. For static and isothermal finite element models, the β_{ij} term is used as a computational tool to evolve the polarization domains from the initial conditions towards a new equilibrium state, but β_{ij} is set to zero to find the final equilibrium (steady state) solution. Heat conduction, on the other hand, is naturally a time-dependent process, and the heat conduction weak form (Eq. 2.33) reflects that. Therefore, for any problems involving heat input and/or nonisothermal conditions, a general time-dependent weak form must be derived from the four equations above. The weak forms are combined by taking the time derivative of Eqs. 2.30-2.32 and adding them to Eq. 2.33 to get the combined principle of virtual work:

$$\int_S \left(\dot{t}_\iota \delta u_i - \dot{\omega} \delta \phi + \dot{\lambda}_i \delta P_i + \frac{1}{\theta} \tilde{q}_i n_i \delta \theta \right) dS$$

$$+ \int_V \left(\dot{b}_\iota \delta u_i - \dot{q} \delta \phi + \dot{f}_i \delta P_i - \frac{1}{\theta} (r + \beta_{ij} \dot{P}_i \dot{P}_j) \delta \theta \right) dV \tag{2.34}$$

$$= \int_V \Big(\dot{\sigma}_{ji} \delta \varepsilon_{ij} - \dot{D}_i \delta E_i + \dot{\xi}_{ji} \delta P_{i,j} + (\dot{\eta}_i + \beta_{ij} \ddot{P}_j) \delta P_i - \dot{s} \delta \theta$$

$$+ \frac{1}{\theta} \tilde{q}_i \delta \theta_{,i} \Big) dV \, .$$

It should be noted that the final term in Eq. 2.34 presents a computational inconvenience because it includes the temperature, a degree of freedom in the problem, and heat flux per unit area, a derived quantity that arises from the gradient of the temperature. To simplify this coupled term, we assume that the temperature range (measured in Kelvin) is small relative to the absolute value of the temperature, and therefore replace the θ in the final term with θ_C, the constant Curie temperature of the material, around which all of the computations will take place. Should the simulations be centered about a different temperature, this would need to be adjusted.

The principle of virtual work presented in Eq. 2.34 can be used for solving problems with gradients in temperature and nonzero heat input. However, isothermal calculations are also useful in evaluating the behavior of ferroelectric ceramic materials. The following simplified isothermal principle of virtual work may then be used,

$$\int_V \left(\sigma_{ji}\delta\varepsilon_{ij} - D_i\delta E_i + \xi_{ji}\delta P_{i,j} + \left(\eta_i + \beta_{ij}\dot{P}_j\right)\delta P_i\right)dV$$
$$= \int_S (t_i\delta u_i - \omega\delta\phi + \lambda_i\delta P_i)dS + \int_V (b_i\delta u_i - q\delta\phi + f_i\delta P_i)dV \ . \tag{2.35}$$

Equations 2.34 and 2.35 are the foundation for the development of the finite element equations for the phase-field model of ferroelectric ceramics in non-isothermal and isothermal conditions, respectively. The finite element implementation for the more general non-isothermal case is derived here, but a similar process can be followed to implement the isothermal case. As mentioned before, mechanical displacement, electric potential, polarization, and temperature are used as the nodal degrees of freedom for the finite element method. The strain, electric field, polarization gradients and thermal gradients can be computed within each element from the gradients of the nodal degrees of freedom. The stress, electric displacement, microforces, and entropy and heat flux can then be computed from Eqs. 2.15 and 2.23, using the appropriate material properties.

For the finite element implementation, the weak form (the principle of virtual work statement) must be expanded to describe the time-derivatives as functions of the computed quantities. The backward Euler scheme is used to compute the first time-derivatives

$$\dot{x} = \frac{x^{t+\Delta t} - x^t}{\Delta t} \tag{2.36}$$

where x is any degree of freedom or derived value that has a time derivative in the weak form. The second derivative terms, which only apply to the polarization degrees of freedom, are calculated by the central difference approximation

$$\ddot{P}_i = \frac{P_i^{t+\Delta t} - 2P_i^t + P_i^{t-\Delta t}}{\Delta t^2} \tag{2.37}$$

where the time $t + \Delta t$ is the unknown solution to the current time step, while t and $t - \Delta t$ are the known results from the two previous steps. This requires that any problem is initialized with some reasonable initial state for the polarization and then evolved in time from there. The expanded weak form is then rearranged such that all known values computed from previous time steps are on one side of the equation and all functions of unknown values, the nodal degrees of freedom and terms derived from them at $t + \Delta t$, are on the other side.

A Newton-Raphson-type method is employed to solve the nonlinear finite element problem. The vector problem described above can then be written generically as

$$LHS = RHS \rightarrow \boldsymbol{F} = \boldsymbol{N}(\boldsymbol{d}^{t+\Delta t}) \tag{2.38}$$

where $\boldsymbol{F}$ and $\boldsymbol{N}$ are the nonlinear algebraic functions describing the left- and right-hand-side of the expanded and rearranged weak form. The nodal quantities, displacement, potential, polarization and temperature, are generically referred to as the vector $\boldsymbol{d}$, and the superscript indicates the time step. The length of both $\boldsymbol{F}$ and $\boldsymbol{N}$

is equal to the number of unknown nodal quantities in the problem. While $\boldsymbol{F}$ is also a nonlinear function of the nodal degrees of freedom, it is only dependent on the known quantities at time t and $t - \Delta t$, and can be computed explicitly. Equation 2.38 has no obvious matrix solution, so we must linearize $\boldsymbol{N}$ using a Taylor expansion. Since the solution for $\boldsymbol{d}$ is determined using an iterative process, we write the Taylor expansion for the value of $\boldsymbol{N}$ for the n+1 iteration of $\boldsymbol{d}$, centered about the nth iteration for $\boldsymbol{d}$ as shown here:

$$\boldsymbol{N}\left(\boldsymbol{d}_{n+1}^{t+\Delta t}\right) = \boldsymbol{N}(\boldsymbol{d}_{\boldsymbol{n}}^{\boldsymbol{t}+\boldsymbol{\Delta t}}) + \left.\frac{\partial \boldsymbol{N}}{\partial \boldsymbol{d}}\right|_{\boldsymbol{d}_n^{t+\Delta t}} \Delta \boldsymbol{d} + \cdots . \tag{2.39}$$

The n subscript in Eq. 2.39 gives the iteration in the Newton-Raphson solution scheme. The ellipsis represents the presence of higher order terms in the Taylor expansion, which are ignored in this case since we are interested purely in the linearization of the system. Combining the Taylor expansion in Eq. 2.39 with Eq. 2.38 and rearranging the terms, we get the matrix equation

$$\boldsymbol{F} - \boldsymbol{N}(\boldsymbol{d}_n^{t+\Delta t}) = \left.\frac{\partial \boldsymbol{N}}{\partial \boldsymbol{d}}\right|_{\boldsymbol{d}_n^{t+\Delta t}} \Delta \boldsymbol{d} \tag{2.40}$$

where the generic term $\boldsymbol{N}(\boldsymbol{d}^{t+\Delta t})$ from Eq. 2.38 is replaced with $\boldsymbol{N}\left(\boldsymbol{d}_{\boldsymbol{n+1}}^{\boldsymbol{t}+\boldsymbol{\Delta t}}\right)$, which uses the most up-to-date value for the vector $\boldsymbol{d}$. Equation 2.40 can be rewritten generically as

$$\boldsymbol{R} = \widetilde{\boldsymbol{K}}\Delta\boldsymbol{d} \tag{2.41}$$

where $\boldsymbol{R}$ is the residual vector, $\widetilde{\boldsymbol{K}}$ is the square consistent tangent matrix and $\Delta\boldsymbol{d}$ is an incremental change in the nodal quantities computed at each Newton-Raphson iteration. When the Newton-Raphson scheme converges to the solution for $\boldsymbol{d}$, $\boldsymbol{N}(\boldsymbol{d}_{\boldsymbol{n}}^{\boldsymbol{t}+\Delta\boldsymbol{t}})$ converges to the true value of $\boldsymbol{N}$ for that time step, and the left-hand-side of Eq. 2.40 is equal to zero. Therefore, as $\boldsymbol{d}$ approaches the solution for the system, the residual $\boldsymbol{R}$, the left-hand-side of the equation, goes to zero. The consistent tangent shown in Eq. 2.41 is the analogue of the stiffness matrix in a linear elasticity problem. Since the consistent tangent is dependent on the nodal variables, it changes with each iteration of the Newton-Raphson scheme, as well as with time. Note that for this particular problem, the consistent tangent, as derived, is only perfectly symmetric for the isothermal case. For the non-isothermal case, the stiffness term relating the microforce (polarization) and temperature causes a slight asymmetry (the asymmetry is small compared to the magnitude of the term). However, since the matrix is close to symmetric, and the consistent tangent is merely a computational tool to arrive at the correct solution iteratively, a symmetric assumption is made for the sake of computational efficiency and only terms on and above the diagonal are used to compute $\widetilde{\boldsymbol{K}}$.

Equation 2.41 presents a method of solving for the change in the nodal variables from the computation of the residual and the consistent tangent. To solve for the true value of the nodal variables for the current time step, the nodal values

are updated incrementally using the formula $\boldsymbol{d}_n = \boldsymbol{d}_{n-1} + \Delta\boldsymbol{d}$ until the residual meets a convergence criteria set in the algorithm, at which point the value of $\boldsymbol{d}_n$ is determined to be the solution for that time step, $t + \Delta t$. With the new nodal values for displacement, potential, polarization and temperature, the next time step can be solved using equation Eq. 2.41 with the updated residual, consistent tangent and nodal values. A schematic of the iterative solution method is shown in Fig. 2.2. For sufficiently large models, the solution of the matrix equations requires the use of computational packages such as PETSC and supercomputing capabilities.

$n = 0, t = 0$

Initialize $\boldsymbol{d}$

Time loop (t)

Compute $\boldsymbol{F}$

Newton-Raphson Loop (n)

Update $\boldsymbol{d}_n = \boldsymbol{d}_{n-1} + \boldsymbol{\Delta d}$

Compute current estimate for $\boldsymbol{N}(\boldsymbol{d}_n)$

$\boldsymbol{R} = \boldsymbol{F} - \boldsymbol{N}(\boldsymbol{d}_n)$

Compute $\tilde{\boldsymbol{K}}$

Solve $\boldsymbol{R} = \tilde{\boldsymbol{K}}\boldsymbol{\Delta d}$

CONVERGENCE TESTS
$||\boldsymbol{R}|| \leq \varepsilon_R$
$||\boldsymbol{\Delta d}|| \leq \varepsilon_d$

Not converged → $n = n + 1$
continue in Newton-Raphson Loop

If converged → $\boldsymbol{d}_n = \boldsymbol{d}^{t+\Delta t}$, $t = t + \Delta t$
break Newton-Raphson Loop, continue to time loop

Figure 2.2: The schematic of the nonlinear finite element solution algorithm for the model. The solution evolves in time. The values for the convergence checks ε_R and ε_d are set in the code.

Chapter 3: Phase-field modeling of ferroelectric to paraelectric phase boundary structures in single-crystal barium titanate[2]

In this chapter, the stable boundary between ferroelectric (FE) and paraelectric (PE) phases is analyzed. Since the two phases can theoretically coexist near the Curie temperature, we look for model geometries in two and three dimensions that would accommodate a quasi-planar phase boundary and the boundary conditions necessary to keep it stable. The focus of this chapter is on a two-dimensional model of the quasi-planar FE-PE boundary under generalized plane strain and with zero average in-plane stress, although other two- and three-dimensional structures are discussed briefly. A nonlinear finite element method is used to solve for the phase boundary structure of a representative unit cell with a 180° ferroelectric laminate for a range of domain widths. The phase coexistence temperature, the excess free energy density of the boundary and the shape of the closure domains are computed as a function of the FE laminate domain width. The entropy jump across the phase boundary, which is a measure of the electrocaloric effect, is quantified. Finally, the motion of the phase boundary under entropy control is demonstrated.

[2] Large portions of this chapter where previously published in 2016 by A.Y. Wolman in collaboration with C. M. Landis [30]. The text was written by A. Y. Woldman, and edited and modified by C. M. Landis. All the calculations and simulations were performed by A. Y. Woldman in consultation with C. M. Landis. The interpretation of the results and the discussion were done collaboratively by both authors.

3.1 TWO-DIMENSIONAL FE-PE PHASE BOUNDARY MODEL GEOMETRY

Using the phase-field methods and equations developed in Chapter 2, we model the FE-PE phase boundary in the single crystal ferroelectric perovskites barium titanate ($BaTiO_3$). FE-PE phase boundaries were predicted and experimentally observed for semiconducting ferroelectric crystals like $KTa_{0.65}Nb_{0.35}O_3$ and cerium doped $BaTiO_3$ [36], [37]. Phase boundaries in semiconducting ferroelectric crystals are subject only to crystallographic compatibility constraints due to the availability of free charge to balance the spontaneous polarization. Here, we focus on the phase boundary of non-conducting $BaTiO_3$ single crystals. Since the boundary must be electrically and mechanically compatible, we expect it to be diffuse and complex in structure, and therefore well-suited to modeling with a phase-field approach.

Barium titanate exhibits a first-order phase transition [6], [15], allowing for the coexistence of the ferroelectric and paraelectric phases, as shown in the free energy diagram in Fig 2.1(c). Figure 3.1 illustrates an analogy between the coexistence of two domains of opposite polarization, separated by a domain wall, and the existence of two phases, paraelectric and ferroelectric, separated by a phase boundary. The ideal single-crystal ferroelectric 180° bidomain is stable only under charge control (Q) at zero voltage (V). The amount of charge on the electrodes dictates the relative volume of each phase variant. The solid line in Fig. 3.1(a) illustrates the charge-voltage response in a crystal *without* defects, lattice friction, or

other pinning sites that lead to the well-known hysteresis loop in such materials (shown by the dashed lines). Hence, there is a unique voltage, $V = 0$, at which both domain types can coexist. Any voltage different from $V = 0$ has a monodomain equilibrium structure. Analogously, the ideal single-crystal FE-PE phase boundary exists only under entropy/heat input control (S) at the transition temperature. As heat is expelled from the crystal, the volume fraction of the ferroelectric phase increases. Again, just as there is a unique voltage where a bidomain can exist in an ideal ferroelectric crystal, there is a theoretical unique temperature where a FE-PE phase boundary can exist in an idealized crystal undergoing a first order phase transition. Any deviation of the temperature from the transition temperature will result in a single phase. Prior works that studied phase and domain structures [28], [29] near the Curie temperature have not observed such phase boundaries due to the absence of entropy/heat input control in those studies. In those studies temperature control is used which does not lend itself to finding and isolating phase boundaries. In this work, entropy control is achieved by the careful selection of the electromechanical boundary conditions such that the phase boundary is in a neutral equilibrium position within the bulk of the crystal. To validate the existence of such boundaries under entropy/heat control, the model is expanded to include temperature as a degree of freedom and the motion of the phase boundary is demonstrated by controlling the heat input.

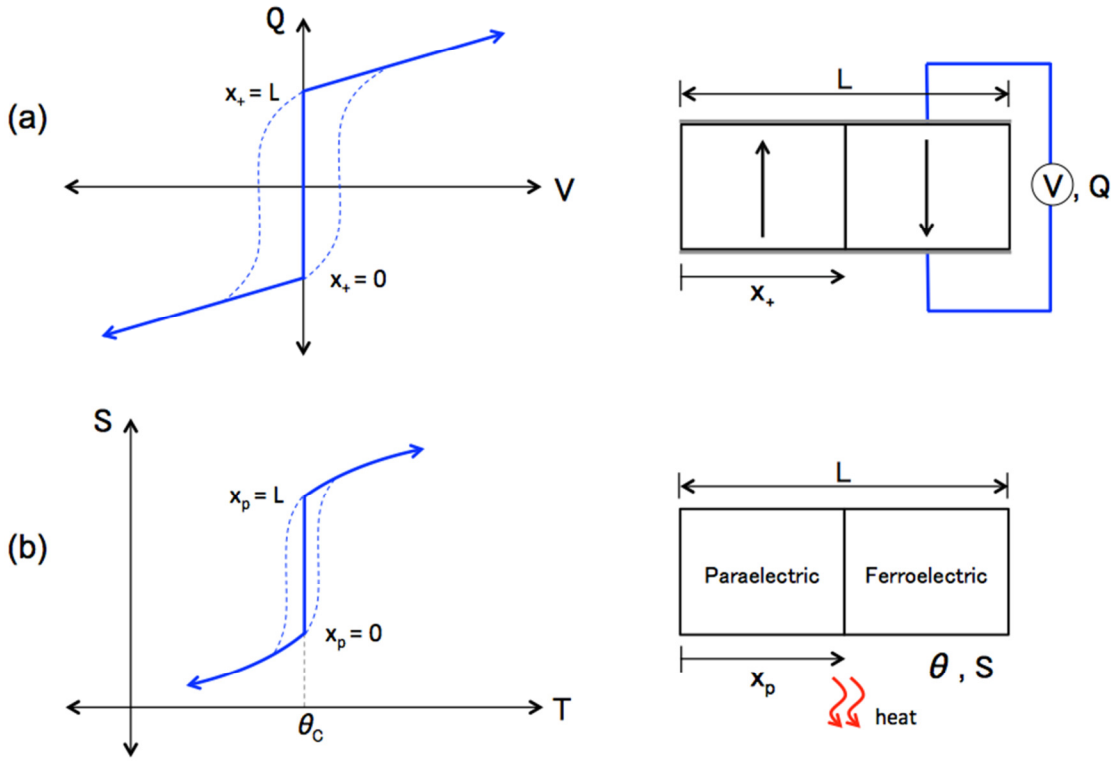

Figure 3.1: The analogy between the ideal 180° ferroelectric bidomain and stable FE-PE boundary. (a) The ideal ferroelectric single crystal bidomain sandwiched by two electrodes is only stable using charge (Q) control at zero voltage (V). The dashed lines represent the well-documented hysteresis behavior seen in non-ideal crystals where pinning and lattice friction hinder domain wall motion. Analogously, (b) the ideal ferroelectric-paraelectric phase boundary in a single crystal with a first order phase transition is only stable with entropy (S) control, at a transition temperature (θ_C). Heat is expelled or absorbed as the boundary moves through the crystal. The dashed line represents the hysteresis behavior seen in non-ideal crystals.

Previous work on the electrocaloric effect and the electrocaloric properties of $BaTiO_3$ inform the formulation of the electrical, mechanical, and thermal conditions and constraints required for the FE-PE phase boundary computations. The electrocaloric effect is maximized at operating temperatures near the Curie

temperature (due to the entropy jump/latent heat at the phase transition) and when allowed to proceed through a discontinuous phase transition [13]. Such discontinuous transitions necessitate the existence of an FE-PE phase boundary that travels through the material. To predict the shape of the FE-PE phase boundary, we turn to the crystallographic theory of martensite [38]. First, we reduce the dimensionality of the problem to a two-dimensional structure by assuming generalized plane strain. The strain $\varepsilon_{zz} = \varepsilon_{zz}^{*}$ is chosen such that at the Curie temperature, the paraelectric and ferroelectric *monodomain* energies are equal, as they are in a bulk unconstrained crystal. Next, we find a plane parallel to the *z*-axis (a line in the *x*-*y* plane) such that averaged electrical and mechanical compatibility between the cubic paraelectric and tetragonal ferroelectric phases is satisfied. For a semiconducting material, only mechanical compatibility must be met across the boundary, since a single charged plane can exist between the ferroelectric and paraelectric phases without the need for a complex domain structure [36], [37]. The predicted structure for a non-conducting ferroelectric perovskites is shown in Fig. 3.2. Electrical compatibility is met by choosing the convenient 180° ferroelectric rank-1 laminate with the domain width defined by the length scale w, a prescribed quantity. The 180° laminate is electrically compatible, in an averaged sense, with the pure paraelectric phase along any angled plane not parallel to the domain walls. However, closure domains are expected to form to resolve the pointwise electrical incompatibilities that form at the phase boundary interface [39].

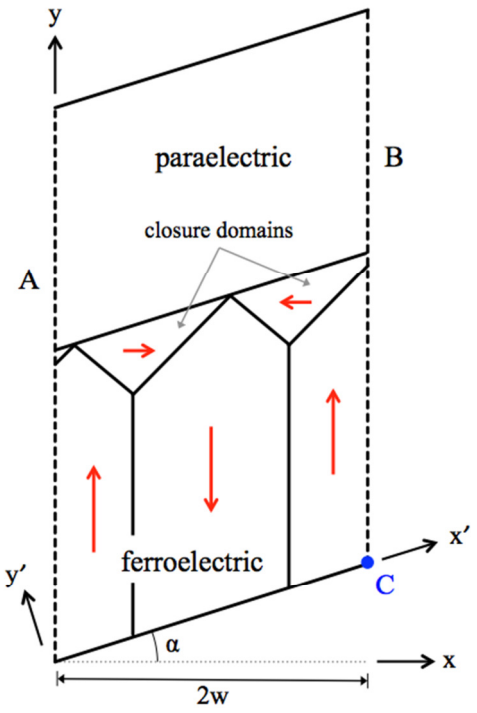

Figure 3.2: The postulated structure of a unit cell for a two-dimensional ferroelectric-paraelectric phase boundary. The full height of the structure is split equally into a lower ferroelectric and an upper paraelectric portion. The ferroelectric portion is composed of a rank-1 laminate with domain width w and equal areas of "up" and "down" polarized ferroelectric material. The phase boundary is at angle α with respect to the x-axis. Closure domains are expected to form in the transition between the two phases. Red arrows indicate the direction of the polarization vector in each region. Periodic boundary conditions are applied along the dashed lines at boundary A and B.

The mechanically compatible plane lies at an angle α with respect to the x-axis and is derived by requiring that the axial strain tangential to this plane in the paraelectric phase is equal to the same strain component in the ferroelectric phase. Hence, the angle α satisfies the strain transformation equation

$$\varepsilon_{x'x'} = \varepsilon_{xx}\cos^2\alpha + \varepsilon_{yy}\sin^2\alpha + \gamma_{xy}\sin\alpha\cos\alpha \tag{3.1}$$

to yield the relationship for the angle of the boundary

$$\alpha = \pm\arctan\sqrt{-\frac{\varepsilon_p - \varepsilon_a}{\varepsilon_p - \varepsilon_c}} \tag{3.2}$$

where $\varepsilon_{x'x'} = \varepsilon_p$ is the equibiaxial in-plane strain of the paraelectric phase, $\varepsilon_{xx} = \varepsilon_a$ and $\varepsilon_{yy} = \varepsilon_c$ are the average strains of the ferroelectric laminate, and the shear, γ_{xy}, is zero. The strains ε_a and ε_c are calculated for each domain width such that a 180° ferroelectric laminate domain has zero average in-plane stress, electric field, and electric displacement. Note that within a 180° domain wall the polarization and the stress-free strain (see Eq. (A2)) go to zero. However, the axial strain parallel to the walls must be equal to that in the neighboring bulk domains, which causes the walls to be in tension. Overall the average in-plane stress in the laminate is zero and hence there is a small level of compressive stress in the bulk domains parallel to the walls. This feature causes the values for the laminate strains ε_a and ε_c to have a weak dependence on the domain width. In contrast, the value of ε_p is independent of domain width and is constant for all cases. Note, however, that ε_P is not zero with respect to the three-dimensional stress and electric field-free paraelectric state because of the imposed nonzero generalized plane strain.

Boundary conditions are applied to the FE-PE structure to create an average in-plane field-free state. Periodic boundary conditions are applied on the dashed

lines (side A and B) in Fig. 3.2. The periodicity occurs along lines at angle α, parallel to the top and bottom edges of the model, i.e. along the x'direction. The periodic boundary conditions are:

$$\begin{aligned} \phi^B &= \phi^A \\ P_x^B &= P_x^A \\ P_y^B &= P_y^A \\ u_{x'}^B &= u_{x'}^A + \varepsilon_p \frac{2w}{\cos\alpha} \\ u_{y'}^B &= u_{y'}^A + \overline{\frac{\partial u_{y'}}{\partial x'}} \frac{2w}{\cos\alpha} \ . \end{aligned} \tag{3.3}$$

On the top paraelectric (P) and bottom ferroelectric (F) edge of the structure, the following boundary conditions are applied to the electric potential and displacement

$$\begin{aligned} \phi^F &= 0 \\ u_x^F &= \varepsilon_a x \\ u_y^F &= \varepsilon_c y \\ u_x^P &= \varepsilon_p x - \omega_0 y + u_x^0 \\ u_y^P &= \varepsilon_p y + \omega_0 x + u_y^0 \end{aligned} \tag{3.4}$$

where ω_0 is the rotation of the paraelectric material caused by the deformation in the ferroelectric material, and u_x^0 and u_y^0 are rigid body translations. The rigid body

motion is computed assuming a perfect planar boundary between the FE and PE phases located halfway up model height. Details on the values of ω_0, u_x^0, and u_y^0 can be found in the Appendix A. A Neumann boundary condition is applied to the potential degrees of freedom to enforce a charge-free condition along the top edge of the model. The boundary conditions in Eq. 3.4 are necessary to stabilize the paraelectric and ferroelectric regions at the top and bottom of the model, respectively, and mimics the conditions required for semi-infinite phases on either side of the boundary. The displacement conditions along the top and bottom boundaries are employed to control the exact total entropy for the model, and dictate that the volume fraction of each phase is half of the total volume.

Finally, let us note that the phase-field model has a characteristic length scale associated with the diffuse domain and phase boundaries, defined as

$$l_0 = \sqrt{\frac{a_0 P_0}{E_0}} \tag{3.5}$$

where a_0 is the nonzero coefficient of the first term in Eq. (2.29), P_0 is the spontaneous polarization and E_0 is electric field needed to trigger 180° domain switching in a monodomain. P_0 and E_0 are computed from the free energy density function at the Curie temperature (see Appendix B). To resolve domain walls in the computational model, the mesh size must be at least $l_0/4$ at the phase and domain boundaries.

3.2 PHASE BOUNDARY STRUCTURE

The structure predicted by the crystallographic theory of martensite and shown in Fig. 3.2 is used as an initial condition to find the steady-state configuration of the FE-PE phase boundary. Since nothing is known a priori about the shape and size of the closure domains, they are excluded from the initial state. The area is discretized into parallelogram-shaped linear two-dimensional elements, with a total of 5000-17000 elements, depending on the domain width. The mesh is highly refined at the domain walls (approximately eight elements span a wall) and around the phase boundary. At the Curie temperature, the ferroelectric and paraelectric *monodomains* have equal energy. However, the ferroelectric multi-domain *laminate* includes domain walls that are at a higher energy state than the bulk regions. The existence of domain walls causes the average free energy density in the ferroelectric laminate, as a whole, to increase. We define the phase coexistence temperature as the temperature at which, for a given domain width, a stable in-plane FE-PE phase boundary can be found with no in-plane mechanical or electrical applied loadings. At this phase coexistence temperature, the average free energy density of the ferroelectric laminate and the paraelectric monodomain are equal. Figure 3.3 shows that as the domain width increases, with the domain walls accounting for a smaller area of the overall ferroelectric laminate, the phase coexistence temperature asymptotically approaches the Curie temperature, θ_c. Conversely, as the domain width decreases, there is a point at which the stress-free phase coexistence

temperature cannot be found because the high energy and internal tension of the domain walls no longer allow the laminate to remain, on average, stress-free. The maximum polarization in the laminate $P_{\max}$ also increases with the model domain width, exactly following the trend of the phase coexistence temperature. $P_{\max}$ asymptotically approaches $0.891P_0$, the value of the spontaneous polarization at the Curie temperature under the imposed generalized plane strain conditions.

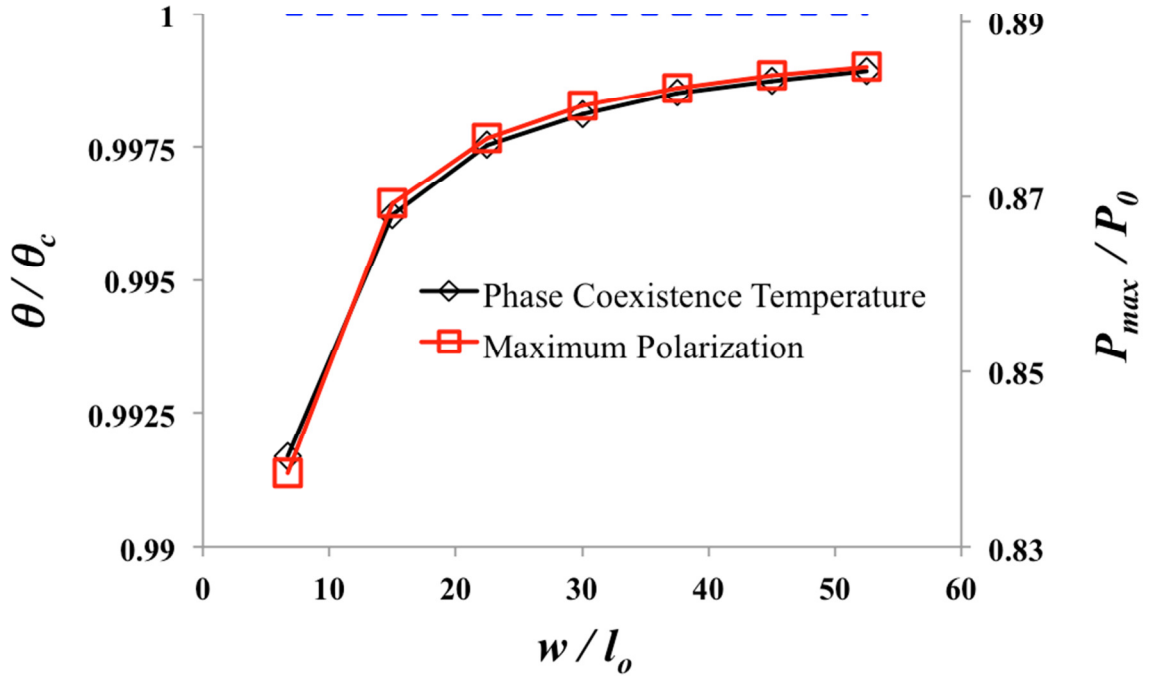

Figure 3.3: The phase coexistence temperature θ of the ferroelectric-paraelectric boundary is a function of the domain width of the ferroelectric laminate, w. As domain width increases, the phase coexistence temperature asymptotically approaches the Curie temperature θ_C, shown by the dashed blue line. The maximum polarization in the ferroelectric laminate follows the same trend, with P_{max} increasing with the domain width and approaching the asymptote of $P_{max} = 0.891\ P_0$.

For all domain widths, the model has a height that is ten times the domain width. This ensures the model edges are sufficiently far from the phase boundary and do not affect its structure. The polarization distribution shown in Fig. 3.4(a)-(c) illustrates the structure of the FE-PE phase boundary for a model with domain width $15l_0$. Far from the phase boundary, the polarization fields are invariant in the *y*-direction, as demonstrated by the plot in Fig. 3.4(d), highlighting that the boundary conditions at the top and bottom of the model do not affect the structure of the boundary, but only dictate the entropy level that allows for approximately equal volumes of the ferroelectric and paraelectric phases. The phase boundary is well defined, with a clear ferroelectric phase with $|\boldsymbol{P}| \neq 0$ below and paraelectric phase with $|\boldsymbol{P}| = 0$ above the phase boundary. The *x*-polarization is effectively zero outside of the phase boundary. As postulated, *x*-aligned closure domains form in the phase boundary, with fairly sharp transitions at the triple junction, and more diffuse transitions between the closure domains and the paraelectric phase. Localized nonzero electric fields form in the phase boundary, but the overall average in-plane electric field remains zero.

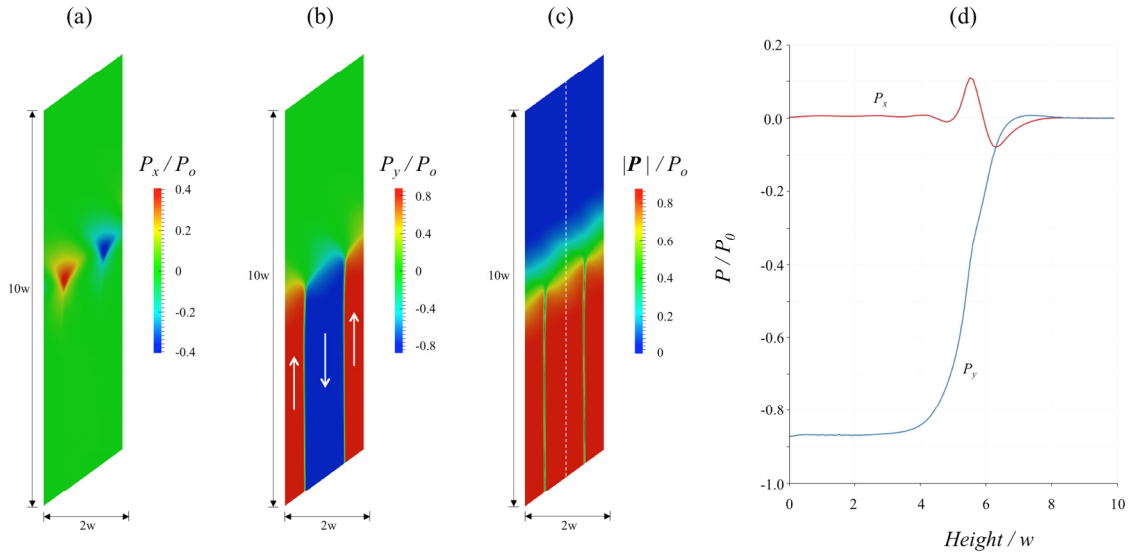

Figure 3.4: The (a) x- and (b) y-direction polarization and (c) and the magnitude of the polarization vector of the ferroelectric-paraelectric phase boundary under generalized plane strain with $\varepsilon_{zz} = \varepsilon_{zz}^*$. The polarization values are normalized by the spontaneous polarization P_0. The lower half of the structure is composed of a 180° rank-1 ferroelectric laminate, where the white arrows in (b) indicate the direction of polarization vector. The average in-plane stresses, electric fields and electric displacements of the structure are zero. The variations of the polarization along the dashed vertical line in (c) are shown on the plot in (d), indicating that the polarization is invariant along the y-direction far from the phase boundary.

Figure 3.5 presents the excess free energy per unit area in the FE-PE phase boundary structure as a function of the domain size. The excess free energy per unit area is defined as

$$\psi_{excess} = \frac{1}{A}\int_A \psi \, dA - \psi_o \qquad (3.6)$$

where ψ_0 is the averaged free energy per area of the 180° ferroelectric laminate and the paraelectric monodomain far from the phase boundary. The excess energy and

ψ_0 are computed at the domain width-dependent phase coexistence temperature given in Fig. 3.3. The excess energy (which is a measure of the energy of the boundary) increases with the domain width, as show in the inset in Fig. 3.5, indicating that a finer domain structure produces the lowest excess energy. Moreover, the trend in the excess free energy per area indicates that the total free energy density of the structure is domain size-dependent. While the free energy density of the paraelectric and ferroelectric regions must be equal, independent of size, the energy of the boundary cannot be quantified without a specified domain size.

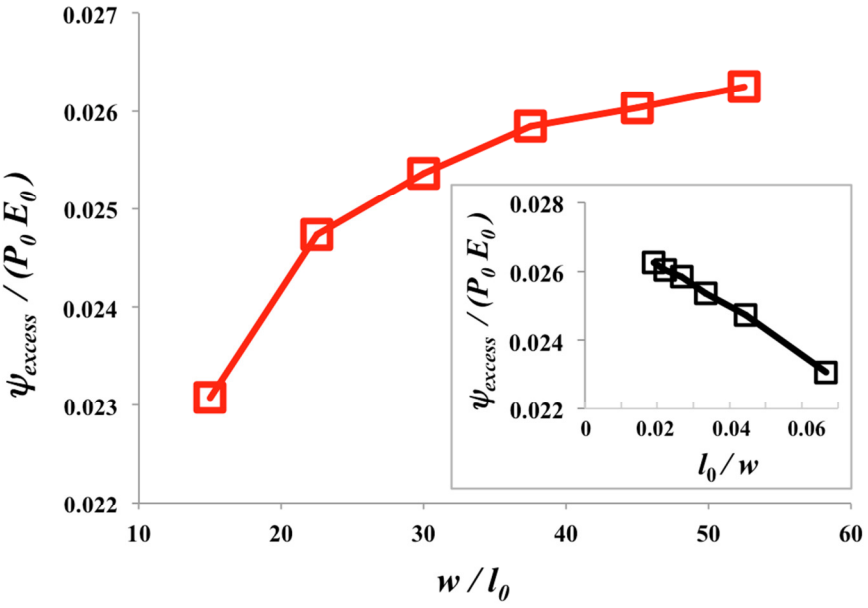

Figure 3.5: The excess Helmholtz free energy per unit area of the equilibrium 180° laminate ferroelectric-paraelectric boundary structure as compared to the pure paraelectric state and ferroelectric laminate phase far from the boundary as a function of the ferroelectric domain size w. Each structure was examined at the phase coexistence temperature shown in Fig. 3.3. The inset plot shows that the excess energy is a linear function of the reciprocal of the domain width w, with an asymptote at $\psi_{excess} = 0.0275\ P_0 E_0$.

For the stable FE-PE boundary shown in Fig. 3.4, the entropy distribution is nonuniform, increasing as the material transitions from ferroelectric to paraelectric. The excess entropy is a measure of the strength of the electrocaloric effect [15] and is directly related to the heat absorbed or expelled as the phase boundary moves between the paraelectric and ferroelectric phases. Using the definition of entropy given in Eq. 2.15, we define the line-averaged excess entropy as a function of distance from the model edge as

$$\bar{S}_{excess}(y') = -\frac{\cos\alpha}{2w}\int_0^{\frac{2w}{\cos\alpha}}\left(\frac{\partial h}{\partial\theta}\right)\Big|_{y'} dx' \qquad (3.7)$$

with axes $x'$and y' as shown on Fig. 3.2. The line-averaged excess entropy transitions smoothly from the ferroelectric to paraelectric region and remains constant within each phase far from the phase boundary. The entropy jump $\Delta\bar{S}_{excess}$, the difference between the averaged entropy in the ferroelectric and paraelectric regions, increases with domain size as shown on the inset plot in Fig. 3.6. Note that while the total entropy depends on thermal expansion and specific heat, the entropy jump is not affected by these values for isothermal simulations. The trend in the entropy jump indicates that a larger domain structure would produce a larger electrocaloric effect, but the differences across the range of domain sizes investigated are small (less than 10%).

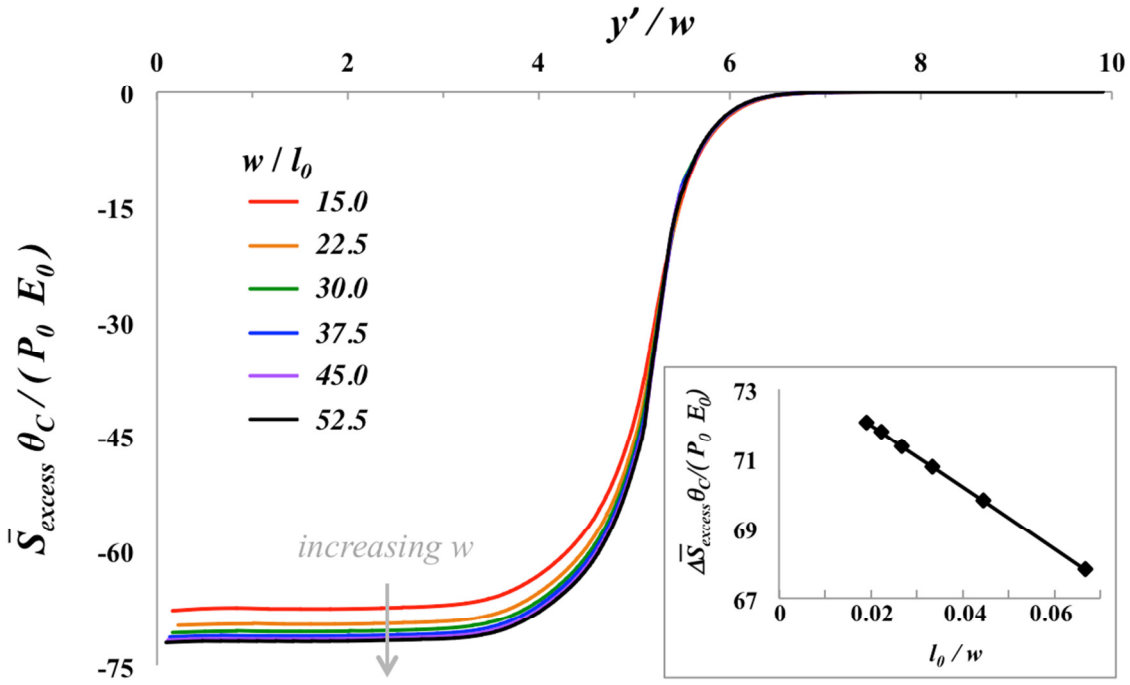

Figure 3.6: The line-averaged excess entropy as a function of distance y' from the bottom edge of the model for a variety of domain widths. The inset plot shows the entropy jump between the paraelectric and ferroelectric region is a linear function of the reciprocal of the domain width. The entropy for each domain width is computed at the phase coexistence temperature for the width, shown in Fig. 3.3.

The shapes and polarization magnitudes of the closure domains change with the domain width and are the cause of the size-dependent free energy of the phase boundary shown in Fig. 3.5. However, the entropy jump shown in the inset of Fig. 3.6 can be obtained solely from consideration of the load-free states of the ferroelectric laminate and the paraelectric phase far from the phase boundary. The transition region between these states is of course dependent on the details of the structures surrounding the phase boundary. Figure 3.7 shows the variation in the size and shape of the closure domains as the domain width is increased to twice and

three times the original size. The maximum magnitude of the *x*-polarization in the closure domain increases with the domain width, approaching the magnitude of the *y*-direction polarization in the laminate below. For larger domain sizes, the shape of the closure domains no longer looks like the triangular regions predicted in Fig. 3.2 and instead resemble needle domains [26], [40].

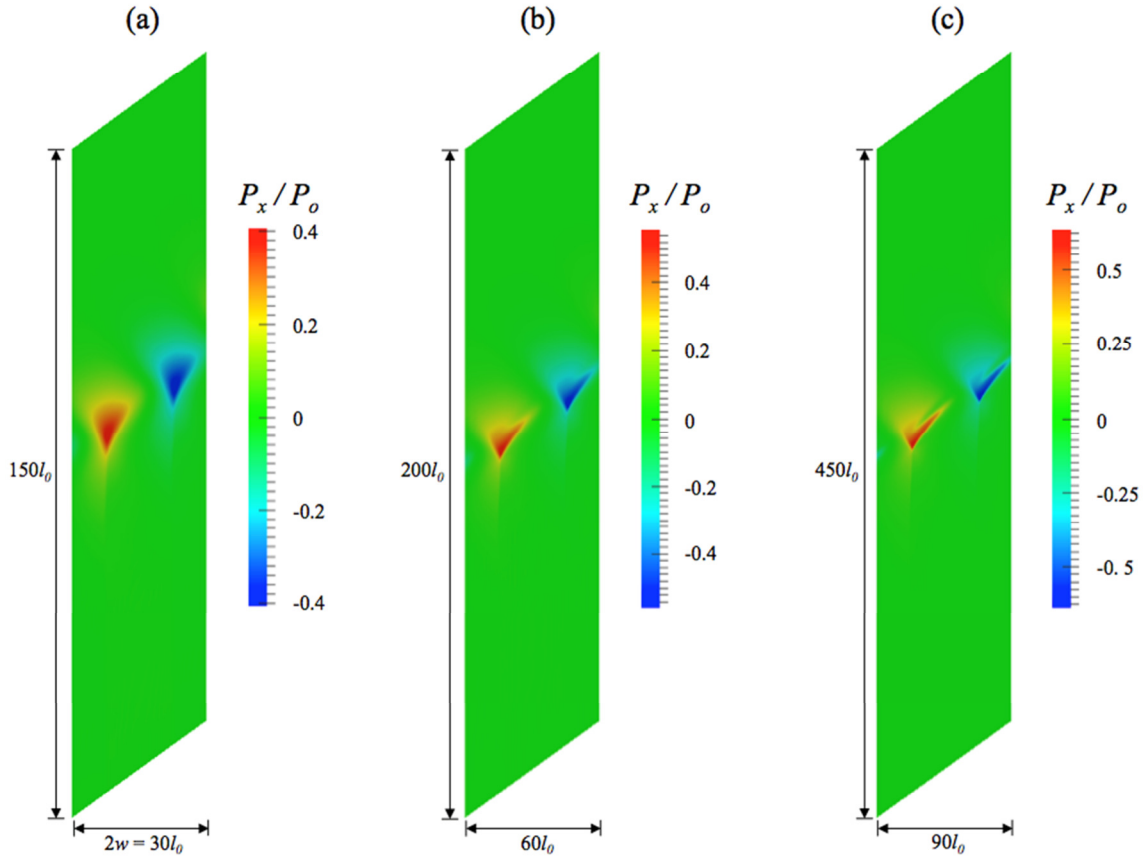

Figure 3.7: The normalized polarization in the *x*-direction of a 180° laminate ferroelectric-paraelectric phase boundary under generalized plane strain with $\varepsilon_{zz} = \varepsilon_{zz}^*$ for domain width (a) $w = 15l_0$, (b) $w = 30l_0$, and (c) $w = 45l_0$. The closure domain shape changes dramatically with the domain width and the peak *x*-direction polarization increases with domain width as follows: (a) 0.40 P_0 for domain width $15l_0$, (b) 0.56 P_0 for domain width $30l_0$, (c) 0.63 P_0 for domain width $45l_0$.

An alternative to the 180° laminate structure chosen for the FE-PE boundary shown in Fig. 3.2 is a 90° domain laminate structure [6]. As before, we choose to apply generalized plane strain conditions to reduce the dimensionality of the problem to two-dimensions. However, the 90° ferroelectric laminate is not mechanically compatible with the paraelectric phase along any plane for a two-dimensional model. Fig. 3.8 shows the in-plane stress-free configurations of the two phases. The strains in both the paraelectric phase and the 90° laminate are, on average, equibiaxial, but of different magnitudes. No rotation can make the two phases compatible. Therefore, the ferroelectric and paraelectric phases must be strained in the *x*-direction to create a compatible phase boundary. The strain is enforced by periodic boundary conditions on the left- and right-hand sides of the representative cell, requiring the average strain $\bar{\varepsilon}_{xx}$ along any line in the *x*-direction to be uniform in both the paraelectric and ferroelectric states throughout the entire model. Electrical compatibility is met in an averaged sense through the use of the laminate ferroelectric structure, but could also be met exactly through the use of a jagged non-planar boundary with boundary edges are parallel to the polarization vector in each domain of the laminate. The simulation results in Fig. 3.9 show the *x*- and *y*-polarization components as well as the magnitude of the polarization vector for a possible laterally *clamped* FE-PE boundary with a 90° ferroelectric laminate. The transition is more gradual than in the 180° FE-PE structure and no closure domains form between the two phases. The stresses in the *x*-direction, calculated

using Eq. 2.15, are $\sigma/\sigma_0 = 3.7$ and $\sigma/\sigma_0 = -1.9$ in the paraelectric and ferroelectric phases, respectively, where $\sigma_0 = E_0/(Q_{11}P_0) = 17.7$ MPa. Due to these high stresses, this phase boundary, while possible, is not physically likely.

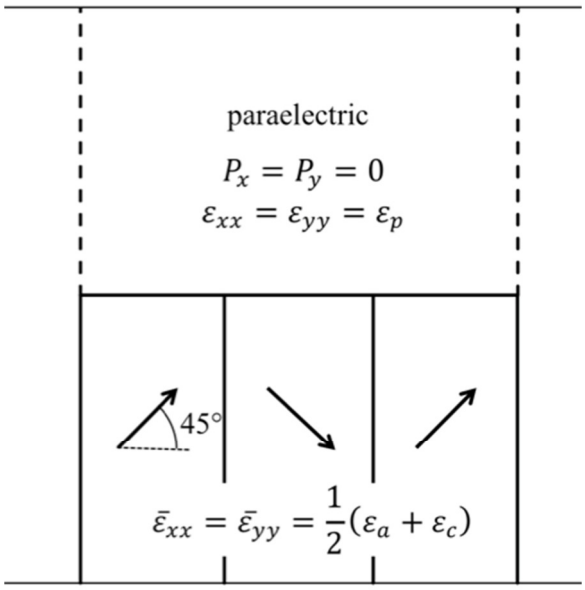

Figure 3.8: Ferroelectric-paraelectric phase boundary for a 90° rank-1 ferroelectric laminate. The arrows in the ferroelectric structure indicate the direction of the polarization vector. The mismatch in strains in the paraelectric and ferroelectric sections require an applied *x*-direction strain for a phase boundary to be mechanically compatible.

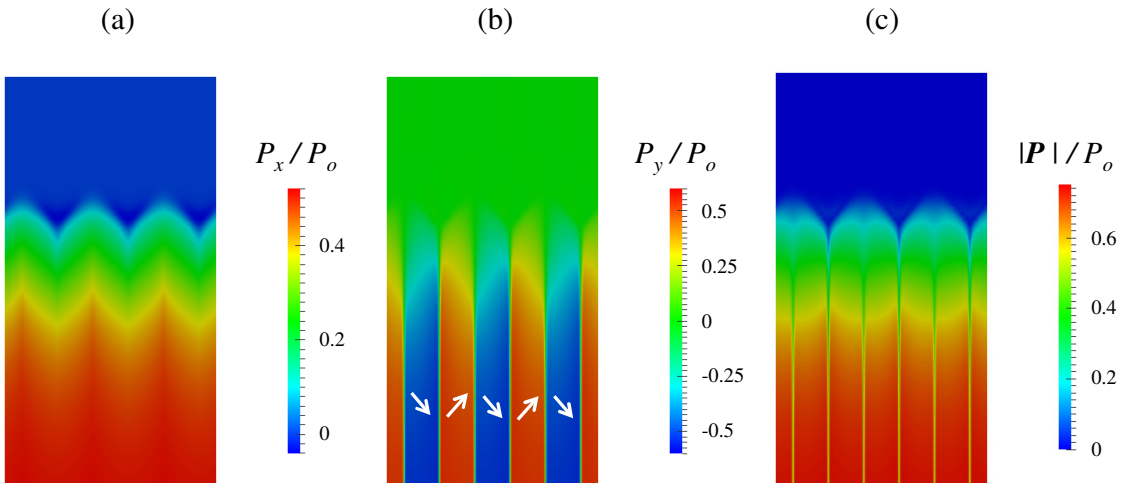

Figure 3.9: The (a) *x*- and (b) *y*-polarization for the simulation of a laterally clamped FE-PE phase boundary with a 90° ferroelectric laminate. The white arrows in (b) indicate the direction of the polarization vector. The total magnitude of the polarization (c) indicates a clear transition region, where the polarization shifts from the ferroelectric laminate to the zero polarization paraelectric state. This configuration is stressed to maintain mechanical compatibility between the paraelectric and ferroelectric phases. In contrast with Fig. 3.4, the transition is more gradual, and does not contain any closure domains.

Finally, while three-dimensional phase boundary structures are beyond the scope of this work, we briefly present the electromechanical compatibility conditions required for a three-dimensional planar phase boundary. We allow the ferroelectric phase to contain higher rank laminates in order to satisfy both average kinematic and charge compatibility with the paraelectric phase. From the crystallographic theory of martensite [38] it is known that low energy compatible phase boundaries exists when one of the principal strains for the ferroelectric laminate is equal to that of the paraelectric phase. The strains in the bulk paraelectric phase and the three rank-1 180° ferroelectric laminates are written as

$$\boldsymbol{\varepsilon}_p = \mathbf{0},\ \ \boldsymbol{\varepsilon}_f^x = \begin{bmatrix} \varepsilon_c & 0 & 0 \\ 0 & \varepsilon_a & 0 \\ 0 & 0 & \varepsilon_a \end{bmatrix},$$
$$\boldsymbol{\varepsilon}_f^y = \begin{bmatrix} \varepsilon_a & 0 & 0 \\ 0 & \varepsilon_c & 0 \\ 0 & 0 & \varepsilon_a \end{bmatrix},\ \ \boldsymbol{\varepsilon}_f^z = \begin{bmatrix} \varepsilon_a & 0 & 0 \\ 0 & \varepsilon_a & 0 \\ 0 & 0 & \varepsilon_c \end{bmatrix} \tag{3.8}$$

where the *p* and *f* subscripts indicate paraelectric and ferroelectric, and the *x*, *y* and *z* superscript indicates the direction of the tetragonal axis of the ferroelectric. The strain components ε_c and ε_a are the spontaneous strains associated with the ferroelectric laminate at a specified domain width. Assuming now, as an example, that we allow only *x*- and *y*-aligned laminates and assign each a volume fraction of f_x and f_y, respectively, we can find a structure with an average zero strain in the *x*-direction. Figure 3.10 presents a possible rank-2 laminate that meets this criterion. The ferroelectric portion of the material contains a combination of *x*- and *y*-aligned rank-1 180° ferroelectric laminates, at a volume fraction of $f_x = -\varepsilon_a/(\varepsilon_c - \varepsilon_a)$ and $f_y = \varepsilon_c/(\varepsilon_c - \varepsilon_a)$ and is invariant in the *z*-direction far from the boundary. The FE-PE phase boundary plane is parallel to the *x*-axis at and angle α with respect to the *x*-*z* plane. To find the angle of the boundary shown in Fig. 3.10, we consider that the displacement of any point on the boundary is equal on the paraelectric and ferroelectric side of the boundary. Given a simplified isochoric case where $\varepsilon_a = -\varepsilon_c/2$, this specific configuration would have volume fractions $f_x = 1/3$ and $f_y = 2/3$ and angle $\alpha = 45°$. In addition to the possible planar phase boundaries

outlined here, there are an infinite number of other non-planar three-dimensional configurations for the FE-PE boundary as well, but these are not amenable to unit cell calculations due to the lack of periodicity in the structure or the large unit cells that would be needed to study such structures. In any case, these planar domain/phase structures are fundamental to perovskite materials that exhibit first order phase changes near a Curie temperature, including ferroelectric and ferromagnetic materials [41] as well. In fact, similar modeling techniques can be used to model the magnetocaloric effect in NiMnGa [42].

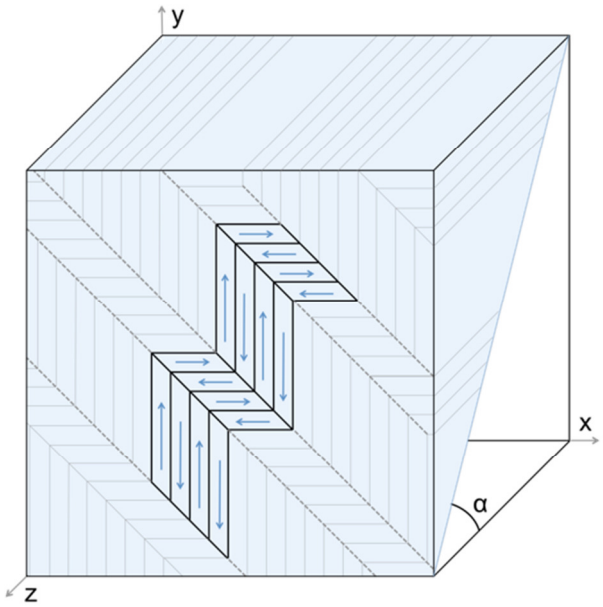

Figure 3.10: A possible three-dimensional structure for the FE-PE boundary. The shaded area is ferroelectric, while the white area is paraelectric. The plane where the two regions meet, the FE-PE phase boundary, is parallel to the *x*-axis and is inclined at an angle α with respect to the *x*-*z* plane. The ferroelectric portion is composed of a rank-2 laminate invariant in the *z*-direction. For an isochoric transformation, the *x*-aligned and *y*-aligned ferroelectric laminates are 1/3 and 2/3 of the ferroelectric volume, respectively, and the angle α is 45°.

3.3 DISCUSSION OF STABLE FE-PE PHASE BOUNDARY RESULTS

The excess free energy calculations suggest that there is a finite excess free energy for large domain sizes. The excess free energy per area shown in Fig. 3.5 is the following linear function of the reciprocal of the domain width

$$\frac{\psi_{excess}}{P_0 E_0} = -0.0662 \left(\frac{l_0}{w}\right) + 0.0278 \qquad (3.13)$$

where 0.0278 is the asymptotic value of the normalized excess energy as the domain width tends to infinity. The entropy jump across the phase boundary shown in Fig. 3.6, a measure of the electrocaloric effect in the material, is also a similar function of the domain width, and is given as,

$$\Delta\bar{S}_P \left(\frac{\theta_C}{P_0 E_0}\right) = -88.6 \left(\frac{l_0}{w}\right) + 73.7 \qquad (3.14)$$

where 73.7 is the asymptotic value of the normalized jump in entropy. From Eq. 2.29 (numerical values give in Appendix A), we can calculate the theoretical maximum entropy jump across the phase boundary as a function of the maximum polarization to be

$$\Delta\bar{S}_{max} \left(\frac{\theta_C}{P_0 E_0}\right) = 92.7 \left(\frac{P_{max}}{P_0}\right)^2. \qquad (3.15)$$

Using the asymptotic value of the maximum polarization for the generalized plane strain ferroelectric laminate (see Fig. 3.3), the maximum entropy jump possible for

this scenario is 73.6 P_0E_0/θ_C, agreeing (to within 0.2%) with the asymptotic value of the entropy jump found from the simulations. This value is 79% of the absolute achievable maximum for an *unconstrained* bulk monodomain, where $P_{max} = P_0$. This reinforces the understanding that unconstrained material transformations maximize the electrocaloric effect.

These calculations illustrate two competing factors associated with the electrocaloric effect. First, a fine domain structure on the ferroelectric side of the phase boundary reduces the phase boundary energy in comparison to a coarser domain structure. This reduction in phase boundary energy is generally associated with a reduced hysteresis upon cycling, i.e. as the phase boundary moves back and forth through the material. A low hysteresis is critical for many electrocaloric applications. On the other hand, the surface tension associated with the domain walls can lead to small decreases in the polarization magnitudes that can be achieved in the unloaded ferroelectric laminate structure. This reduction in the polarization then also results in a reduction in the entropy jump across the phase boundary, and an associated reduction in the electrocaloric effect. We do note that both the phase boundary energy changes and entropy jump changes are relatively small, ~10%, across the domain widths that have been studied in this work.

3.4 PHASE BOUNDARY MOTION

As illustrated in Figure 3.1(b), the motion of the phase boundary through the material can be achieved through entropy/heat input control of the system. To

demonstrate this motion, we turn to the time-dependent thermo-electro-mechanical weak form from Eq. 2.34. The implementation of this model with nonlinear finite element requires evolution in time, and the addition of another degree of freedom, temperature (details on the finite element implementation can be found in Chapter 2). Using the results from the stable FE-PE boundary shown in Fig 3.5 as initial conditions, we simulate the motion of the phase boundary through the material. Since the phase boundary will no longer be centered at the midpoint of the model, the boundary conditions must change to accommodate this motion. As before, periodic boundary conditions are applied on the dashed lines (side A and B) in Fig. 3.2. The potential and polarization boundary conditions remain unchanged. However, since the average strains in the ferroelectric phase, ε_a and ε_c are dependent on temperature, and temperature is no longer fixed, the displacement boundary conditions are modified to allow for periodicity while maintaining in-plane stress-free conditions. The new periodic boundary conditions are

$$\begin{aligned} \phi^B &= \phi^A \\ P_x^B &= P_x^A \\ P_y^B &= P_y^A \\ u_x^B &= u_x^A + u_x^C \\ u_y^B &= u_y^A + u_y^C \end{aligned} \tag{3.9}$$

where point C is the lower right corner of the model, as shown in the figure. The forces at point C are set to $F_x = F_y = 0$ to achieve the average stress-free condition in the model. Displacement boundary conditions along the entire top and bottom edge of the model are no longer necessary to control the total entropy of the system. The temperature-dependent finite element implementation allows for entropy to be directly controlled by the addition/removal of heat through Neumann boundary conditions on the temperature degree of freedom. Therefore, the boundary conditions on the top paraelectric (P) and bottom ferroelectric (F) edge of the structure are now

$$\begin{aligned} \phi^F &= 0 \\ u_x^F &= u_x^B\left(\frac{x^F}{2w}\right) \\ u_y^F &= u_x^B\left(\frac{y^F}{2w}\right) \end{aligned} \qquad (3.10)$$

where x^F and y^F and the coordinates of the ferroelectric bottom edge nodes. The two displacement boundary conditions in Eq. 3.10 are used simply to keep the bottom edge straight. Without this constraint, the displacements would kink at the domain walls, which would be inconsistent with our desire to mimics semi-infinite phases on either side of the boundary. This displacement constraint is not necessary for the paraelectric edge, since that edge will naturally remain straight without constraints. In fact, no displacement boundary conditions are necessary to stabilize

the top paraelectric edge, but Neumann boundary conditions are again applied to enforce zero net charge along the top edge. Finally, to enforce entropy/heat control, the temperature is required to be uniform throughout and heat is applied or removed at a constant rate. Using multipoint constraints, we allow the system to distribute the heat as needed throughout the whole structure in order to maintain isothermal conditions. To reiterate, in this simulation, isothermal does not imply that the temperature is being set, only that it is to be uniform throughout the material. In fact, we expect that the temperature will change slightly with the application and removal of heat.

Figure 3.11 shows deformed shape of the phase boundary simulation as the boundary moves through the material. Due to the limitations in the refinement of the mesh, the wall is not moved through all the way to the edges of the model. The entropy is increased linearly with time, i.e. heat is supplied at a constant rate, to reduce the proportion of the ferroelectric phase (move the boundary up) and then decreased linearly with time to reduce the proportion of paraelectric phase (move the boundary down) to return to the original state. Figure 3.12 shows the entropy as a function of the temperature for the phase boundary motion. Note that in the ideal case shown by the solid line in Fig. 3.1(b), where no energy is dissipated, the boundary moves through at a single unique phase coexistence temperature. However, due to dissipative forces and coupling, the temperature does exhibit a slight change as the boundary moves through the material. The temperature range

for the transition shown is $4 \times 10^{-5}\theta_C$, or about $0.016K$, and is therefore *quite narrow*.

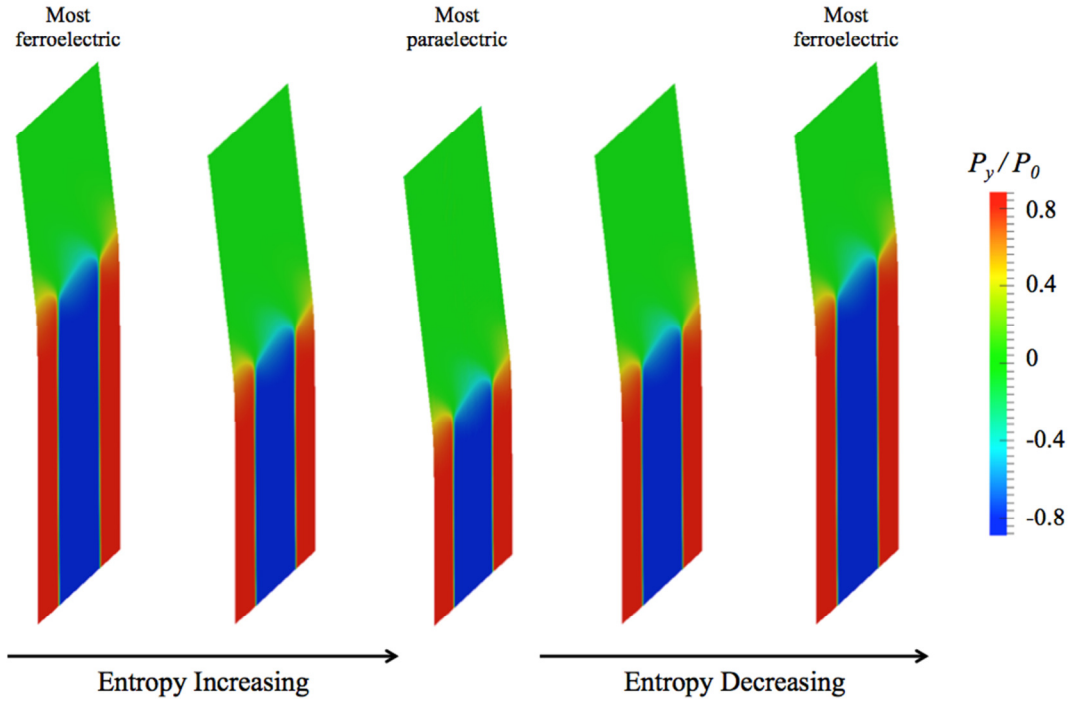

Figure 3.11: The deformed shape and y-polarization for a 180° rank-1 laminate FE-PE phase boundary as it moves though the material under entropy/heat input control. The entropy is increased linearly to increase to move the phase boundary down and then decreased linearly to move the phase boundary back up. The shape of the phase boundary remains the same as the front propagates through the material.

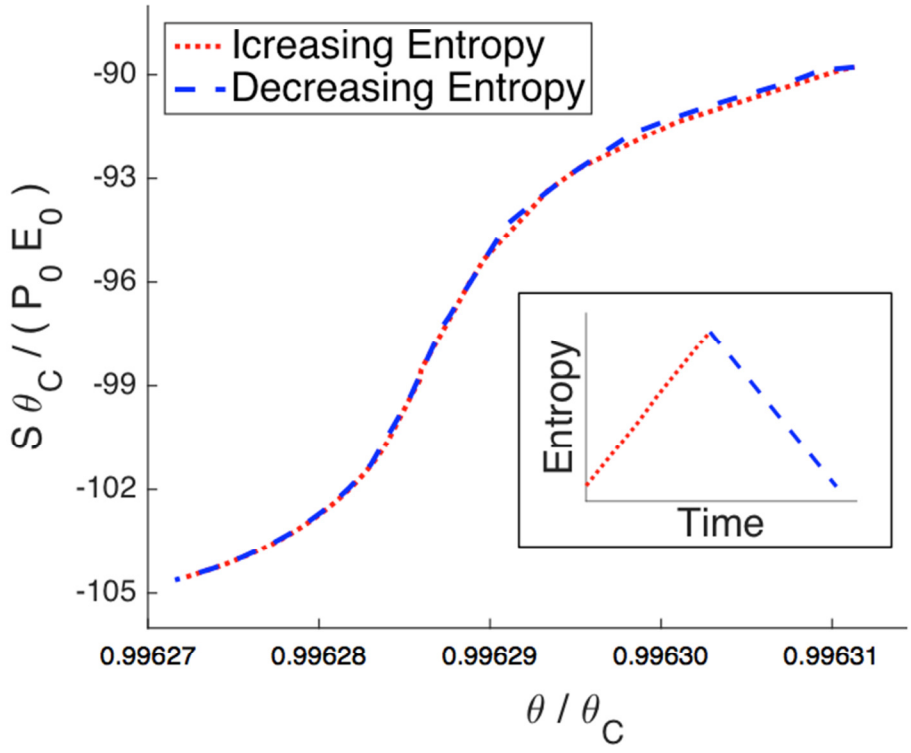

Figure 3.12: The relationship between entropy and temperature as the FE-PE phase boundary propagates through the material with the application and removal of heat. As indicated in the inset, the entropy increases and decreases linearly with time due to constant heat input over time. The overall temperature range of the transition shown is $4 \times 10^{-5}\theta_C$, or $0.016K$.

For an explanation of the shape seen in the temperature vs. entropy relationship in Figure 3.12, we look to the coupled heat conduction equation derived in Chapter 2 (Eq. 2.27). Removing all terms that evaluate to zero, ignoring the thermal expansion (which is negligible over such a small temperature range), and setting $\beta_{ij} = \beta\delta_{ij}$ the energy balance reduces to

$$\left(\kappa_{ij}\theta_{,j}\right)_{,i} + \theta\left(\frac{\partial^2 h}{\partial\theta\partial P_i}\dot{P}_i + \frac{\partial^2 h}{\partial^2\theta}\dot{\theta}\right) + \beta\dot{P}_i\dot{P}_i = 0\,. \qquad (3.11)$$

Since the simulation is isothermal, there are no gradients in temperature, so the first term in Eq. 3.11 is zero. Also, assuming that the phase boundary moves through at a constant rate (which is verified by the simulation), the $\dot{P}_i$ will be constant regardless of the location of the phase boundary. Expanding the second derivatives of the electrical enthalpy using Eq. A.1 form the Appendix, the heat conduction equation now becomes

$$2\theta\alpha_1\left(P_x + P_y + P_z\right)A - C_p\dot{\theta} + \beta A^2 = 0 \qquad (3.12)$$

where A is the constant rate of change of the polarization and α_1 and C_p are constant material properties (numerical values given in the Appendix A). If the LGD landscape for the free energy did not have coupling between the polarization and temperature, then the first term in Eq. 3.12 would be absent from the expression, so the relationship could be integrated to show a linear dependence between the temperature and time, and therefore a linear dependence between temperature and entropy (see inset in Fig. 3.12). In the extreme case, where $\beta = 0$ as well, there is no dissipation associated with the boundary motion, the temperature is constant in time, and thus the temperature is constant for any entropy values as the phase boundary moves through the material (the ideal case). The presence of the first term causes the temperature-entropy relationship to deviate from a linear shape,

and instead gives rise to the shape show in the simulation results in Fig. 3.12. While the temperature does not remain perfectly constant, this simulation verifies that the phase boundary can be moved, reversibly, through the material using entropy/heat control. The simulation was repeated with a different polarization mobility values to test whether the results are highly sensitive to this term, and no difference in the shape of the curve was noted. Therefore, we can confidently conclude that the coupling between the polarization and temperature is the primary contribution to the nonconstant temperature nature of the phase boundary motion.

3.5 CONCLUSION

The ferroelectric-paraelectric phase boundary is the fundamental defect that drives the electrocaloric effect. This chapter uses a phase-field approach and the finite element method to model the structure of the phase boundary for non-conducting barium titanate under generalized plane strain conditions. To our knowledge, the structure of such boundaries has not been directly observed. A mechanically and electrically compatible angled phase boundary was found for a representative unit cell with the ferroelectric phase arranged in a rank-1 laminate with a 180° domain structure. The phase coexistence temperature for the phase boundary approaches the Curie temperature as the domain width increases and the relative energy contribution of the domain walls diminishes. The maximum polarization in the ferroelectric laminate follows the same trend, approaching an asymptote as the domain width increases. The asymptotic value of the maximum

polarization is less than the spontaneous polarization of the bulk material, P_0, since the model is constrained in the *z*-direction. We show that the excess free energy per unit area of the model increases with domain width, indicating that the energy of the 180° FE-PE phase boundary is domain size-dependent. The closure domains that form between the two phases to resolve local electrical incompatibilities are responsible for the size-dependence of the free energy. The closure domain shape changes with domain size, shifting from a roughly triangular to a more needle-shaped domain as the domain width increases. This suggests that the relative volume of the transition zone decreases with increasing domain width and explains the asymptotic approach to a finite excess phase boundary energy for large domain widths. We also simulated the boundary motion of the 180° rank-1 laminate FE-PE phase boundary by entropy/heat input control to demonstrate that such boundaries are stable under specific thermodynamic conditions.

Aside from the highlighted case of the 180° rank-1 laminate FE-PE phase boundary, another simple planar configuration with a rank-1 90° ferroelectric laminate was computed. However, due to the mechanical constraints required to enforce compatibility of the strains between the ferroelectric and paraelectric phases, the configuration is stressed, making it unlikely to form naturally. In order to find unloaded FE-PE phase boundaries in three dimensions, rank-2 ferroelectric laminate structures can be used, with the phase boundary angle dictated by the

crystallographic theory of martensite. Further explorations of such three-dimensional boundaries are left for future work.

Chapter 4: Phase-field model of an electrocaloric cooling device

Much of the excitement with the discovery of the giant electrocaloric effect (ECE) stemmed from its possible application to solid-state cooling devices. Conventional vapor compression cycle refrigerators are bulky and cannot be scaled to chip level. Moreover, conventional refrigeration is not environmentally friendly, as most refrigerants are potent greenhouse gases. Electrocaloric (EC) devices, on the other hand, are compact, scalable, highly efficient and environmentally friendly. In 2010, Kar-Narayan and Mathur serendipitously observed the ECE in commercial multilayer capacitors (MLCs) [43], suggesting that such a device could be used at chip scale for EC cooling. In this chapter, phase-field modeling techniques are used to model the thermodynamic cooling cycle in an MLC electrocaloric device. We discuss the selection of geometry and boundary conditions, as well as the limitations of the model. Finally, the difference between the modeled cycle and the cycle for an ideal monodomain under plane strain are discussed, bringing to light some of the device inefficiencies that should be considered in the design process.

4.1 Device geometry and boundary conditions

Since the discovery of the ECE in multilayer capacitors [43], EC cooling device design has centered around the MLC configuration: alternating layers of ferroelectric material and electrodes. Figure 4.1 shows the electrode, terminal and

EC/ferroelectric material configuration for a typical cooling device. The interdigitated electrode array is filled with EC material and each electrode is connected to one of two terminals. Generally, one terminal will be grounded, while the other has an applied potential, creating an array of alternating electric fields between each set of electrodes. The structure is ideal for EC cooling for several key reasons, as explained by Kar-Narayan, *et al.* in Electrocaloric Materials [19]. First and foremost, the multilayer capacitor configuration can exploit the giant ECE found in thin film materials. The EC material is essentially deposited as a thin film in between the electrodes, allowing for large electric fields with relatively small voltages and no risk of electrical breakdown or arcing. The configuration also allows for efficient heat transfer due to the large contact area between the EC material and the electrode. Finally, the metal electrodes are excellent thermal conductors, helping transfer the thermal load in and out of the EC material [19].

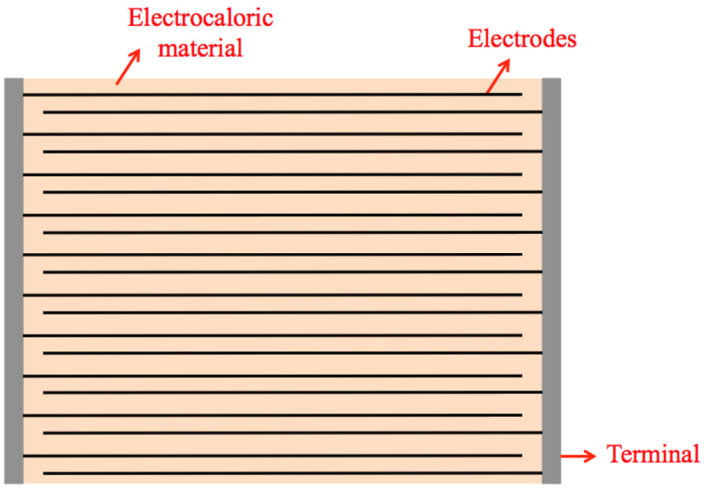

Figure 4.1: Schematic of the interdigitated electrode MLC electrocaloric cooling device

The integration of multilayer EC cooling devices into actual refrigeration technology presents another challenge. Since the terminals/electrodes are used as the thermal conductors, they must be placed in contact with the heat sinks or heat sources. Epstein and Malloy suggested heat switches based on thin film liquid crystals [20]. The liquid crystals have highly anisotropic thermal conductivities and the alignment of the molecular directors can be controlled by an electric field. The switches are opened and closed by the application of a parallel or perpendicular electric field, changing the film properties between thermally insulating and thermally conductive, respectively. The advantages of using a heat switch method is that there are no moving part, and the switch time could be quite fast, dependent only on the viscosity of the liquid suspension. However, the heat switches would be continuously in contact with the EC cooling device, thereby increasing the likelihood of heat leakage through closed switches. Micromechanical systems (MEMS) could also be used in small-scale devices to control the heat flow. For example, Ju designed an interdigitated device suspended by silicon mechanical flexures which can be actuated by a low power MEMs device [21]. The flexures move the interdigitated device up and down to alternately bring it into contact with the heat sink and source. The adiabatic stages of the cooling cycle are met by suspending the device out of contact with either side. This design would minimize heat loss, but does depend on moving parts, thereby making reliability and speed an issue. For both configurations from the literature described above, each interdigitated electrode

and terminal set (right or left) only serves as the thermal conductor for either the heat sink or the heat source, not both. We therefore make this assumption for our calculations. We also assume that any part of the device *not* in contact with the source or sink at a given point in time is a perfectly thermally insulated boundary.

The schematic shown in Fig. 4.2(a) shows the overall geometry chosen for the phase-field modeling of the electrocaloric cooling device. The right and left electrodes, indicated in red and blue, respectively, extend 95% of the length of the entire structure into the grey EC material. The electrodes and terminals have a thickness of l_0 and the electrode tips are semicircular. The left terminal is grounded, while the right has a specified applied potential that varies depending on the step in the EC cooling cycle, shown in Fig. 4.2(b). During first leg of the cycle, the potential is increased from $\phi^R = 0$ to $\phi^R = \phi_{max}$. The maximum potential is chosen such that it produces an average electric field of magnitude $|E_y| = 10\, E_o$ between each set of electrodes. The maximum applied electric field is of the same order as those found in literature and should be well beyond necessary electric field to induce a phase transition. The electric field is kept constant during the second leg, then reduced gradually back to zero on the third leg, and kept at zero for the fourth leg. The temperature boundary conditions at the electrodes also depend on the leg of the cooling cycle. The device is under perfect adiabatic conditions for the first and third leg of the cycle. While drawn as isentropic in Fig. 4.2(b), the adiabatic legs are only isentropic in ideal energy conserving conditions. On the second leg of the cycle, the

hot side is placed in contact with the heat sink, so temperature is specified along the vertical right edge of the model. Similarly, on the fourth leg, the cool side is placed in contact with the source, so temperature is specified along the vertical left edge of the model. The copper electrodes are modeled as isotropic linear elastic solids with thermal conductivity k^{Cu}. The electrical properties of the electrodes are not modeled, as copper is assumed to be a perfect electrical conductor. The material properties of copper used in this work can be found in Appendix A.

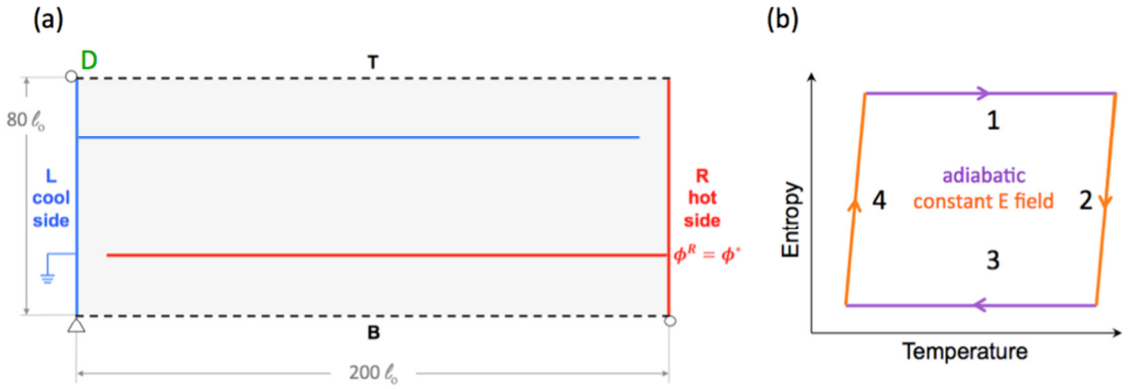

Figure 4.2: (a) Schematic of the geometry chosen for the simulation of a representative unit cell of the electrocaloric cooling device. The left electrode is grounded while the right is at some applied potential. The dashed lines on the top (T) and bottom (B) are periodic boundaries. (b) The EC cooling device is subjected to the thermodynamic refrigeration cycle with two adiabatic legs and two constant electric field legs. The hot side of the device is placed in contact with the heat sink during the second leg of the cycle and the cool side is placed in contact with the source on the last leg on the cycle

The interface between the electrodes/terminals and the EC material are modeled as perfectly bonded. Previous iterations of this work thought to exclude the electrode from the model, simply assuming a constant height inclusion that offers no

mechanical resistance in place of the electrode, and either fixed or free conditions at terminal edges. This assumption required applying the temperature boundary conditions along the full length of the edges of the inclusion. However, as seen in the results of the simulation, this was a poor assumption. First, the temperature does not instantaneously travel the length of the electrode, so the thermal conductivity of the electrode must be considered. Also, the copper electrode does provide some mechanical resistance to the shape change that occurs in the EC material as it goes through the phase transformation. The interfacial strains from the electrode/EC interface dampen the transformation, and therefore must be considered for better simulation accuracy. The small thickness of the electrodes is chosen so as to contribute minimally to the overall cycle.

The top and bottom of the model, shown by the black dashed lines labeled T and B in Fig. 4.2(a), are periodic boundaries with boundary conditions throughout the whole cooling cycle given by

$$\begin{aligned} u_x^T &= u_x^B \\ u_y^T &= u_y^B + u_y^D \\ \phi^T &= \phi^B \\ P_x^T &= P_x^B \\ P_y^T &= P_y^B \\ \theta^T &= \theta^B \,, \end{aligned} \tag{4.1}$$

where point D is the top left corner of the model, as indicated in Fig. 4.2(a). The periodic displacement boundary conditions dictate that the device is free to deform but has an average in-plane stress of zero. Plane strain conditions are assumed out-of-plane. The size of the structure, $80l_0 \times 200l_0$, is chosen such that well-defined boundaries can form at the ends of each electrode, but the EC material in the center of the model is free from edge effects, and thus transforms uniformly.

4.2 SIMULATION OF ELECTROCALORIC COOLING CYCLE

For any meaningful results to be understood from the simulation of the EC device cooling cycle, a baseline must be determined to use for comparison. For this, we turn to the free energy function (see Appendix A) and look at two different scenarios, a bulk stress-free $BaTiO_3$ and plane strain $BaTiO_3$ with in-plane stresses equal to zero. Considering a range of electric fields and a range of temperatures near θ_C, we solve for the entropy as a function of the temperature. The entropy is computed for the lowest energy monodomain for a particular temperature, disregarding hysteresis and direction of temperature change. Figure 4.3(a)-(b) shows the entropy vs. temperature diagrams for the bulk and plane strain monodomains for electric fields from $E = 0$ to $E = 10E_0$. As expected, a large entropy jump is seen at the transition temperature. The discontinuity in the entropy is a classic indication of a first order phase transition. The plane strain constraint suppresses the transition temperature from θ_C to $0.988\theta_C$. The general entropy trend at higher electric fields is very similar between the two cases. While a phase

transition is still evident for an electric field of magnitude E_0, the phase transition at the electric fields $5E_0$ and $10E_0$ are annihilated: there is *no* temperature at which the paraelectric phase is energetically favorable at such high fields.

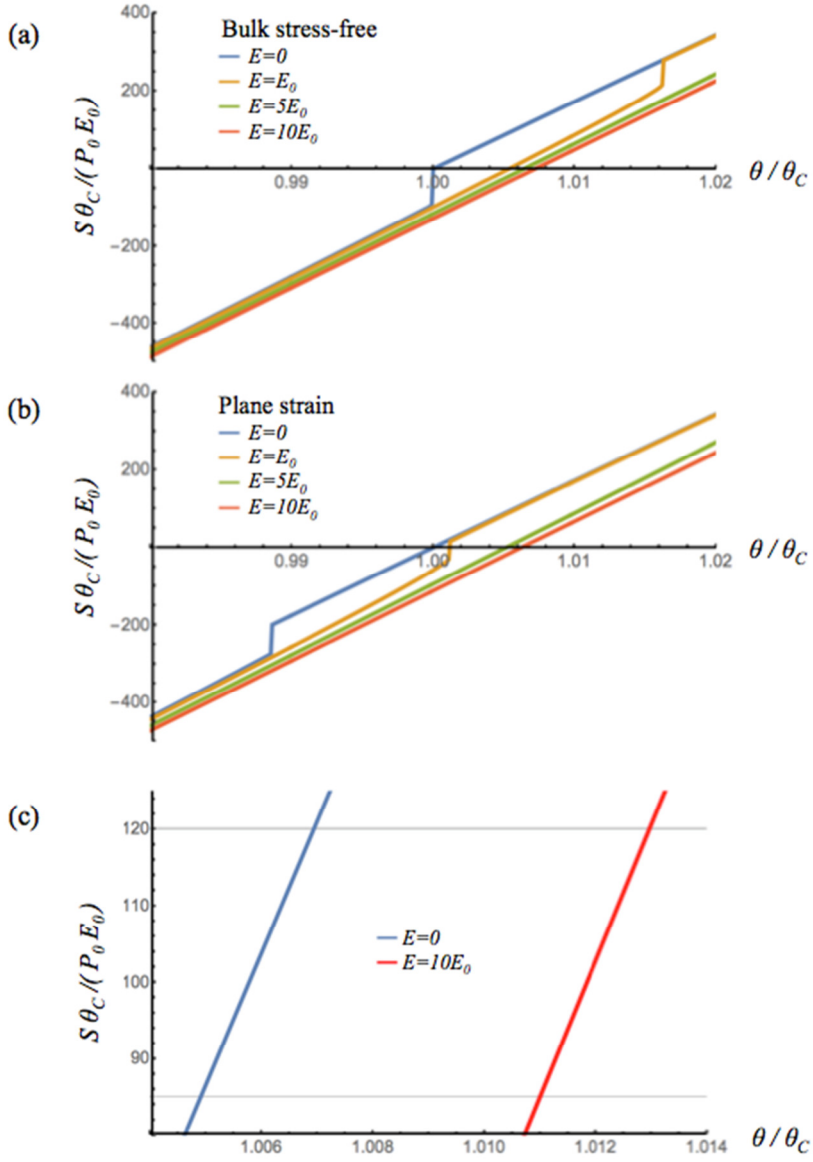

Figure 4.3: The analytically computed temperature vs. entropy diagram for (a) a bulk stress-free monodomain and a (b) plane strain, in-plane stress-free monodomain. (c) The ideal plane strain thermodynamic cooling cycle is developed with two constant field branches with isentropic legs between them.

We choose the plane strain solution as a baseline for comparison for the EC cooling device. The constant electric field lines for $E = 0$ and $E = 10E_0$ provide two of the four legs of the thermodynamic cycle for the ideal plane strain monodomain. The other two legs are simply isentropic lines connecting the two constant field lines, as shown in Fig. 4.3(c).

The simulation of the EC cooling device is performed with a mesh of approximately 9×10^4 bilinear quadrilateral elements. The mesh is selectively refined to a length and width of $l_0/4$ or smaller in areas where phase/domain boundary structures are present. Initially, the material is in the pure paraelectric phase with zero polarization throughout, and no strain mismatch exists between the EC material and electrode/terminal interfaces. The starting temperature is isothermal with temperature $\theta = 1.00693\ \theta_0$. The choice of starting temperature in motived by the observations of Moya, *et al.* who note that EC temperature changes near the transition temperature are only reversible above the *transition finish temperature* for the ferroelectric to paraelectric transition [44]. Therefore, we choose a temperature just slightly above θ_C, definitively higher than the transition finish temperature for heating from ferroelectric to paraelectric, as calculated analytically from the free energy function. The simulation is performed using the governing equations and time-dependent finite element implementation discussed in detail in Chapter 2.

Before continuing to the results of the simulations, we briefly discuss the two time scales associated with the fully thermo-electro-mechanically coupled ferroelectric model: the polarization time scale, indicating the time scale with which the domain/phase boundaries move through the material, and the thermal time scale, related to the speed of thermal conductivity. The two times scales can be written in terms of the problem parameters (see Appendix B) as

$$t_P \propto \beta \frac{P_0}{E_0} \tag{4.2}$$

and

$$t_\theta \propto \frac{P_0 E_0 l_0^2}{k\theta_C} \tag{4.3}$$

where one time scale is proportional to the value of β, the polarization viscosity, and the other inversely proportional to k, the thermal diffusivity. The two time scales can be modified relative to one another and are, as a general rule, not the same. The polarization time scale is used as a computational tool for the evolution of the phase/domain structure within the model. The exact value of β is chosen to allow for computational stability, but should not impact the steady-state solution if chosen wisely, i.e. small such that the domain/phase structure equilibrates with the prevailing temperature field. The temperature time scale, on the other hand, is directly tied to the physical properties of the material. Since k is an easily

quantifiable material property (see Appendix A), the time scale associated with temperature diffusion is the relevant time scale used to characterize the evolution of the fields during the cycle.

In the simulation of the refrigeration cycle of an EC cooling device, Fig 4.4 shows the evolution of the polarization as the material traverses the first adiabatic leg of the cycle. Applying a nonzero potential to the right electrode/terminal creates a nonzero electric field in the EC material. The potential is increased in regular discrete increments and the structure evolves after each increase. Initially, the material immediately between the electrodes transforms, while the material between the terminals and the electrode tip forms diffuse closure domains. Once the average electric field is sufficiently large, the majority of the EC material transforms to align with the electric fields, with much sharper closure domains forming at the electrode tip to accommodate local electrical incompatibilities. The transition between incomplete and full transformation occurs between $5E_0$ and $6E_0$.

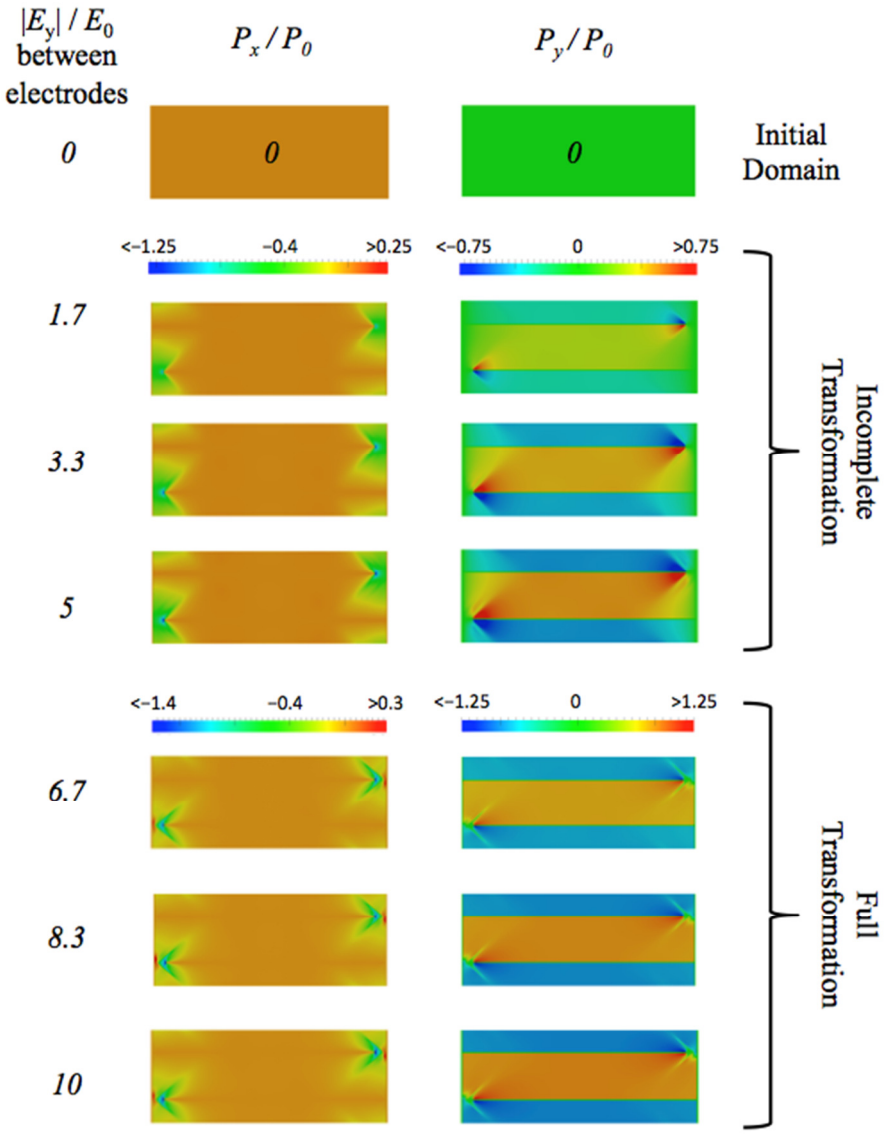

Figure 4.4: The evolution of the polarization domain structure in the first leg of the thermodynamic cooling cycle of the electrocaloric cooling device. As the electric field between the electrodes increases, the material transforms from uniform paraelectric to the fully transformed ferroelectric domain structure. The transition between incomplete transformation and full transformation occurs between $5E_0$ and $6E_0$.

In the second leg of the thermodynamic cycle, the entropy decreases as the device is placed in contact with the heat sink. The heat sink is at a temperature

$\theta = 1.011\,\theta_C$. The temperature chosen must be below the average temperature after the completion of the first leg, since heat will only flow from hot to cold. The device is cooled until it reaches essentially isothermal conditions. This is not necessary for the operation of such a device, but is a choice we make in our calculations in order to better predict the *final* domain structure that would exists once the device is cooled, rather than a metastable intermediate state. Moreover, the ideal plane strain case to which we care comparing our results assumes uniform temperature in the monodomain at the completion of every leg of the cycle. Assuming isothermal conditions at the end of the constant field leg places an additional restriction on the heat sink temperature: the smaller the difference in temperature between the average temperature after completion of the first leg and the heat sink, the greater the temperature change that can be driven by the cycle. Note that, the temperature change driven by the cycle is defined as the difference between the temperature of the source and the sink. This consideration is unique to the chosen constant field cooling cycle, and can be avoided by using a Carnot-like cycle with isothermal steps in place of the constant electric field steps (see discussion of the cooling cycle and Fig. 1.4 in Chapter 1).

Figure 4.5 shows the evolution of the temperature as the right side of the device is placed in contact with the heat sink. The temperature is initially nonuniform, with the highest temperatures around the electrodes, especially the electrode tips. This is due to the fact that the material is not given time to evolve into

an isothermal state after the application of the electric field (this is assumed to be the "fast" step). Given more time, the temperature would eventually become homogeneous, but the average temperature would not change during that process (assuming the heat capacity is a constant). As heat leaves through the heat sink, the temperature becomes cooler on the heat sink side. Notice that kinking in the temperature front is evident from the presence of the highly thermally conductive electrodes. The electrode attached to the heat sink terminal moves the front forward, while the electrode attached to the insulated terminal slows the progression of the front. However, the electrodes are not at a uniform temperature, confirming the necessity of modeling the electrodes with a finite thermal conductivity despite the fact that the thermal conductivity of copper is more than two orders of magnitude larger than that of $BaTiO_3$ (see Appendix A). Heat is withdrawn from the device until the temperature is essentially uniform, with the left side predictably taking the longest time to cool to the heat sink temperature. Throughout this heat removal step, the applied potential remains at the maximum value (maintaining a constant average applied electric field between the electrodes), and the domain structure within the device does not change significantly. The sharpness of the stress distributions within the device soften as the material approaches an isothermal state.

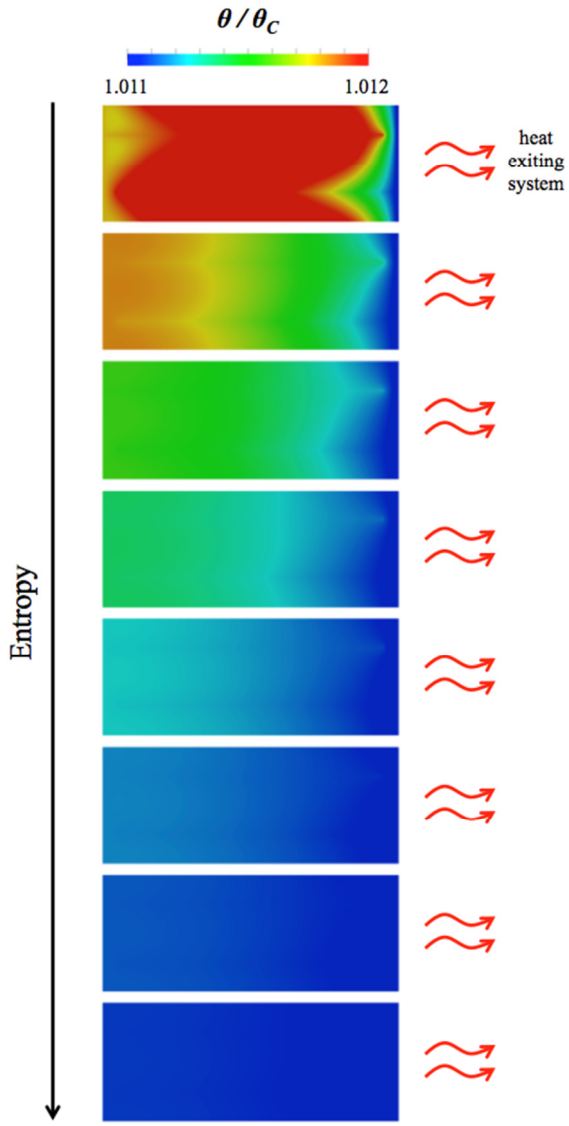

Figure 4.5: The time evolution (with uniform time steps) of the temperature distribution as the EC cooling device is brought into contact with the heat sink of temperature $\theta = 1.011\ \theta_C$ in the second leg of the thermodynamics cooling cycle. As heat exits the system through the right side, the entropy decreases and the device cools. Kinking in the cooling front is caused by the presence of highly thermally conductive electrodes. The cooling is complete when the material is of a uniform temperature.

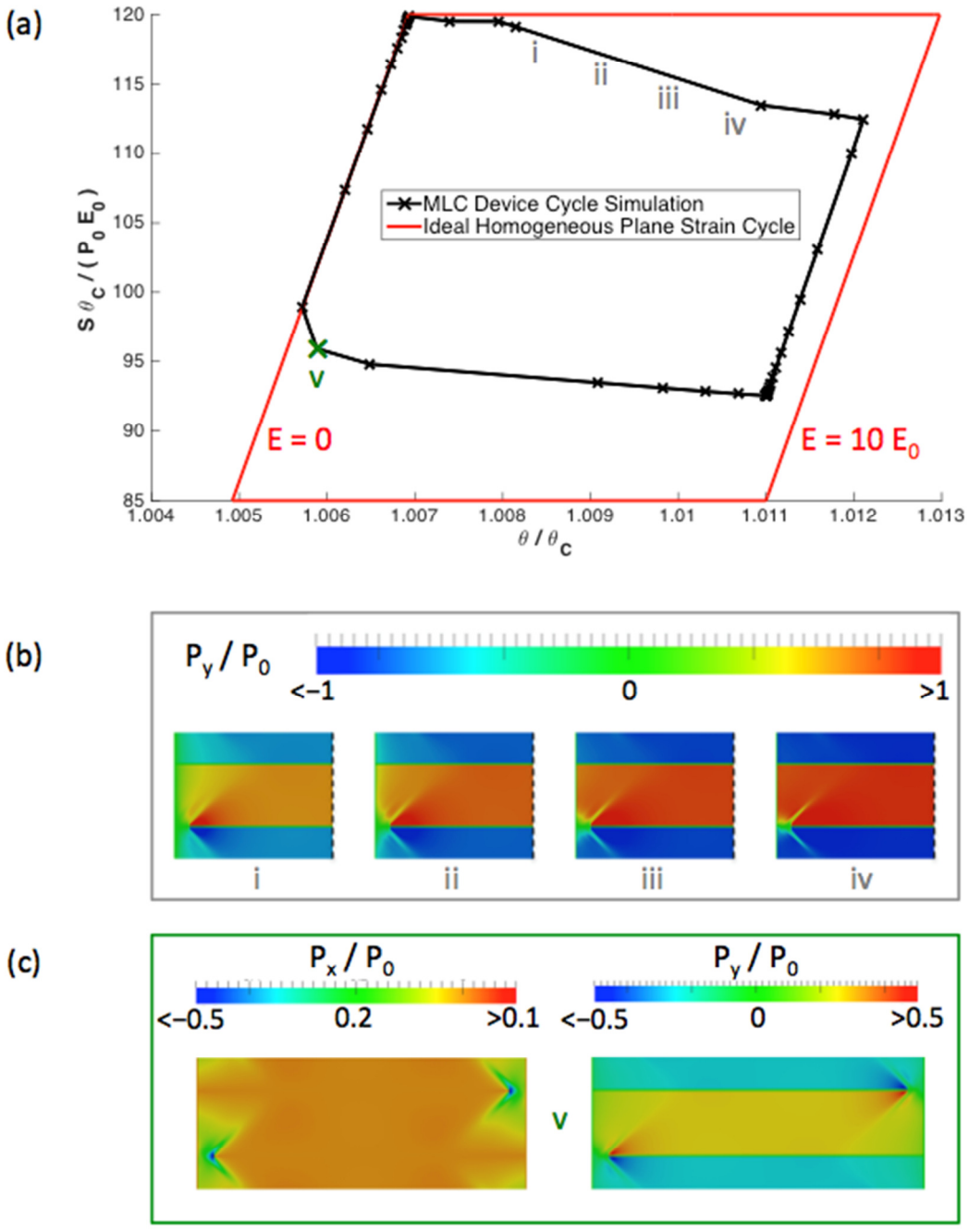

Figure 4.6: (a) The temperature vs. entropy plot for the simulation of the MLC EC cooling device as compared to the ideal homogeneous material cycle. (b) The section of the cycle in (a) labeled i-iv shows large changes in the polarization domain structure, as shown here in the *y*-polarization snapshots. (c) Once the electric field is removed (v), a residual ferroelectric state remains.

The simulation results for the full thermodynamic cooling cycle of the EC cooling device is show by the black curve in the temperature vs. entropy diagram in Fig. 4.6(a). The device completes the cycle at same point it begins, showing that the changes in the material, as modelled, are fully reversible. The adiabatic portions of the cycle do not remain isentropic as in the ideal cycle. The loss of entropy comes from the energy dissipated by the motion of the phase boundaries. The largest losses occur when the domain structure undergoes a large structural change, as shown in the progression of the *y*-polarization in Fig. 4.6(b). During the progression from state (i)-(iv), the polarization changes dramatically, going from the incomplete transformation to full transformation, as the *y*-aligned polarization wraps around the electrode tip, shrinking and surrounding the closure domains. The region of the curve where this transformation occurs shows the largest entropy loss due to dissipation. As expected, the steps with constant electric field follow a straight-line pattern, tending towards the applied temperature at those steps. There is little deviation from the ideal slope since changes in polarization are relatively small in this step and therefore energy dissipation is minimal. The uniform polarization between the electrodes increases from a magnitude of $P_y = 0.99P_0$ to $P_y = 1.03P_0$ as the entropy of the system decreases and heat leaves the system. The polarization for the plane strain monodomain at the high and low entropy points on the second leg are $P_y = 1.057P_0$ to $P_y = 1.063P_0$, respectively. Thus, the simulation, in the central uniform section, attains 94-96% of the ideal polarization magnitude. Once the

electric field is removed in the third leg of the cycle, a small amplitude residual ferroelectric state remains (Fig. 4.6(c)), with the polarization magnitude in the uniformly transformed central section equal to $0.26P_0$. This is due to the energy barrier which must be overcome to return the material to the fully paraelectric state. In the ideal plane strain case, the polarization at this point is equal to zero. In the final step of the cycle, the necessary energy input is provided from the heat source. As the heat is absorbed, the material transforms to a uniform temperature and zero polarization, thereby returning to the initial state, and matching the ideal plane strain case. The simulation tracks the predicted cycle well, with expected inefficiencies and losses due to energy dissipation. The causes of the inefficiency and suggestions on how they can be reduced are explored in the discussion section. In a real EC cooling device, there are likely to be other sources of energy loss that cannot be accounted for in this simulation, for example, imperfect heat transfer, poorly enforced adiabatic conditions, hysteresis due to pinning, electrical resistance and electrode/terminal yielding.

4.3 DISCUSSION

The simulation of the thermodynamic cooling cycle of an EC cooling device has several deviations from the ideal predicted cycle for a homogeneous plane strain EC material cooling cycle, shown by the black and red lines in Fig. 4.6, respectively. These deviations provide insight into the inefficiencies that exist in a MLC design. The area enclosed by the cycle in the temperature vs. entropy diagram

is the work done by the EC device [20]. From Fig. 4.6(a), we calculate that the MLC EC cooling device shows a loss of 41.2% as compared to the ideal state. We now address some losses and how they can be reduces.

First, as discussed previously, dissipation from phase boundary motion/evolution is not accounted for in the calculation of the ideal cycle, but contributes to a large entropy loss during the adiabatic part of the cycle. Specifically, the loss is most significant in the paraelectric to ferroelectric portion of the transformation. Theoretically, immediately inducing the full transformation in the material without traversing through the incomplete transformation first, should reduce the dissipation from boundary motion. However, our attempts to model such a scenario were not successful due to the instability of the polarization evolution with large instantaneous electric field changes. This suggests that such a dramatic transformation cannot occur without the intermediate stages of the transformation. Regardless, since it is necessary that the material transform phases for the operation of the device, we assume the inefficiency caused by polarization mobility cannot be readily reduced within the scope of this model. It should be noted, however, that the purity of the material (single crystal, no charge defects, vacancies or grain boundaries) presented in this simulation affects the ease of motion of the domain boundaries. The inclusion of defects would hinder domain wall motion [8], [45], [46] and thereby further decrease the efficiency of the cycle.

Another inefficiently is immediately evident in the incomplete transformation of the material as the electric field is applied. As seen in domain structures labeled "incomplete transformation" in Fig. 4.4, even after fields far above E_0 are applied, the material near the left and right model edges remains untransformed, thereby reducing the temperature change as compared to the ideal cycle. This is due to the confinement of the material in the MLC structure and is to be expected in any realistic model. The structural confinement includes the resistance to strain of the copper electrodes and terminals and the restriction of the material to plane strain conditions. As demonstrated in Fig. 4.3, just the application of plane strain suppresses the transformation temperature, thereby increasing the electric field necessary for spontaneous polarization at a given temperature. Logically, further confinement of the material will further suppress the phase transformation.

Once the EC material has fully transformed, there are still closure domains that exist between the idealy poled "up" and "down" phases. Figure 4.7 shows a schematic of the domains near the electrode tip for the incomplete and full transformation. The solid blue lines represent well-defined domain boundaries while the dashed blue lines denote diffuse boundaries. The domains that form in the structure are consistent with stable twin boundaries for tetragonal ferroelectric materials, with a well-defined 90° twin boundary at the tip of the electrode in both cases. The two "right" and "left" aligned domains in the full transformation do not meet at an electrically compatible boundary, and neither do the two "up" and

"down" domains. Therefore, the boundary between all four of these domain types forms a highly diffuse anti-vortex [47] structure.

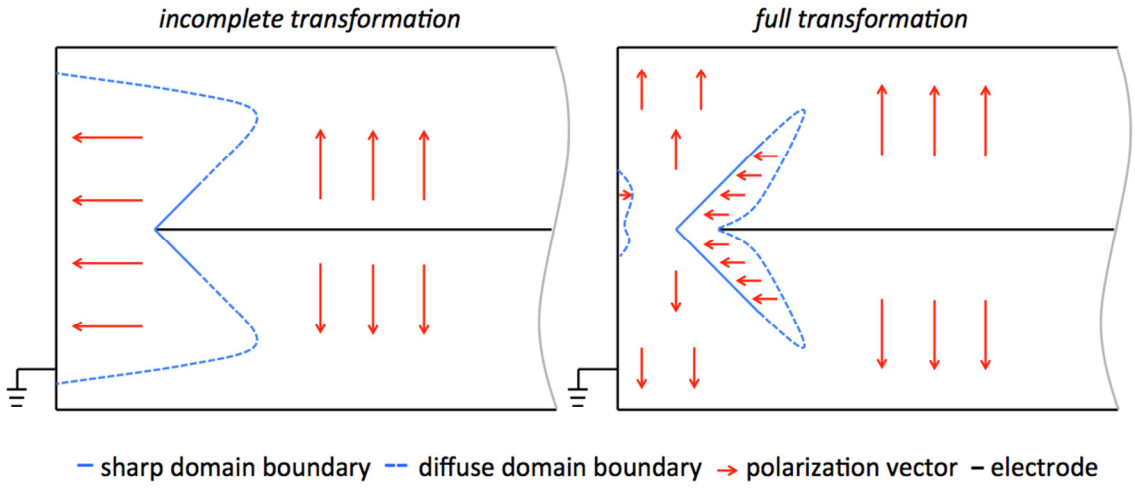

Figure 4.7: A schematic of the domain structure at the electrode tip in the MLC EC cooling device. Sharp boundaries are shown with solid blue lines and diffuse boundaries are shown with dashed blue lines. Red arrows indicate the direction of the polarization. The incomplete transformation has a single closure domain that bridges the two phases. The full transformation has two separate closure domains, with a diffuse quadruple point region between the domains.

The area near the electrode tip also exhibits large stresses, as shown in Fig. 4.8. Strain incompatibilities between domains and the EC material and copper electrode boundaries are the causes of the stresses, and the spikes in stresses closely follow domain boundaries and material interfaces. Though the electrode is rounded to minimize extreme stress behavior, the σ_{yy} stress at the electrode tip resembles stresses at a crack tip (or narrow elliptical hole or inclusion). In operation of the EC cooling device, it is clear that failure is most likely to occur at the

electrode tip. In fact, yielding and fracture in the electrode will be expected in this region, but is not modeled in our simulations.

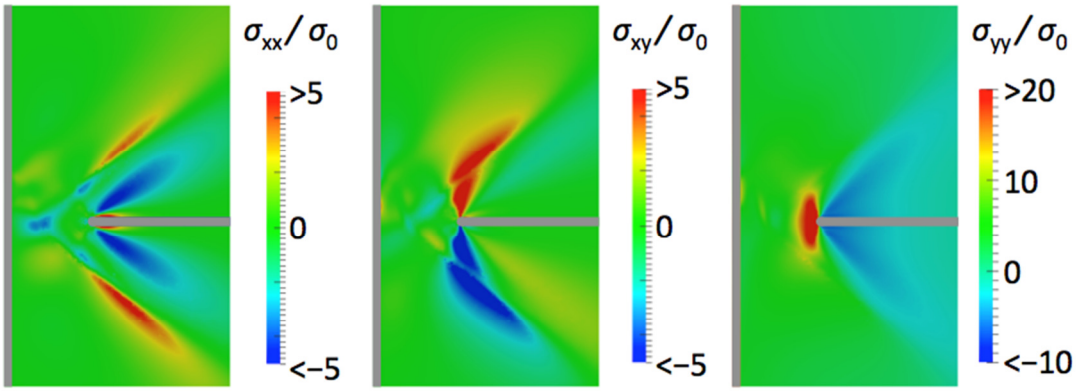

Figure 4.8: The stress distributions around the electrode tip in the MLC EC cooling device. The spike in stresses corresponds to domain boundaries and material interfaces. The electrode material is shown in grey.

The electromechanical incompatibilities in the electrode tip zone lead to a high energy state, with energy contributions from the large electric fields, high strains, and the presence of domain walls. Overall, the high energy zone creates inefficiency in the cycle that does not exist in the ideal transformation, thus reducing the temperature change that is achieved by the application of the electric field to the EC cooling device. Since this high energy zone is localized, increasing the length of the MLC geometry (relative to the distance between electrodes) can reduce its relative size. Creating a larger central zone where the EC material is uniformly transformed from paraelectric to ferroelectric with the application of the electric field will reduce the overall average energy density of the device, allowing for larger average temperature changes in the cooling cycle. However, the increase in length

will also increase the time required for the absorbing and removing heat from the EC device (as evident from Fig. 4.5), an important consideration in devices where quick operation through the cycle is expected.

Finally, we note that stresses in domain structure near the electrode tip are a function of the electrode tip geometry and the spacing between the electrode tip and terminal. The further study of these factors should be done to develop and optimized shape to minimize the energy of the electrode tip zone, but is beyond the scope of this work.

4.4 CONCLUSION

In summary, the model of the thermodynamic cooling cycle for a MLC EC cooling device and comparison of the results to the ideal plane strain monodomain cooling cycle suggests that device geometry plays a large role in the efficiency of the cycle. Factors including the length of the device, the gaps between electrode tip and terminal, electrode shape and thickness all impact the operation of device in the cooling cycle. Some confinement of the EC material and the formation of closure domains to resolve local incompatibilities are necessary in the operation of such a device, but many geometrical parameters can be optimized to better match the device performance to the ideal cooling cycle.

Chapter 5: Vortex domain structure and actuation in free-standing and transferred ferroelectric nanodots

The study of ferroelectric nanostructures (dots, rods, wires, disks) has been of great interest in the scientific community, in large part due their possible applications in nonvolatile ferroelectric random access memories (FeRAM) for microelectronics [48]–[51], where memory density could be greatly increased beyond current abilities by writing to individual nanoparticles. Nanostructures are also of interest in the general study of the miniaturization of ferroelectric devices like piezoelectric actuators and transducers, as well as other devices that make use of ferroelectric material properties. The formation of vortex domain structures has been widely predicted and shown by calculations from firsts principles [48], [50], though direct observation of standalone vortex structures is still lacking in the literature. Interest in the vortex structure arises from the possibility of "switching" the vortex direction by electric field [52], [53]. Vortex structures have been experimentally observed in larger ferroelectric structures outside of standalone nanodots. For instance Schilling, *et al.* observed single crystal dots that formed into quadrants with a complex array of 90° domains [49] and Balke *et al.* observed vortex structure and measured their conductive properties in thin film $BiFe0_3$ [47].

The need to study nanodots, specifically, rather than larger scale macroscopic structures, comes from the dramatic sensitivity to size that arises at

the *nano*-scale. In this study, we look at the domain/phase structure that forms as free-standing paraelectric nanodots are cooled past their transformation temperature, to see if the predicted vortex structures arise naturally. Moreover, we look at device thickness to explore whether out-of-plane polarizations can form upon cooling while the device is kept flat. Finally, we briefly explore the possibility of transferring the ferroelectric dots for use as actuators.

5.1 COOLING OF FREE-STANDING NANODOTS FROM THE PARAELECTRIC PHASE

The simulation of the paraelectric to ferroelectric phase transition of the nanodot structure is performed using a fully three-dimensional nonlinear finite element model with displacement, potential, polarization and temperature as nodal degrees of freedom. For details on the formulation of the finite element formulation, see Chapter 2. The geometry of the nanodot structure is square in the *x*-*y* plane, with size lengths of $10l_0$ or $20l_0$, depending on the simulation. The height in the *z*-direction vary between $0.5l_0$ and $2l_0$, depending on the simulation. Note that the width of an unstressed 180° domain wall is $2l_0$ and a 90° domain wall is $3l_0$ at room temperature [8]. The dot structure is initialized as a free-standing paraelectric structure. The polarization in initialized with a random smoothed nonzero polarization of maximum magnitude $P_0 \times 10^{-7}$ in all directions. This in necessary since the paraelectric state is a metastable equilibrium point just below the Curie temperature, and then becomes an unstable equilibrium point with continued cooling. Thus, the paraelectric state could computationally continue to be a perfect (though unstable) solution for the dot structure far beyond the physical stability of such a structure, so a nonzero initialization is necessary for nucleation of the

ferroelectric state. A single corner node is grounded and the structure is prevented from rigid-body displacement and rotation. The top and bottom surfaces of the dot structure are kept parallel to the *x-y* plane, creating generalized plane strain conditions, but the strain is not specified, allowing for average stress-free conditions in all directions. This boundary condition is imposed for future transfer of the dot, which would require a flat surface for full adhesion.

The dot is cooled by applying a temperature change of $\Delta\theta = 0.01\theta_C$ and allowing the structure to evolve in time. This relatively slow temperature change prevents the structure from being shocked into a higher energy state with a greater number of domains. Since $BaTiO_3$ exhibits a first-order phase transition, the paraelectric state is still energetically stable for a small range of temperatures below the Curie temperature, though it is not the lowest energy state. Therefore, the transition to a ferroelectric state is expected at a temperature below the Curie temperature, but not necessarily immediately upon cooling below it. Figure 5.1 shows a schematic of the expected transition to the vortex structure. The compatible paraelectric dot, upon cooling, reaches a state where it is no longer thermodynamically stable. At this point, ferroelectric domains form in the material. For electrical compatibility, the ferroelectric vortex structure is expected to form, with 90° domain boundaries between each of the domains. However, as seen in the figure, the deformed shape of each of four ferroelectric domains, while meeting at electrically compatible boundaries, do not fit together in a mechanically compatible way. Therefore, the material must be strained to remain intact, with a particularly high strain at the quadruple-point in the center. Since the strained domain boundaries will be high-energy, the transformation temperature could be further suppressed.

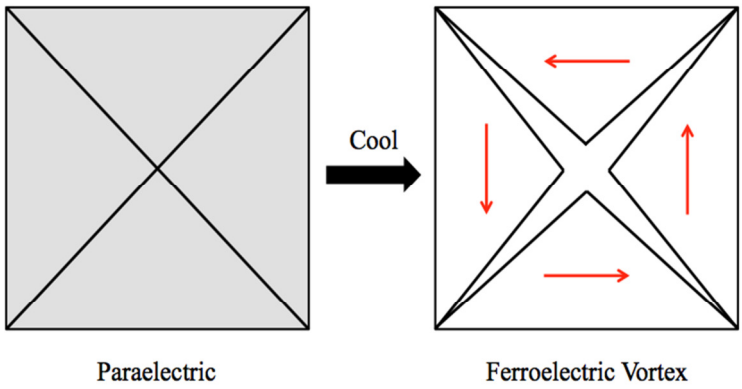

Figure 5.1: The transition of the paraelectric free-standing dot to the ferroelectric vortex structure upon cooling. The ferroelectric structure shows the deformed shape of each spontaneously strained domain. The mechanical incompatibility in the nanodot structure must be resolved by straining the material such that the domain boundaries meet.

The first two simulations are done with dots with the dimensions $20l_0 \times 20l_0 \times 0.5l_0$ and $10l_0 \times 10l_0 \times 0.5l_0$ to demonstrate the size sensitivity of the domain structure of the dots. The dot structures are essentially thin films with all problem variables invariant in the z-direction. Figure 5.2 shows the domain structures that form in each of the dots. For the larger dot, the domains form into a double vortex structure, similar to those predicted by Kontsos and Landis for ferroelectric thin films with periodic boundaries [24]. For the smaller dot, a single vortex structure forms. The "ideal" vortex structure is not found, however, as the y-domains elongate to form two triple-point junctions and a 180° domain boundary instead of a single quadruple point. The two structures also have disparate transition temperatures, with the larger dot forming ferroelectric domains at $\theta = 0.96\theta_C$ and the smaller dot at $\theta = 0.95\theta_C$. While both the models are three-dimensional and thus allow for z-polarization, the spontaneous polarization upon

transition is entirely in the *x*-*y* plane. This is expected, given that the model thickness is smaller than domain wall thickness.

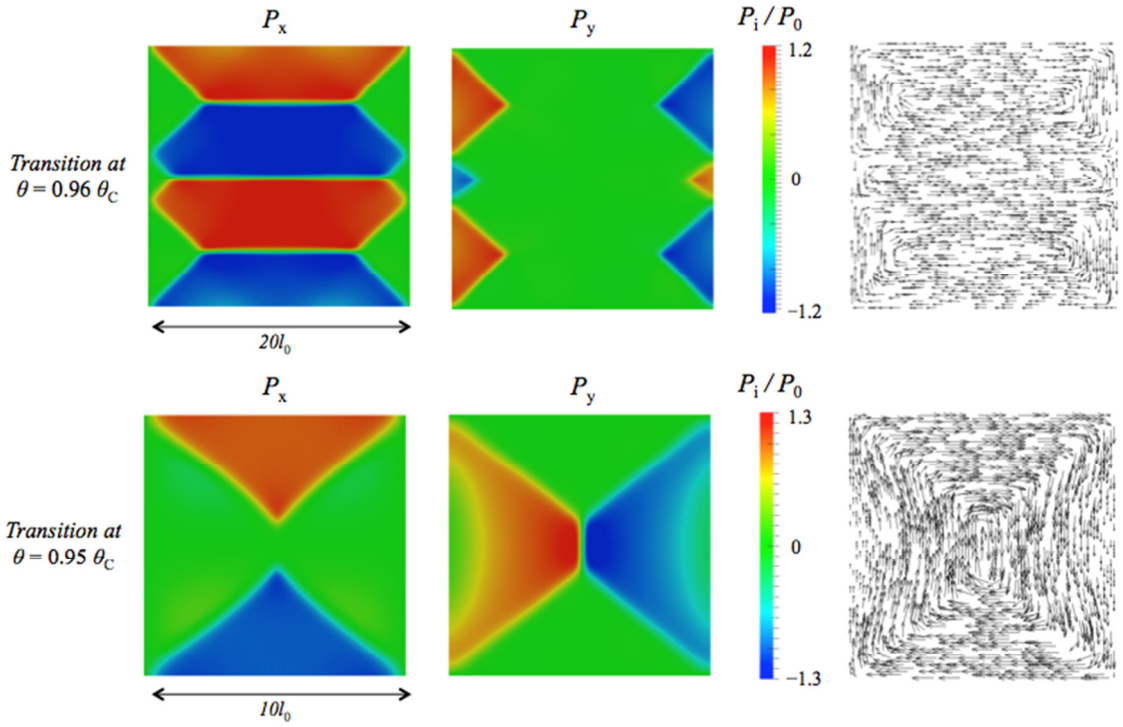

Figure 5.2: The domain structures that form in the $20l_0 \times 20l_0 \times 0.5l_0$ and $10l_0 \times 10l_0 \times 0.5l_0$ as they cool through the transition temperature indicated for each. Neither model forms the ideal vortex structure with the larger model forming multiple vortex domains reminiscent of thin film domain structures. The third panel for each model size gives a vector map of the polarization.

Increasing the thickness of the model creates the opportunity for more complex domain structures, with possible out-of-plane polarization. It also allows us to explore whether the non-ideal vortex structure seen in the spontaneous domain can become ideal with greater thickness. We therefore model a $10l_0 \times 10l_0 \times l_0$ and $10l_0 \times 10l_0 \times 2l_0$ dot and compare them to the previous results. Figure 5.3 shows the domain structure for both models, with the ideal vortex structure forming

immediately upon phase transformation. The phase transition occurs at $\theta = 0.97\theta_C$ for both, a higher transition temperature than the thinner model shown in Fig. 5.2. The local electric field produced by the vortex structure does not follow the vortex structure, as was predicted for cubic free-standing dots by Prosandeev and Bellaiche [50], but instead is more erratic, switching directions within each domain. The third diagram for each simulation shown in Fig. 5.3 shows a schematic of the electric field in the model. The grey dashed lines show where the electric field goes to zero, separating the model into 12 distinct zones. The electric field is also zero at the quadruple point. As before, though only the *x*-*y* plane is shown, the model is fully three-dimensional, but all problem variables are invariant in the *z*-direction at the temperature shown. The reader may note that the vortices in the two structures have opposite spin. This is not the result of some structural difference, but rather a random effect that arises from the small random polarization distribution that is present in each model's initial state and from which the vortex structures nucleate.

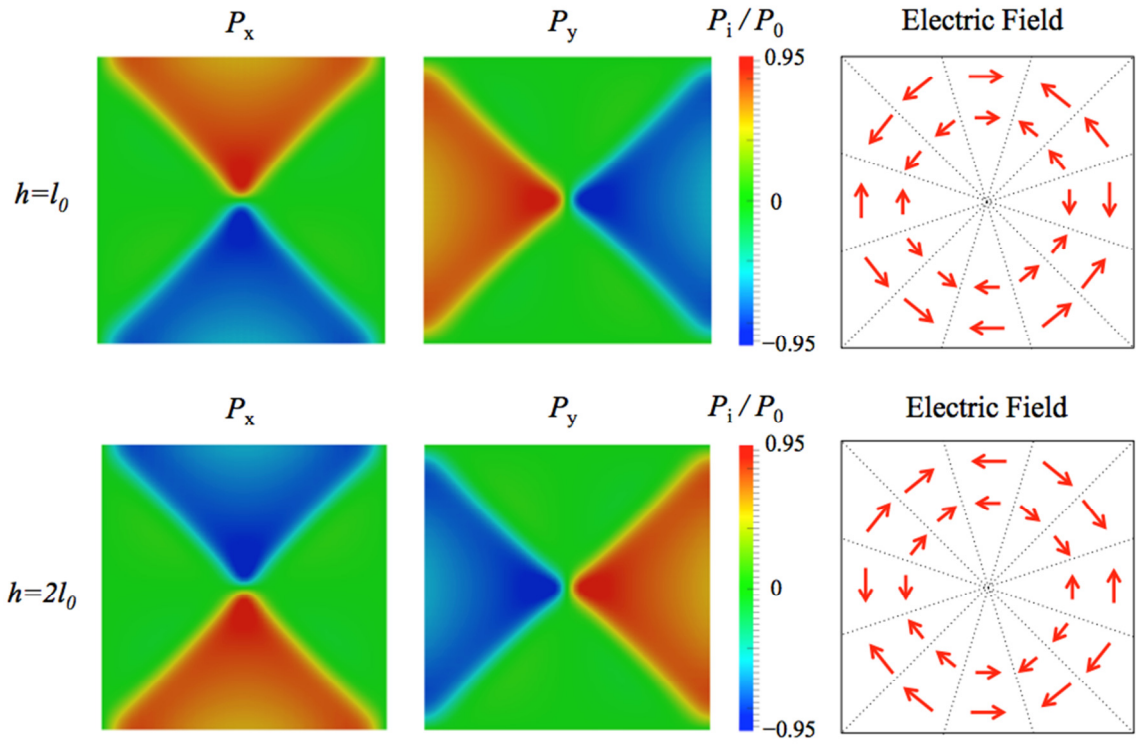

Figure 5.3: The polarization in the x- and y-direction and schematic of the electric field for the $10l_0 \times 10l_0 \times l_0$ and $10l_0 \times 10l_0 \times 2l_0$ dot structure at their transition temperature $\theta = 0.97\theta_C$. The dashed black lines on the electric field schematic indicate lines along which the electric field goes to zero and red arrows indicate the direction and magnitude of the local field.

The domain structure that forms upon transition from paraelectric to ferroelectric does not remain unchanged as the dots cool to room temperature. For the $10l_0 \times 10l_0 \times 0.5l_0$ dot, further cooling actually brings the dot into the ideal vortex shape. And for $10l_0 \times 10l_0$ based dots of all three thicknesses studied, cooling eventually leads to a loss of ideal vortex structure, and the formation of a more complex domain structure. This restructuring occurs when the maximum magnitude of the polarization is far above P_0. The loss of the ideal vortex structure relieves

some of the local strain energy that arises from resolving the mechanical incompatibility caused by the shape change in the vortex. The deformed shape of the models right before and right after the loss of symmetry is shown in Fig. 5.4(a) and (b). The shape change is completely different in the two models, yet again showing strong size dependence, this time due to the thickness of the model. In Fig. 5.4(a), the shape change stretches the dot in one of the planar directions while contracting in the other. The quadruple point separates into two triple points and a 180° boundary. In the largest model (thickness $2l_0$), whose deformed shape and polarization magnitude are shown in Fig. 5.4(b), nonzero polarization in the *z*-direction finally appears, causing bulges to form along the four narrow faces with *x*- and *y*-direction normal vectors. The *z*-domains do not continue through the entire thickness of the dot so the material is no longer invariant in the *z*-direction. The polarization in the *z*-direction for the full dot is shown on the deformed shape is Fig. 5.4(c), along with a cutaway of the *z*-aligned polarization halfway through the thickness of the dot structure. The average of the polarization must be zero in all directions since there are no unbalanced charges on the surfaces, but the formation of the small *z*-domains reduces local axial stresses, specifically at the quadruple point, which remains intact. Overall, the cooling leads to the formation of new domain structures as the vortex becomes unstable. The shape and arrangement of the new domain structure seems highly dependent on the thickness of the dot.

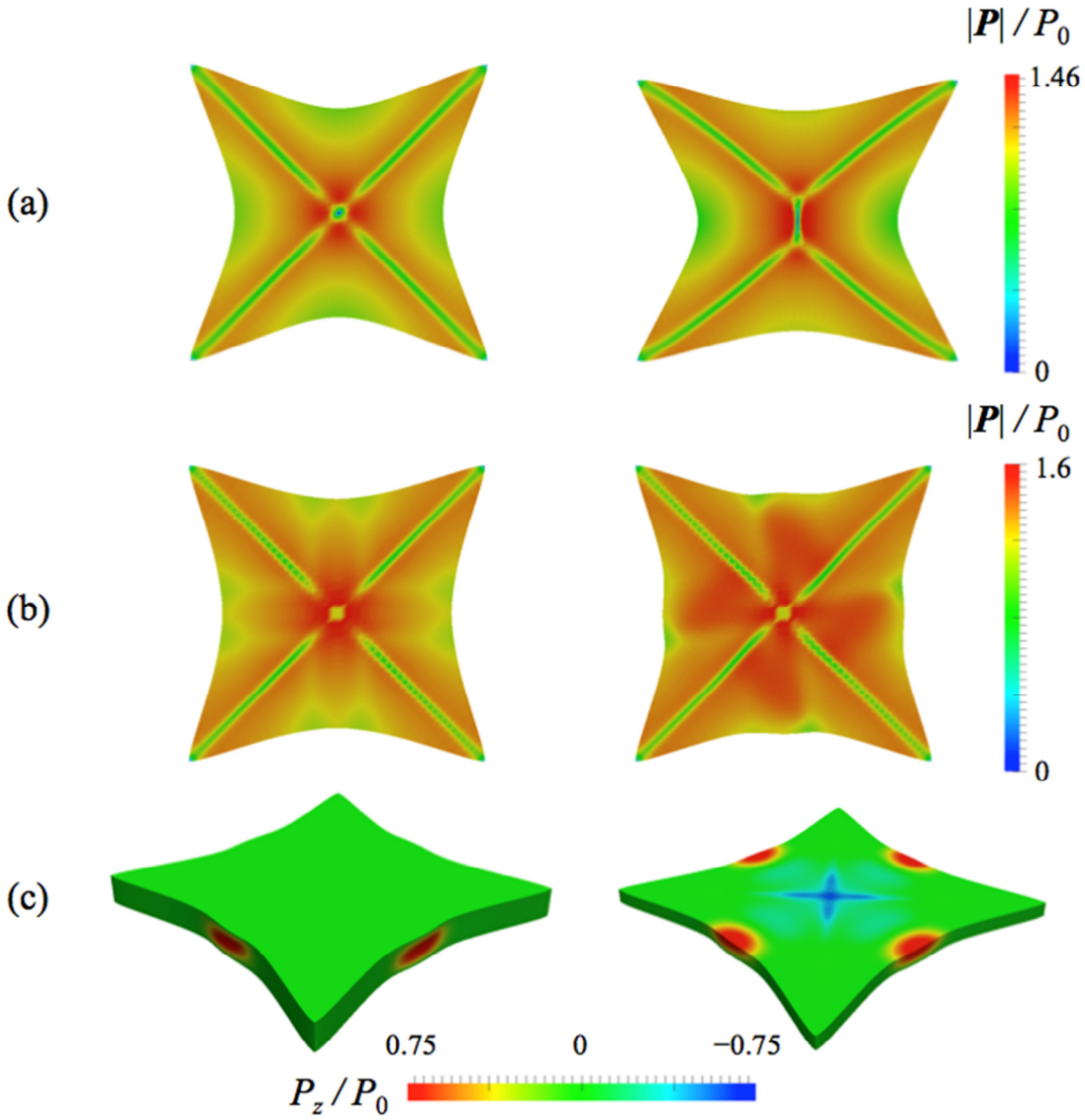

Figure 5.4: The deformed shape of cooled nanodots before and after the loss of the perfect vortex structure. (a) The $10l_0 \times 10l_0 \times l_0$ dot changes shape and elongates along one planar axis, changing the quadruple point into two triple points and a 180° domain wall. (b) The $10l_0 \times 10l_0 \times 2l_0$ dot develops bulges at the free edges of the 4 vortex domains. The bulges form from the spontaneous z-polarization at the edges, and are shown for both the whole dot and with a cutaway halfway through the height in panel (c).

5.2 TRANSFERRED NANODOTS FOR ACTUATION

One of the possible uses of ferroelectric nanodots is for the actuation at the *nano*-scale. To test this functionality, we assume manufacturing of the nanodots that is consistent with some of the processes described in the literature for $BaTiO_3$ dot array formation [54]. For this simulation, the initial state of the dot is the room temperature deformed shape computed by the simulations in Section 5.1. This assumes that the dot is manufactured at a high temperature, and then cooled with the constraint that the top and bottom surfaces remain flat. Then the dot is transferred to a conductive/electrode surface, and a conductive layer coats the top of the dots as well. The substrate onto which the dot is transferred is considered rigid and the dot is perfectly bonded to the surface, so the entire bottom/substrate surface boundary conditions are fixed at the initial values in all three directions. The bottom electrode is grounded and the top electrode has an applied potential, creating a nonzero out-of-plane electric field. The top electrode is assumed to provide no resistance to deformation.

The goal of this simulation is to induce domain switching from in-plane to out-of-plane ferroelectric phases. Such a switch would be accompanied by a large change in out-of-plane displacement. Since the initial vortex-like structure contains mostly in-plane phases, the strain in the *z*-direction is, on average, negative, relative to the cubic/paraelectric phase. Switching to mostly *z*-polarization would make *z*-

strains mostly positive, as the tetragonal axis of the dominant domain would become the z-axis. Thus, the dot could theoretically be used a nano-actuator.

Figure 5.5 shows the results of the actuation simulation for the $10l_0 \times 10l_0 \times 2l_0$ dot structure. Just the application of the electrodes (which allows for unbalanced spontaneous polarizations in the z-direction), leads to an average spontaneous polarization of $\bar{P}_z = 0.18P_0$ at zero average electric field. Most of the spontaneous out-of-plane polarization is localized to the free edges of each domain and the 90° domain boundaries. As the electric field is increased, up to a value of $\bar{E}_z = -5E_0$, the polarization in the z-direction decreases to $\bar{P}_z = -0.83P_0$, with large non-zero out-of-plane polarization throughout most of the model, though ample localization is still evident. It is important to note that contrary to our predictions, the domains do not switch from in-plane ferroelectric to out-of-plane ferroelectric. The out-of-plane polarization forms *in addition* to the in-plane domains, which are still present at the high out-of-plane electric fields. Under the same electric field and temperature, a bulk monodomain would have an induced uniform polarization of $P_z = -1.45P_0$. Also, it is useful to note that the sign of the electric field does not significantly affect the results of the actuation simulation. While the domain structures for an electric field of $+5E_0$ differ slightly from those shown in Fig. 5.5, the general trends in polarization and displacement are very similar.

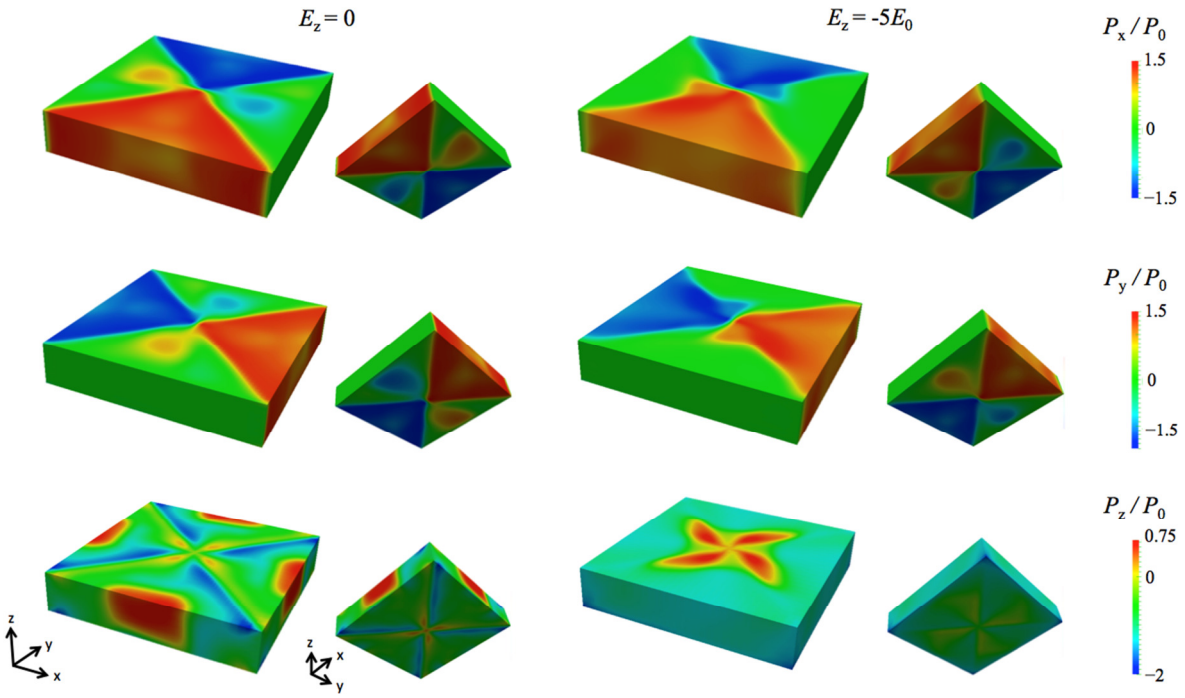

Figure 5.5: The $10l_0 \times 10l_0 \times 2l_0$ dot with fixed displacements on the bottom surface and electrodes on the top and bottom z-surfaces. The electrodes are used to create an average nonzero out-of-plane electric field. The average polarization in the z-direction is $P_z = 0.14P_0$ at zero electric field and $P_z = -0.83P_0$ at an electric field of $E_z = -5E_0$. The in-plane domains do not switch to form z-domains, and instead, z-domains form in addition to the x- and y-polarization.

The deformed shape at the largest electric field is shown in Fig. 5.6, with the colormap indicating the displacement in the z-direction. The largest deformation is at the edges of the dot, where there is the least confinement. The central portion of the dot actually has negative deformation, suggesting the polarization there is dominated by the in-plane phases. From these results, it is evident that the shape change is not as large as would be possible with full polarization switching. For reference, in the bulk monodomain ferroelectric crystal at room temperature, the

displacement at the top edge of the model would switch from $u_z = -1.40 l_0 \varepsilon_0$ to $u_z = 4.20 l_0 \varepsilon_0$ as the polarization switches from in plane to out-of-plane with the applied electric field of $-5E_0$. In the vortex nano-actuator model, the displacements switch from a uniform value of $u_z = -1.16 l_0 \varepsilon_0$ to a maximum out-of-plane deformation of $u_z^{max} = 3.98 l_0 \varepsilon_0$. However, the maximum value is only achieved at the four free corners of the dot, and the average deformation of the top surface is only $\bar{u}_z = 0.45 l_0 \varepsilon_0$. While this value is still a dramatic change from the initial state, it achieves only 11% of the possible deformation for an unconstrained material under identical temperature and electric field conditions. For this reason, the type of dot manufacturing and transferring described in this section is obviously not the most ideal for actuation applications. A better option would transfer the dot with smaller initial strains, so that switching would not be suppressed by the suboptimal displacement boundary conditions. Another option would be to use a compliant substrate.

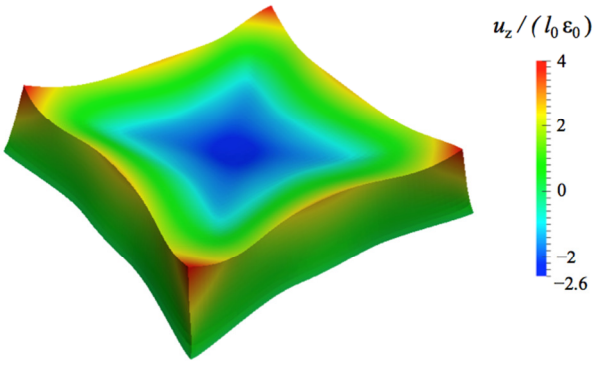

Figure 5.6: The deformed shape of the actuated dot shown in Fig. 5.5 at an average electric field of $\bar{E}_Z = -5E_0$. The displacement in the z-direction is shown by the colormap, with maximum deformation $u_z^{max} = 3.98 l_0 \varepsilon_0$ at the model corners.

5.3 CONCLUSION

This chapter models shape and polarization of ferroelectric nanodots formed by cooling an ideal isothermal paraelectric dot, with boundary conditions restricting the top and bottom surface to remain flat. As predicted by literature, a polarization vortex domain structure forms in sufficiently small dot structures. The formation of the vortex is highly dependent on the in-plane size and out-of-plane height. Dots with heights smaller than the domain wall width do not exhibit a variation through the thickness, while taller dots develop out-of-plane polarization at certain temperatures. The use of transferred nanodots for actuation is also explored by applying an electrode to the top and bottom surface of the cooled nanodot structure and fixing the displacement at the substrate. While the application of an electric field to this structure does result in the formation of large out-of-plane polarizations, full domain switching does not occur, resulting in significantly suppressed deformation. Therefore, we conclude that the simulated setup is not ideal for use in actuation, and a setup with smaller initial deformation/strain at the substrate or a more compliant substrate would likely allow for larger deformations.

Chapter 6: Conclusion and future work

Ferroelectric materials form complex domain structures that are well suited to analysis using phase-field modeling techniques. In this dissertation, several topics relating to the modeling of temperature-dependent behavior of ferroelectric barium titanate were explored. First, we developed a continuum thermodynamics theory for modeling the full thermo-electro-mechanical coupling that exists in ferroelectric materials. This theory expands on previous work by including the temperature as a degree of freedom, thus necessitating a fourth governing equation to model the temperature behavior. The governing equation for temperature is derived from the first and second laws of thermodynamics, and is a highly coupled heat conduction equation. With the inclusion of temperature, and the resulting time-dependent thermal diffusion, the nonlinear finite element model must solve for the full evolution of the fields rather than solving for an equilibrium state. The energy-based theory uses an eight order polynomial free energy function to model the full behavior of the material. The energy function has a single-well shape above the Curie temperature and a multi-well shape below the Curie temperature. However, near the Curie temperature, both the paraelectric and ferroelectric phases are stable or metastable. At a specific phase coexistence temperature, given certain electromechanical matching conditions, the two phases can coexist.

The structure of the stable isothermal paraelectric to ferroelectric phase boundary in two dimensions was modeled for a variety of domain widths under generalized plane strain conditions. The structure, excess energy, phase-coexistence temperature, and entropy jump of the boundary was calculated as a function of the domain width of the ferroelectric laminate. We demonstrate that the boundary structure is stable and can move through the material with entropy/heat input control. Since only a two dimensional boundary is modeled in this dissertation, future work should expand this boundary to three dimensions with higher-order laminate ferroelectric structures. Also, the hysteretic behavior of the FE-PE phase boundary is of great interest for applications and should be quantified in further studies.

One of the novel properties of ferroelectric materials like barium titanate is that they exhibit the electrocaloric effect, an adiabatic change in temperature upon the application of an electric field. This effect can be harnessed to create electrocaloric cooling devices. Using a multi-layer capacitor style layout with electrocaloric material between interdigitated electrodes, we modeled the thermodynamic cooling cycle of such a device for a representative unit cell. The device matched the general shape of the ideal cooling cycle for a plane strain electrocaloric material, but certain inefficiencies exist that led to a 41% loss in energy for the modeled case. Specifically, inefficiencies arose from the formation of closure domain structures around the electrode tip. Also, large stress fields

developed at the material interface between the electrode and electrocaloric material near the electrode tip. These inefficiencies, amongst others discussed, should be investigated in the future work. The shape of the electrode and geometry of the cooling device should be varied in a parametric study to find optimal shapes and sizes to maximize the efficacy of the electrocaloric cooling device.

The final study in this dissertation focused on the formation of vortex structures by cooling paraelectric nanodots through the Curie temperature. The dots are thin relative to their square cross section. For the sake of transferring applications, the dots are kept flat on the top and bottom. The predicted vortex structure forms for dots of a certain size, while larger dots form larger more complex domains, reminiscent of thin films. The final domain structure and shape upon cooling to room temperature is highly dependent on the height of the dot. Dots with heights equal to or greater than the domain wall thickness form spontaneous out-of-plane polarizations that vary through the thickness. The transfer of the dots to a rigid surface at room temperature and the application of electrodes to the top and bottom allow for actuation via electric field. However, while the dot does develop a large out-of-plane polarization that aligns with the electric field, the switching from in-plane to out-of-plane polarization never fully occurs, and both in-plane and out-of-plane polarizations coexist, suppressing the possible actuation displacement. Therefore, we conclude that this specific transfer method presented

here is not optimal, and suggest that future work explore other actuation techniques with less restrictive boundary conditions.

Appendix A: Helmholtz free energy and material properties for barium titanate and copper

The general form of the Helmholtz free energy function is presented in Eq. 2.29. The material tensors must all have the symmetry of the highest symmetry phase, cubic, thus drastically reducing the number of nonzero terms in the free energy. The fully expanded free energy function used in the simulation of barium titanate presented in Chapters 3-5 is shown in Eq. A1. Here, the free energy is written as a function of the spontaneous strain (ε_{ij}^{0}), which is the strain that arises in the crystal under stress-free boundary conditions. The free energy is

$$\psi = \frac{a_0}{2}\left(P_{x,x}^2 + P_{y,y}^2 + P_{z,z}^2 + P_{x,y}^2 + P_{y,x}^2 + P_{x,z}^2 + P_{z,x}^2 + P_{y,z}^2 + P_{z,y}^2\right)$$
$$+\alpha_1(\theta - \theta_0)\left(P_x^2 + P_y^2 + P_z^2\right) + \alpha_{11}\left(P_x^4 + P_y^4 + P_z^4\right)$$
$$+ \alpha_{12}\left(P_x^2P_y^2 + P_x^2P_z^2 + P_z^2P_y^2\right) + \alpha_{111}\left(P_x^6 + P_y^6 + P_z^6\right)$$
$$+ \alpha_{112}\left(P_x^2\left(P_y^4 + P_z^4\right) + P_y^2(P_x^4 + P_z^4) + P_z^2\left(P_x^4 + P_y^4\right)\right)$$
$$+ \alpha_{123}P_x^2P_y^2P_z^2 + \alpha_{1111}\left(P_x^8 + P_y^8 + P_z^8\right)$$
$$+ \alpha_{1112}\left(P_x^6\left(P_y^2 + P_z^2\right) + P_y^6(P_x^2 + P_z^2) + P_z^6\left(P_x^2 + P_y^2\right)\right)$$
$$+ \alpha_{1122}\left(P_x^4P_y^4 + P_x^4P_z^4 + P_z^4P_y^4\right)$$
$$+ \alpha_{1123}\left(P_x^4P_y^2P_z^2 + P_x^2P_y^4P_z^2 + P_x^2P_y^2P_z^4\right)$$
$$+\frac{1}{2}C_{11}\left((\varepsilon_{xx} - \varepsilon_{xx}^0)^2 + \left(\varepsilon_{yy} - \varepsilon_{yy}^0\right)^2 + (\varepsilon_{zz} - \varepsilon_{zz}^0)^2\right)$$
$$+ C_{12}\left((\varepsilon_{xx} - \varepsilon_{xx}^0)\left(\varepsilon_{yy} - \varepsilon_{yy}^0\right) + (\varepsilon_{xx} - \varepsilon_{xx}^0)(\varepsilon_{zz} - \varepsilon_{zz}^0)\right.$$
$$\left. + (\varepsilon_{zz} - \varepsilon_{zz}^0)\left(\varepsilon_{yy} - \varepsilon_{yy}^0\right)\right)$$
$$+\frac{1}{2}C_{44}\left(\left(\varepsilon_{xy} - \varepsilon_{xy}^0\right)^2 + \left(\varepsilon_{yx} - \varepsilon_{yx}^0\right)^2 + 2\left(\varepsilon_{xy} - \varepsilon_{xy}^0\right)\left(\varepsilon_{yx} - \varepsilon_{yx}^0\right)\right.$$
$$+ (\varepsilon_{xz} - \varepsilon_{xz}^0)^2 + (\varepsilon_{zx} - \varepsilon_{zx}^0)^2 + 2(\varepsilon_{xz} - \varepsilon_{xz}^0)(\varepsilon_{zx} - \varepsilon_{zx}^0)$$
$$\left. + \left(\varepsilon_{zy} - \varepsilon_{zy}^0\right)^2 + \left(\varepsilon_{yz} - \varepsilon_{yz}^0\right)^2 + 2\left(\varepsilon_{zy} - \varepsilon_{zy}^0\right)\left(\varepsilon_{yz} - \varepsilon_{yz}^0\right)\right)$$
$$+\frac{1}{2\kappa_0}\left((D_x - P_x)^2 + \left(D_y - P_y\right)^2 + (D_z - P_z)^2\right) + \tilde{\beta}_{ij}(\theta - \theta_1)\varepsilon_{ij}$$
$$+ C_P\left[(\theta - \theta_2) - \theta\ln\left(\frac{\theta}{\theta_2}\right)\right] \qquad \text{(A1)}$$

The spontaneous strains can be calculated from the polarization as follows:

$$\varepsilon_{xx}^{0} = Q_{11}P_x^2 + Q_{12}\left(P_y^2 + P_z^2\right)$$

$$\varepsilon_{yy}^{0} = Q_{11}P_y^2 + Q_{12}(P_x^2 + P_z^2)$$

$$\varepsilon_{zz}^{0} = Q_{11}P_z^2 + Q_{12}\left(P_y^2 + P_x^2\right)$$

$$\varepsilon_{xy}^{0} = \varepsilon_{yx}^{0} = \frac{1}{2}\left(Q_{44}P_xP_y\right) \qquad \text{(A2)}$$

$$\varepsilon_{xz}^{0} = \varepsilon_{zx}^{0} = \frac{1}{2}(Q_{44}P_xP_z)$$

$$\varepsilon_{zy}^{0} = \varepsilon_{yz}^{0} = \frac{1}{2}\left(Q_{44}P_zP_y\right)$$

The parameter a_0 in the free energy function in Eq. A1 gives rise to finite thickness domain walls and is related to the domain wall thickness parameter l_0 as given in Eq. 3.5.

The coefficients for the eighth order Landau-Devonshire potential for barium titanate are taken from the literature [34], [55]

$$\alpha_1(\theta-\theta_0) = 4.124\times10^5\,(\theta - 388\,K)\;\; N\,m^2/C^2K$$

$$\alpha_{11} = -2.097\times10^8\;\; N\,m^6/C^4$$

$$\alpha_{12} = 7.974\times10^8\;\; N\,m^6/C^4$$

$$\alpha_{111} = 1.294\times10^9\;\; N\,m^{10}/C^6$$

$$\alpha_{112} = -1.95\times10^9\;\; N\,m^{10}/C^6$$

$$\alpha_{123} = -2.5009\times10^9\;\; N\,m^{10}/C^6 \qquad \text{(A3)}$$

$$\alpha_{1111} = 3.863\times10^{10}\;\; N\,m^{14}/C^8$$

$$\alpha_{1112} = 2.529\times10^{10}\;\; N\,m^{14}/C^8$$

$$\alpha_{1122} = 1.637\times10^{10}\;\; N\,m^{14}/C^8$$

$$\alpha_{1123} = 1.367\times10^{10}\;\; N\,m^{14}/C^8$$

The electrostrictive and elastic coefficients are [55]

$$Q_{11} = 0.10\;\; m^4/C^2$$

$$Q_{12} = -0.034\;\; m^4/C^2$$

$$Q_{44} = 0.029\;\; m^4/C^2 \qquad \text{(A4)}$$

$$C_{11} = 1.78\times10^{11}\;\; N/m^2$$

$$C_{12} = 0.964\times10^{11}\;\; N/m^2$$

$$C_{44} = 1.22\times10^{11}\; N/m^2$$

and the permittivity of free space is

$$\kappa_0 = -8.854\times10^{-12}\; C^2/Nm^2\,. \qquad \text{(A5)}$$

The two final terms in Eq. A1 are the energy from the thermal expansion and specific heat of the material. The parameters $\tilde{\beta}_{ij}$ and C_P are related to the thermal expansion coefficients and the specific heat capacity, respectively. The parameters θ_1 and θ_2 are two baseline temperatures used for the thermal expansion and heat capacity calculations.

The free energy function and quantities presented in above are used consistently for all simulations in Chapter 3-5 for the barium titanate material. However, each chapter does have some unique parameter choices specific to the problem, and those quantities are discussed individually below.

A.1 Ferroelectric-paraelectric phase boundary simulation parameters

For the isothermal calculations in Chapter 3, both thermal expansion and heat capacity terms (temperature-dependent terms) are not included. While this does change the baseline value of the entropy, which then becomes zero in the paraelectric state, it does not impact the results.

For the two-dimensional generalized plane strain condition applied to the ferroelectric-paraelectric phase boundary model, the axial strain in the z-direction is set to a constant $\varepsilon_{zz}^{*} = 0.4501\, Q_{12}$, such that the paraelectric monodomain and ferroelectric monodomain have the same energy under field-free conditions at the Curie temperature. In the bulk free material, the two monodomains have the same free energy at the Curie temperature. This is the situation that we aim to simulate.

Displacement boundary conditions used to constrain the 180° laminate FE-PE phase boundary are given in Eq. 3.4. The rigid body motion and rotation are given below as functions of the angle of the boundary, α, the average x- and y-strains, ε_a and ε_c, in the ferroelectric phase, and the equibiaxial strain ε_p in the paraelectric phase.

$$u_x^0 = \frac{5w}{\tan\alpha}\left(\varepsilon_p - \varepsilon_a\right)$$

$$u_y^0 = 5w\ (\varepsilon_c - \varepsilon_p) \qquad \text{(A.6)}$$

$$\omega_0 = \frac{\left(\varepsilon_p - \varepsilon_a\right)}{\tan\alpha}$$

The rigid body displacements and rotations given above are specific to a boundary located halfway between the edges of the model. They are computed assuming a perfect planar boundary without closure domains.

A.2 ELECTROCALORIC COOLING DEVICE MODEL PARAMETERS

Chapter 4 presents a bimaterial problem, so beyond the free energy and parameters for the barium titanate (Eqs. A.1-A.5), the material properties and behavior of copper must also be considered. The free energy function for copper is given by

$$\psi = \frac{\lambda}{2}\varepsilon_{ii}\varepsilon_{jj} + \mu\varepsilon_{ij}\varepsilon_{ij} + \tilde{\beta}_1^{Cu}(\theta - \theta_1^{Cu})\varepsilon_{ii} + C_P^{Cu}((\theta - \theta_2^{Cu}) - \theta \ln\left(\frac{\theta}{\theta_2^{Cu}}\right) \quad \text{(A.7)}$$

where the superscript Cu indicated the material property for copper. This is a standard isotropic elasticity model for the free energy, with the thermal expansion and specific heat terms added. Plane strain is assumed so $\varepsilon_{zz} = 0$. The Lamé parameters λ and μ for polycrystalline copper are [56]

$$\lambda = 71\ GPa$$
$$\mu = 33.4\ GPa\ . \quad \text{(A.8)}$$

For the bimaterial model, the thermal expansion is not included in the copper or electrocaloric material. This is done for simplicity since a matching baseline temperature (θ_1 and θ_1^{Cu}) would need to be chosen somewhat arbitrarily. Since the temperature range in the problem is small, the thermal expansion plays a minor role. Further studies could investigate the effect of manufacturing at different temperatures, and how the strain mismatch helps or hinders the operation of the electrocaloric cooling cycle. The volumetric specific heats for the two materials are [57]

$$C_P = 2.5324 \times 10^6\ J/(m^3K)$$
$$C_P^{Cu} = 3.40252 \times 10^6\ J/(m^3K)\ . \quad \text{(A.9)}$$

The reference temperatures are all chosen to be the Curie temperature

$$\theta_1 = \theta_2 = \theta_1^{Cu} = \theta_2^{Cu} = 398\ K\ . \qquad (A.10)$$

Finally, both materials are thermally conductive (see Eq. 2.23(b)). The thermal conductivity for both materials is assumed to follow the general form $\boldsymbol{k} = k_0\boldsymbol{I}$ where $\boldsymbol{I}$ is the identity matrix. The isotropic thermal conductivities for the two materials are [57]

$$\begin{aligned} k_0 &= 2.61\ W/(mK) \\ k_0^{Cu} &= 401\ W/(mK)\ . \end{aligned} \qquad (A.11)$$

Obviously copper is much more thermally conductive than barium titanate. However, even though the two thermal conductivities have a difference of more than two orders of magnitude, the conductivity of copper cannot be taken as infinite in these calculations without significantly impacting the results.

A.3 NANODOT SIMULATION PARAMETERS

The nanodot simulations are fully three-dimensional. The thermal conductivity term is, again, ignored. This is appropriate since the simulations are essentially isothermal. The model parameters for the nanodot simulation are given in Eqs. A.2-A.5 and A.9(a)-A.11(a).

Appendix B: Normalization quantities

Several normalizations are used throughout this dissertation to provide easier to read plots and diagrams with more meaningful quantities. The spontaneous polarization and electric field are derived analytically from the free energy function and found to be

$$P_0 = 0.1811\ C/m^2$$
$$E_0 = 3.21 \times 10^5\ N/C\ . \qquad \text{(B.1)}$$

P_0 is the magnitude of the polarization in the stress-free, field-free bulk ferroelectric monodomain at the Curie temperature ($\theta_C = 398\ K$). E_0 is the electric field necessary to switch the polarization from one phase to another, also measure at θ_C. The spontaneous strain used for normalization is

$$\varepsilon_0 = Q_{11}P_0^2 = 3.28 \times 10^{-3} \qquad \text{(B.2)}$$

and gives the value of the strain in the tetragonal direction for the bulk stress-free, field free ferroelectric monodomain. Finally, σ_0 is given by

$$\sigma_0 = \frac{E_0 P_0}{\varepsilon_0} = 17.7\ MPa \qquad \text{(B.3)}$$

This is a derived quantity used for the normalization of the stress values and does not have a physical meaning.

References

[1] J. F. Scott, “Applications of Modern Ferroelectrics,” *Science*, vol. 315, no. 5814, pp. 954–959, Feb. 2007.

[2] W. Duan and Z.-R. Liu, “Theoretical modeling and simulations of perovskite ferroelectrics: From phenomenological approaches to ab initio,” *Curr. Opin. Solid State Mater. Sci.*, vol. 10, no. 1, pp. 40–51, Feb. 2006.

[3] P. R. Potnis, N.-T. Tsou, and J. E. Huber, “A Review of Domain Modelling and Domain Imaging Techniques in Ferroelectric Crystals,” *Materials*, vol. 4, no. 2, pp. 417–447, Feb. 2011.

[4] L.-Q. Chen, “Phase-Field Models for Microstructure Evolution,” *Annu. Rev. Mater. Res.*, vol. 32, no. 1, pp. 113–140, 2002.

[5] J. Fousek, “Joseph Valasek and the discovery of ferroelectricity,” in *Proceedings of 1994 IEEE International Symposium on Applications of Ferroelectrics*, 1994, pp. 1–5.

[6] W. Cao and L. E. Cross, “Theory of tetragonal twin structures in ferroelectric perovskites with a first-order phase transition,” *Phys. Rev. B*, vol. 44, no. 1, pp. 5–12, Jul. 1991.

[7] C. A. Randall, D. J. Barber, and R. W. Whatmore, “Ferroelectric domain configurations in a modified-PZT ceramic,” *J. Mater. Sci.*, vol. 22, no. 3, pp. 925–931, Mar. 1987.

[8] Y. Su and C. M. Landis, “Continuum thermodynamics of ferroelectric domain evolution: Theory, finite element implementation, and application to domain wall pinning,” *J. Mech. Phys. Solids*, vol. 55, no. 2, pp. 280–305, Feb. 2007.

[9] N. T. Tsou and J. E. Huber, “Compatible domain structures and the poling of single crystal ferroelectrics,” *Mech. Mater.*, vol. 42, no. 7, pp. 740–753, Jul. 2010.

[10] G. G. Wiseman and J. K. Kuebler, “Electrocaloric Effect in Ferroelectric Rochelle Salt,” *Phys. Rev.*, vol. 131, no. 5, pp. 2023–2027, Sep. 1963.

[11] G. G. Wiseman, “Electrocaloric effect in potassium dihydrogen phosphate,” *IEEE Trans. Electron Devices*, vol. 16, no. 6, pp. 588–593, Jun. 1969.

[12] A. S. Mischenko, Q. Zhang, J. F. Scott, R. W. Whatmore, and N. D. Mathur, “Giant Electrocaloric Effect in Thin-Film $PbZr_{0.95}Ti_{0.05}O_3$,” *Science*, vol. 311, no. 5765, pp. 1270–1271, Mar. 2006.

[13] G. Akcay, S. P. Alpay, J. V. Mantese, and G. A. Rossetti, “Magnitude of the intrinsic electrocaloric effect in ferroelectric perovskite thin films at high electric fields,” *Appl. Phys. Lett.*, vol. 90, no. 25, p. 252909, Jun. 2007.

[14] J. F. Scott, “Electrocaloric Materials,” *Annu. Rev. Mater. Res.*, vol. 41, no. 1, pp. 229–240, 2011.

[15] G. Akcay, S. P. Alpay, G. A. Rossetti Jr, and J. F. Scott, “Influence of mechanical boundary conditions on the electrocaloric properties of ferroelectric thin films,” *J. Appl. Phys.*, vol. 103, no. 2, p. 24104, Jan. 2008.

[16] B. Li, J. B. Wang, X. L. Zhong, F. Wang, and Y. C. Zhou, "Room temperature electrocaloric effect on $PbZr_{0.8}Ti_{0.2}O_3$ thin film," *J. Appl. Phys.*, vol. 107, no. 1, p. 14109, Jan. 2010.

[17] J. F. Scott, "Cylinder stress in nanostructures: effect on domains in nanowires, nanotubes, and nano-disks," *J. Phys. Condens. Matter*, vol. 26, no. 21, p. 212202, May 2014.

[18] M. Liu and J. Wang, "Giant electrocaloric effect in ferroelectric nanotubes near room temperature," *Sci. Rep.*, vol. 5, Jan. 2015.

[19] T. Correia and Q. Zhang, Eds., *Electrocaloric materials: new generation of coolers*. Heidelberg: Springer, 2014.

[20] R. I. Epstein and K. J. Malloy, "Electrocaloric devices based on thin-film heat switches," *J. Appl. Phys.*, vol. 106, no. 6, p. 64509, Sep. 2009.

[21] Y. S. Ju, "Solid-State Refrigeration Based on the Electrocaloric Effect for Electronics Cooling," *J. Electron. Packag.*, vol. 132, no. 4, pp. 041004–041004, Nov. 2010.

[22] J. H. Haeni, P. Irvin, W. Chang, R. Uecker, and et al, "Room-temperature ferroelectricity in strained $SrTiO_3$," *Nat. Lond.*, vol. 430, no. 7001, pp. 758–61, Aug. 2004.

[23] H.-L. Hu and L.-Q. Chen, "Three-Dimensional Computer Simulation of Ferroelectric Domain Formation," *J. Am. Ceram. Soc.*, vol. 81, no. 3, pp. 492–500, Mar. 1998.

[24] A. Kontsos and C. M. Landis, “Computational modeling of domain wall interactions with dislocations in ferroelectric crystals,” *Int. J. Solids Struct.*, vol. 46, no. 6, pp. 1491–1498, Mar. 2009.

[25] A. Kontsos and C. M. Landis, “Phase-Field Modeling of Domain Structure Energetics and Evolution in Ferroelectric Thin Films,” *J. Appl. Mech.*, vol. 77, no. 4, pp. 041014–041014, Apr. 2010.

[26] W. Li and C. M. Landis, “Nucleation and growth of domains near crack tips in single crystal ferroelectrics,” *Eng. Fract. Mech.*, vol. 78, no. 7, pp. 1505–1513, May 2011.

[27] I. Münch, M. Krauß, C. M. Landis, and J. E. Huber, “Domain engineered ferroelectric energy harvesters on a substrate,” *J. Appl. Phys.*, vol. 109, no. 10, p. 104106, May 2011.

[28] Y. L. Li, S. Y. Hu, Z. K. Liu, and L. Q. Chen, “Phase-field model of domain structures in ferroelectric thin films,” *Appl. Phys. Lett.*, vol. 78, no. 24, pp. 3878–3880, Jun. 2001.

[29] Y. L. Li and L. Q. Chen, “Temperature-strain phase diagram for $BaTiO_3$ thin films,” *Appl. Phys. Lett.*, vol. 88, no. 7, p. 72905, Feb. 2006.

[30] A. Y. Woldman and C. M. Landis, “Phase-field modeling of ferroelectric to paraelectric phase boundary structures in single-crystal barium titanate,” *Smart Mater. Struct.*, vol. 25, no. 3, p. 35033, 2016.

[31] M. E. Gurtin, “Generalized Ginzburg-Landau and Cahn-Hilliard equations based on a microforce balance,” *Phys. Nonlinear Phenom.*, vol. 92, no. 3–4, pp. 178–192, May 1996.

[32] J. Íñiguez, S. Ivantchev, J. M. Perez-Mato, and A. García, “Devonshire-Landau free energy of $BaTiO_3$ from first principles,” *Phys. Rev. B*, vol. 63, no. 14, p. 144103, Mar. 2001.

[33] Y. L. Wang *et al.*, “Landau thermodynamic potential for $BaTiO_3$,” *J. Appl. Phys.*, vol. 101, no. 10, p. 104115, May 2007.

[34] Y. L. Li, L. E. Cross, and L. Q. Chen, “A phenomenological thermodynamic potential for $BaTiO_3$ single crystals,” *J. Appl. Phys.*, vol. 98, no. 6, p. 64101, Sep. 2005.

[35] A. J. Bell and L. E. Cross, “A phenomenological gibbs function for $BaTiO_3$ giving correct e field dependence of all ferroelectric phase changes,” *Ferroelectrics*, vol. 59, no. 1, pp. 197–203, Jan. 1984.

[36] M. DiDomenico and S. H. Wemple, “Paraelectric-Ferroelectric Phase Boundaries in Semiconducting Perovskite-Type Crystals,” *Phys. Rev.*, vol. 155, no. 2, pp. 539–545, Mar. 1967.

[37] T. J. Parker and J. C. Burfoot, “The structure of transition fronts in barium titanate,” *Br. J. Appl. Phys.*, vol. 17, no. 2, p. 207, 1966.

[38] K. Bhattacharya and R. D. James, “A theory of thin films of martensitic materials with applications to microactuators,” *J. Mech. Phys. Solids*, vol. 47, no. 3, pp. 531–576, Mar. 1999.

[39] K. Dayal and K. Bhattacharya, “A real-space non-local phase-field model of ferroelectric domain patterns in complex geometries,” *Acta Mater.*, vol. 55, no. 6, pp. 1907–1917, Apr. 2007.

[40] D. Carka and C. M. Landis, “Equilibrium Conditions and Evolution of Needle Domain Arrays in Ferroelectric Single Crystals,” in *ASME 2012 Conference on Smart Materials, Adaptive Structures and Intelligent Systems*, 2012, pp. 255–257.

[41] V. Basso, C. P. Sasso, K. P. Skokov, O. Gutfleisch, and V. V. Khovaylo, “Hysteresis and magnetocaloric effect at the magnetostructural phase transition of Ni-Mn-Ga and Ni-Mn-Co-Sn Heusler alloys,” *Phys. Rev. B*, vol. 85, no. 1, p. 14430, Jan. 2012.

[42] C. M. Landis, “A continuum thermodynamics formulation for micro-magneto-mechanics with applications to ferromagnetic shape memory alloys,” *J. Mech. Phys. Solids*, vol. 56, no. 10, pp. 3059–3076, Oct. 2008.

[43] S. Kar-Narayan and N. D. Mathur, “Direct and indirect electrocaloric measurements using multilayer capacitors,” *J. Phys. Appl. Phys.*, vol. 43, no. 3, p. 32002, 2010.

[44] X. Moya *et al.*, "Giant Electrocaloric Strength in Single-Crystal $BaTiO_3$," *Adv. Mater.*, vol. 25, no. 9, pp. 1360–1365, Mar. 2013.

[45] Y. Xiao, V. B. Shenoy, and K. Bhattacharya, "Depletion Layers and Domain Walls in Semiconducting Ferroelectric Thin Films," *Phys. Rev. Lett.*, vol. 95, no. 24, p. 247603, Dec. 2005.

[46] D. M. Marincel *et al.*, "Influence of a Single Grain Boundary on Domain Wall Motion in Ferroelectrics," *Adv. Funct. Mater.*, vol. 24, no. 10, pp. 1409–1417, Mar. 2014.

[47] N. Balke *et al.*, "Enhanced electric conductivity at ferroelectric vortex cores in $BiFeO_3$," *Nat. Phys. Lond.*, vol. 8, no. 1, pp. 81–88, Jan. 2012.

[48] H. Fu and L. Bellaiche, "Ferroelectricity in Barium Titanate Quantum Dots and Wires," *Phys. Rev. Lett.*, vol. 91, no. 25, p. 257601, Dec. 2003.

[49] A. Schilling *et al.*, "Domains in Ferroelectric Nanodots," *Nano Lett.*, vol. 9, no. 9, pp. 3359–3364, Sep. 2009.

[50] S. Prosandeev and L. Bellaiche, "Characteristics and signatures of dipole vortices in ferroelectric nanodots: First-principles-based simulations and analytical expressions," *Phys. Rev. B*, vol. 75, no. 9, p. 94102, Mar. 2007.

[51] I. I. Naumov, L. Bellaiche, and H. Fu, "Unusual phase transitions in ferroelectric nanodisks and nanorods," *Nat. Lond.*, vol. 432, no. 7018, pp. 737–40, Dec. 2004.

[52] J. Wang, "Switching mechanism of polarization vortex in single-crystal ferroelectric nanodots," *Appl. Phys. Lett.*, vol. 97, no. 19, p. 192901, Nov. 2010.

[53] S. Prosandeev, I. Ponomareva, I. Kornev, I. Naumov, and L. Bellaiche, "Controlling Toroidal Moment by Means of an Inhomogeneous Static Field: An Ab Initio Study," *Phys. Rev. Lett.*, vol. 96, no. 23, p. 237601, Jun. 2006.

[54] K.-I. Park, S. Y. Lee, S. Kim, J. Chang, S.-J. L. Kang, and K. J. Lee, "Bendable and Transparent Barium Titanate Capacitors on Plastic Substrates for High Performance Flexible Ferroelectric Devices," *Electrochem. Solid-State Lett.*, vol. 13, no. 7, pp. G57–G59, Jul. 2010.

[55] K. M. Rabe, C. H. Ahn, and J.-M. Triscone, Eds., *Physics of ferroelectrics: a modern perspective*. Berlin ; New York: Springer, 2007.

[56] M. H. Sadd, *Elasticity: Theory, Applications, and Numerics*. Academic Press, 2009.

[57] Y. He, "Heat capacity, thermal conductivity, and thermal expansion of barium titanate-based ceramics," *Thermochim. Acta*, vol. 419, no. 1, pp. 135–141, Sep. 2004.